DT # 46895 QA:NA 2/3/06

Mechanical degradation of emplacement drifts at Yucca Mountain—A case study in rock mechanics.
Part I: Nonlithophysal rock

M. Lin[a*], D. Kicker[a], B. Damjanac[b], M. Board[b], M. Karakouzian[c]

[a]*Bechtel SAIC Company, 1180 Town Center Dr, Las Vegas, NV 89144, USA*
[b]*Itasca Consulting Group Inc., 111 Third Avenue South, Suite 450, Minneapolis, MN 55401, USA*
[c]*University of Nevada, Department of Civil and Environmental Engineering, 4505 Maryland Parkway, Box 454015, Las Vegas, NV 89154, USA*

Abstract–This paper outlines rock mechanics investigations associated with mechanical degradation of planned emplacement drifts at Yucca Mountain, which is the designated site for a U.S. high-level nuclear waste repository. The factors leading to drift degradation include stresses from the overburden, stresses induced by the heat released from the emplaced waste, stresses due to seismically related ground motions, and time-dependent strength degradation. The welded tuff emplacement horizon consists of two groups of rock with distinct engineering properties: nonlithophysal units and lithophysal units, based on the relative proportion of lithophysal cavities. Part I of the paper concentrates on the generally hard, strong, and fractured nonlithophysal rock. The degradation behavior of the tunnels in the nonlithophysal rock is controlled by the occurrence of keyblocks. A statistically equivalent fracture model was generated based on extensive underground fracture mapping data from the Exploratory Studies Facility at Yucca Mountain. Three-dimensional distinct block analyses, generated with the fracture patterns randomly selected from the fracture model, were developed with the consideration of *in situ*, thermal, and seismic loads. In this study, field data, laboratory data, and numerical analyses are well integrated to provide a solution for the unique problem of modeling drift degradation throughout the regulatory period for repository performance.

1. Introduction

Yucca Mountain is located on federal land on and adjacent to the Nevada Test Site in Nye County, Nevada. It has undergone comprehensive site characterization activities for gathering site information beginning in May 1986. In 2002, the site was designated as the U.S. repository for high-level nuclear waste.

Degradation of underground openings as a function of time is a natural and expected occurrence for any subsurface excavation. Over time, changes occur to both the stress condition and the strength of the rock mass due to several interacting factors. Once the factors contributing to degradation are characterized, the effects of drift degradation can typically be mitigated through appropriate design and maintenance of the ground support system. However, for the emplacement drifts of the geologic repository at Yucca Mountain, it is necessary to characterize drift degradation over a 10,000-year period or more, which is well beyond the functional period of the ground support system. This

---

[*] Corresponding author. Tel.: 1-702-295-4830; fax:+1-702-295-5198 E-mail address: ming_lin@ymp.gov

paper provides a summary of the study of the stability of repository excavations and potential mechanical degradation under the action of *in situ*, thermal, and seismic stresses during the first 10,000 years of repository performance.

2. Site Geology and Geotechnical Characteristics of the Host Rock

The proposed repository will be located in tuff that was deposited by a series of volcanic eruptions between 11 and 14 million years ago. The lithostratigraphy and geologic evolution of the Yucca Mountain site is described in *Yucca Mountain Site Description* (Bechtel SAIC Company 2004a). The water table at Yucca Mountain is approximately 500 m to 800 m below the surface at the repository location. The deep water table and thick unsaturated zone result from the low infiltration rate of surface water due to low annual rainfall and high rates of evaporation and transpiration.

Site-specific characteristics of the rock units of the Topopah Spring Tuff that constitute the host rock at the repository horizon are found in the geologic mapping of those units in both the main drift and ramps of the Exploratory Study Facility (ESF) and the Enhanced Characterization of the Repository Block (ECRB) Cross-Drift (Figure 1). The units that comprise the host rocks of the repository horizon are zones of the crystal-poor member of the Topopah Spring Tuff. The host rocks are shown schematically in Figure 2. In descending order (by depth), the repository horizon consists of the lower part of the upper lithophysal zone (Tptpul), the middle nonlithophysal zone (Tptpmn), the lower lithophysal zone (Tptpll), and the lower nonlithophysal zone (Tptpln). The repository host rock units can be categorized into two general engineering classifications: nonlithophysal units (Tptpmn and Tptpln) and lithophysal units (Tptpul and Tptpll), based on the relative proportion of lithophysal cavities. According to current design, the entire repository is to be located in densely welded and crystallized volcanic tuff with approximately 85% of the repository in lithophysal tuff and 15% in nonlithophysal tuff. The nonlithophysal units are generally hard, strong, fractured rocks with matrix porosities of 10% or less. Fractures that formed during the cooling process are the primary structural features found in these units. In contrast, the lithophysal units have significantly fewer fractures of significant continuous length (i.e., trace length greater than 1 m), but have relatively uniformly distributed porosity in the form of lithophysal cavities. Lithophysal porosity in the Tptpul and Tptpll is generally on the order of less than 10% to about 30% by volume. The groundmass that makes up the rock matrix in the lithophysal units is mineralogically the same as the matrix of the nonlithophysal units, but is heavily fractured with small scale (lengths of less than 1 m) fractures in the Tptpll; however, it is relatively fracture-free in the Tptpul.

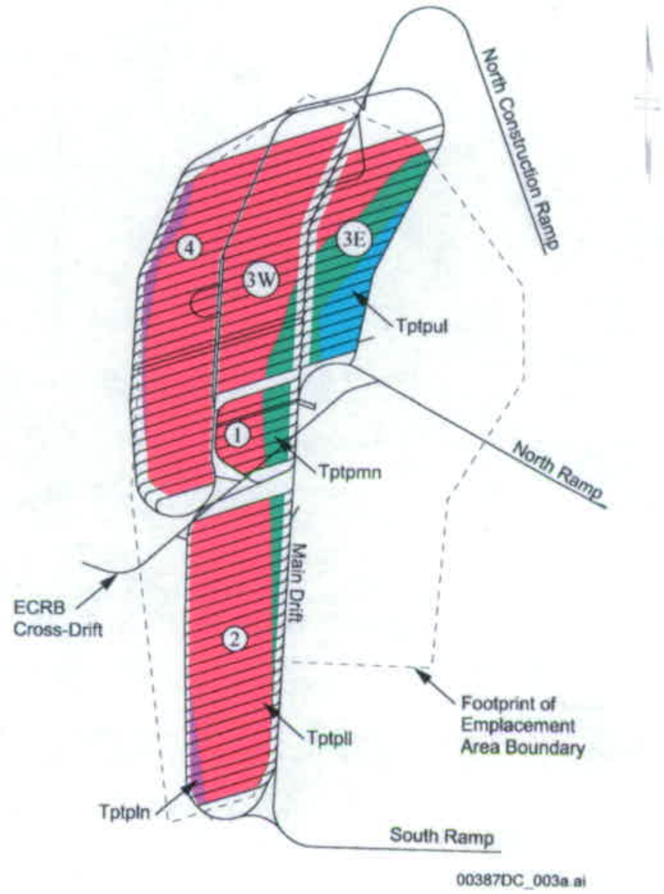

Note: The repository includes 5 panels: Panels 1, 2, 3E, 3W, 4, and 5

Figure 1. Proposed Repository Layout in Plan View Showing Intersections of Geologic Subunits with Emplacement Drifts

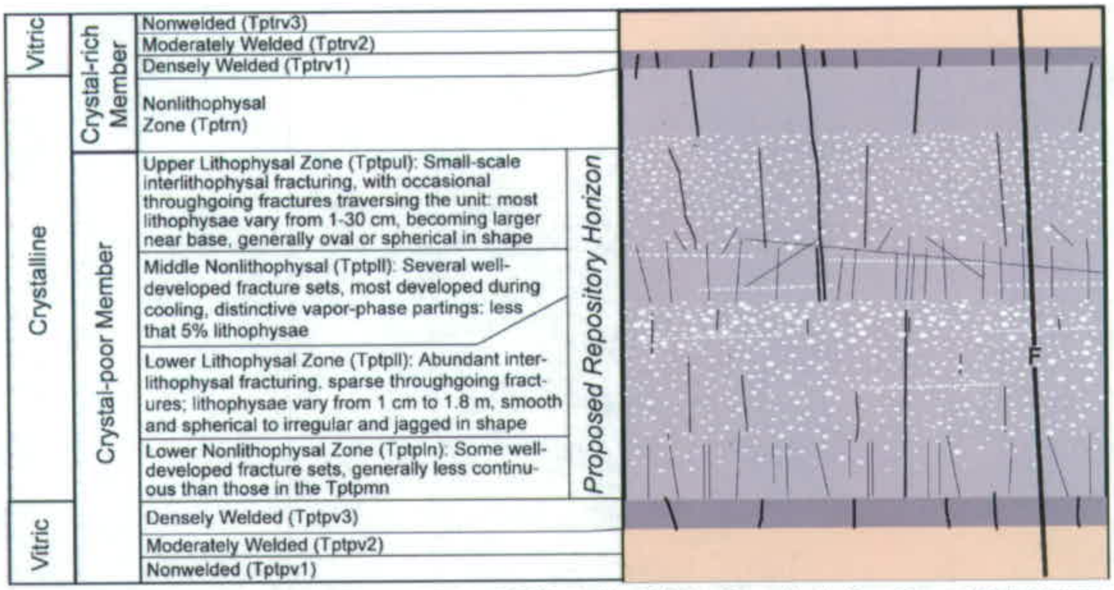

Diagrammatic Cross-Section of the Topopah Spring Tuff Illustrating Relative Discontinuity Densities and Orientations: This figure indicates how fractures, faults, and lithophysae are typically distributed through the ignimbrite.

Figure 2. Structure of the Topopah Spring Tuff Showing Relative Relationship between Fracturing and Lithophysae in Major Flow Subunits

The rock matrix material is a typical fine-grained volcanic rock of silica content with a mean unconfined compressive strength of approximately 180 MPa (Bechtel SAIC Company 2003). The structure of the rock mass defines the properties and overall mechanical response of the rock mass to thermal and mechanical loading. The fracture geometry and properties in the nonlithophysal rocks and the degree of porosity (total and lithophysal) in the lithophysal subunits are the primary geologic structural features that impact rock mass behavior. More detailed description on the effect of lithophysal cavities on the rock mechanical behavior is provided in Part II .

Geotechnical mapping of fractures has been performed in the ESF and the ECRB Cross-Drift (CRWMS M&O 1998; Mongano et al. 1999). Figure 3 presents a schematic of the Topopah Spring Tuff Formation, illustrating the general occurrence of fracturing and lithophysae in the various subunits of the repository host horizon. The occurrence of fractures and lithophysae are roughly inversely proportional as demonstrated quantitatively in Figure 3, where the fracture density (fractures with trace length greater than 1 m) determined from detailed line mapping and the approximate percentage of lithophysal porosity in the ECRB Cross-Drift are shown. The density of fractures with trace length greater than 1 m is significantly larger in the nonlithophysal rock (20 to 35 fractures/10 m), compared to the lithophysal rock (5 fractures/10 m). Conversely, lithophysae are sparse in the nonlithophysal units.

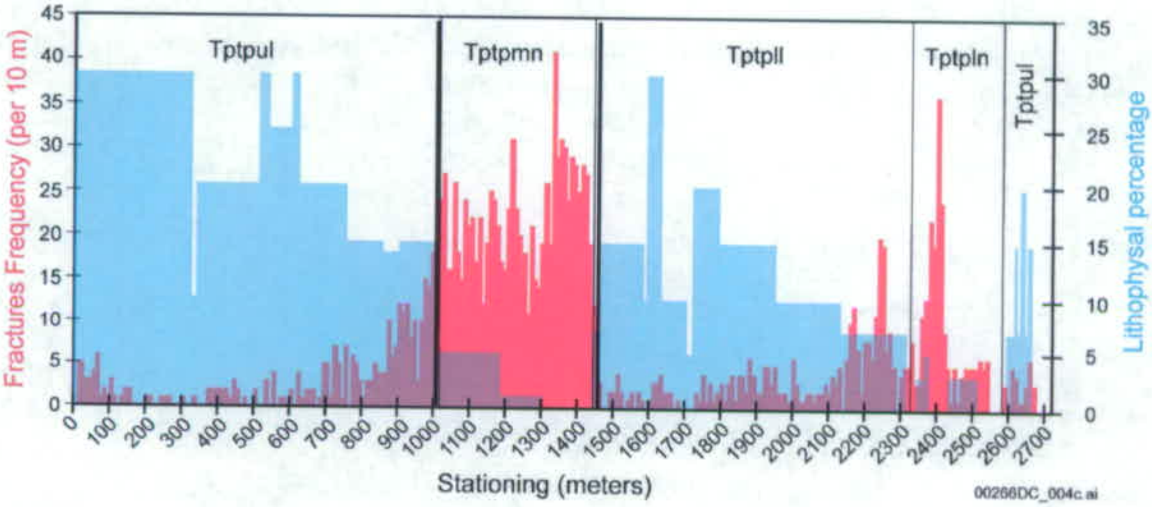

Figure 3. Composite Plot of Fracture Frequency and Lithophysal Porosity as a Function of Distance along the Enhanced Characterization of the Repository Block Cross-Drift

The field fracture database, constructed from mapping in the ESF and ECRB Cross-Drift during tunneling operations, consists of full-periphery maps and detailed line surveys of all fractures with length of one meter or greater. In total, a database of more than 35,000 fracture descriptions is available. In summary, there are four sets of fractures in the Tptpmn with the geometrical and surface characteristics shown in Table 1.

Table 1. General Characteristics of Fracture Sets in the Nonlithophysal Unit

Set	Observed Orientation, Azimuth/Dip (°)	Median Spacing (m)	Median Trace Length (m)	Comment
1	120/84	0.48	3.3	Rough to smooth, planar
2	215/88	1.08	2.9	Smooth but curved
3	302/38	3.40	3.7	Random fractures with generally flat to moderate dip
4	329/14	2.46	3.5	Vapor-phase partings, rough, cohesive with coating minerals, planar

The low-angle vapor-phase partings are relatively continuous structures seen throughout the nonlithophysal rock. These continuous, but anastomosing fractures are subparallel to the dip of the rock unit, and are filled with concentrations of vapor-phase mineralization (primarily tridymite and cristobalite). The surfaces are rough on a small scale and, unlike the subvertical fractures, have cohesion as a result of the mineral filling.

Rotary and direct shear tests were conducted on natural rock fractures from core samples in the repository host units. An average cohesion of 0.9 MPa and peak friction angle of 41° was obtained from the rotary shear tests. The results from the direct shear tests are divided into two groups: one represents the subvertical cooling joints and the other for the vapor-phase parting. The average cohesion and peak friction angle are 0.3 MPa and 34° for the cooling joints and 0.7 MPa and 44° for the vapor-phase parting.

3. General Approach

The nature of the fracture geometry governs the estimates of the stability and degradation of the nonlithophysal rock mass, particularly under the action of seismic shaking, as well as estimates of the support performance and level of required ground support. The blocks of nonlithophysal rock are significantly stronger than the *in situ* and thermally induced stresses, and thus the problem of modeling this material is essentially one of elastic blocks separated by fracture surfaces. Therefore, in modeling of the stability of the tunnels and the rockfall that may occur from the applied load, the fracture geometry and surface properties are of primary importance. Three-dimensional discontinuum numerical methods are required for correct representation of the degradation mechanism. The approach to modeling mechanical degradation and rockfall from combined *in situ*, thermal, and seismic loading in nonlithophysal rock is illustrated in Figure 4. This approach involves modeling of emplacement drifts excavated within the stochastically defined, representative fractured rock mass volume, followed by application of *in situ*, thermal, and seismic load. A large number of parameter studies are conducted in which the tunnel location (and fracture geometry), rock fracture surface properties, and loading conditions are varied to derive a appropriate range of performance response (in terms of rockfall mass, volume, and opening shape) that is indicative of the possible geologic conditions at depth. Sensitivity study of the thermal properties and preclosure heat removal ratio (considering both 90% and 70% heat removal cases) is also included.

The time to failure for intact nonlithophysal rock blocks due to stress corrosion shows significantly less time dependency than for the lithophysal rock based on the laboratory long-term testing data (Bechtel SAIC Company 2004b). Therefore, insignificant time-related fracture growth is expected in the intact rock blocks in nonlithophysal units. Contrary to the lithophysal rock, time-dependent strength degradation within the intact block is not considered for the nonlithophysal rock.

Ground support is not considered in the mechanical degradation models in this study. The rock blocks predicted in this study are, therefore, blocks that fail in an unsupported opening. This modeling approach leads to a conservative prediction of unstable blocks for the time frame before the closure of the repository (i.e., more blocks will be predicted to fail in the model that would otherwise be supported and remain stable with ground support). During the postclosure period, ground support will degrade and eventually fail. Not including ground support in the rockfall models is realistic for the postclosure period.

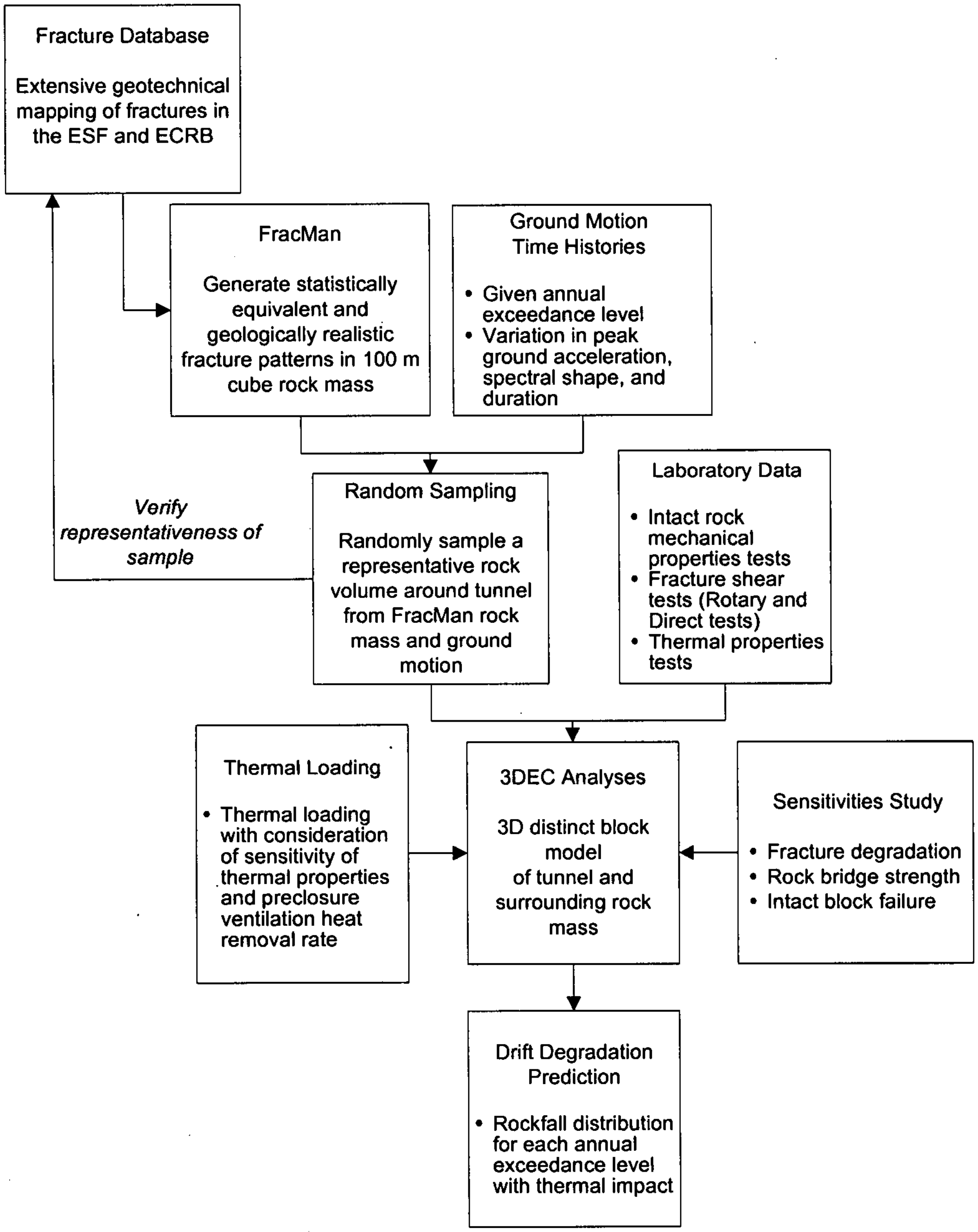

Figure 4. Approach of Drift Degradation and Rockfall Analyses for Nonlithophysal Rock

4. Development of Fracture Geometries for Nonlithophysal Rock

The development of a stochastically defined fracture system, representative of the actual rock mass, is accomplished using the FracMan program (Dershowitz 1984). The existing fracture mapping database provides the basic input to the FracMan program, which develops sets of planar, circular fracture planes that conform to the statistical variability of the geometric characteristics of the input data. Statistical models are fitted to the various geometric characteristics of each fracture set in the database, followed by generation of representative fracture sets. These representative fractures are then back-checked against the statistical variability and geologic realism of the field data to achieve an acceptable facsimile. Details of this process are described in *Drift Degradation Analysis* (Bechtel SAIC Company 2004b). A three-dimensional representative rock mass cube, 100 m on a side, is generated using FracMan and composed of the matrix blocks defined by approximately 90,000 fractures. Each fracture is described by its centroid coordinate, dip, dip direction, and radius. These geometric properties are used as direct inputs to the distinct element code 3DEC (Itasca Consulting Group 2002) for development of a block geometry within which emplacement drifts can be randomly excavated.

The constructed FracMan fracture region is calibrated to the observed data for orientation and its dispersion, size and its distribution, and intensity (as measured by interfracture distance) and its distribution on a set-by-set basis. In addition, any biases due to sampling were effectively removed by using the same sampling style as the observed data collection when comparing the synthetic and the observed data sets. The detailed line survey data in the Tptpmn unit are used to condition FracMan to develop representative fracture trace lengths and spacings. Table 2 displays the mean orientation of the sets, a comparison of median fracture radius converted to diameter and median trace length, and intensity (median spacing) from FracMan and median spacing from the detailed line surveys. A direct comparison between actual full periphery geologic maps from the ESF to synthetic full periphery geologic maps from FracMan is given in Figure 5. This comparison ensures that the synthetic fracture geometries are not only quantitatively validated, but similar from a geological perspective as well.

Table 2. Comparison of Data from Field Mapping and FracMan Output for the Tptpmn

Set	**Observed Orientation (Strike/Dip)**	**FracMan Orientation (Strike/Dip)**	**Median Inter-Fracture Distance (m)**		**Median Trace Length from Full Periphery Geologic Maps (m)**	**Trace Length Median from FracMan (m)**
			Observed	**FracMan**		
1	120/84	125/84	0.48	0.79	3.3	2.8
2	215/88	214/86	1.08	1.29	3.1	2.9
3	302/38	299/43	3.40	3.16	3.6	3.7
4	329/14	327/08	2.46	1.48	3.4	3.5

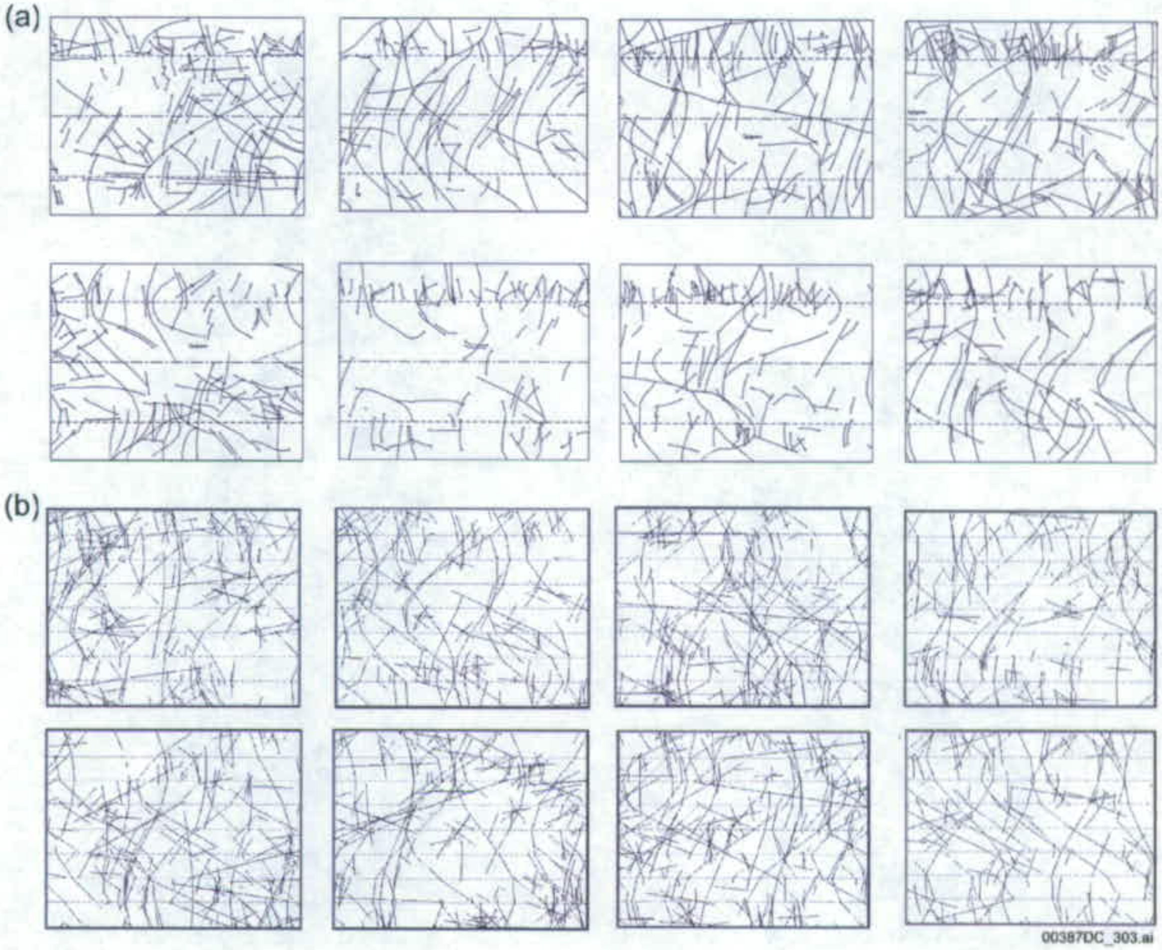

Figure 5. Comparison of (a) Full Periphery Geologic Maps from the Tptpmn in the Exploratory Studies Facility with (b) Simulated Full Periphery Geologic Maps from the FracMan Cube

5. Distinct Block Dynamic and Thermal-mechanical Analyses

A total of 50 emplacement drifts are randomly located and "excavated" within the 100 m cube rock mass generated by FracMan, such that the stochastic nature of the jointed medium and its impact on rockfall is adequately sampled. A random emplacement drift centroid coordinate is chosen within the cube, and a 25 m × 25 m × 25 m volume, oriented at the emplacement drift 72° azimuth, is extracted to contain the model emplacement drift (Figure 6). The dimension of the model is selected to optimize the time required for analysis and the ability of the model to accurately predict rockfall. Sensitivity of the model dimension to the outcome of rockfall prediction has been evaluated and concluded to be adequate. Within each emplacement drift, a rigid, rectangular block representing the drip shield[1] is affixed to the invert of the tunnel.

---

[1] A titanium drip shield is planned to be installed over the waste packages prior to repository closure. The purpose of the drip shield is to divert any moisture that might drip around the waste packages to the drift floor. The drip shields are designed to maintain their function in the event of rockfall.

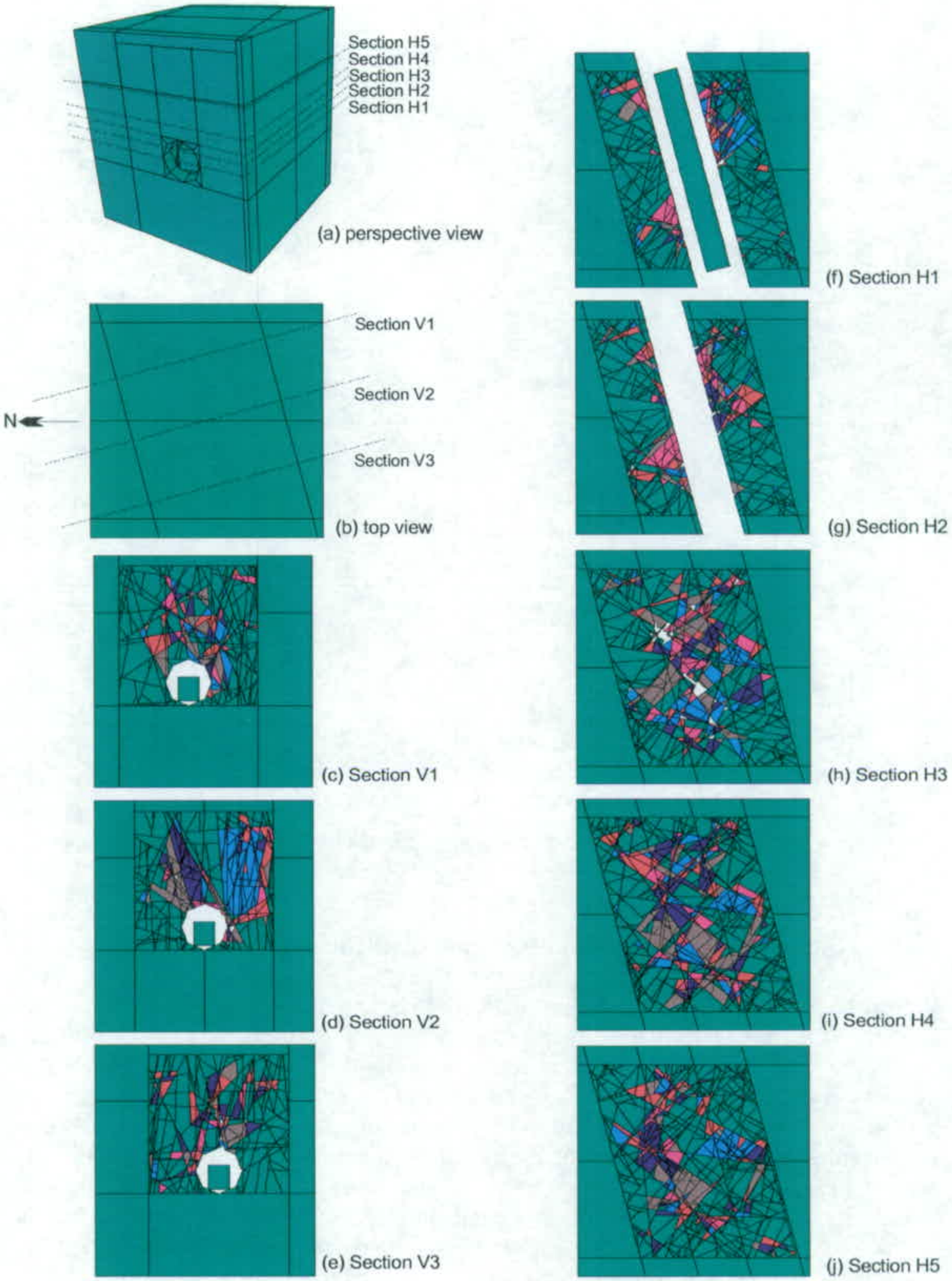

(a) perspective view
(b) top view
(c) Section V1
(d) Section V2
(e) Section V3
(f) Section H1
(g) Section H2
(h) Section H3
(i) Section H4
(j) Section H5

Figure 6. 3DEC Model Geometry and Cross Sections

Because the fractures within the Tptpmn are nonpersistent in nature (with median trace lengths of approximately 3 m [Table 2], which is smaller than the 5.5-m tunnel diameter), many fractures are of insufficient length to form a regular block. An algorithm was developed for applying the FracMan fracture geometry to the 3DEC model. Previous versions of the 3DEC program were set up to only efficiently handle through-going joint planes. The new algorithm allows incomplete fractures to be cut within a block, or to terminate against other fractures, thus creating realistic fracture patterns within the rock mass. In other words, portions of a fracture plane could be assigned a standard Coulomb slip behavior, whereas others could be bonded to the opposing surface with the strength of the adjacent rock blocks, thereby creating fractures that have rock "bridges" along their surface. In this case, the rock bridge acts as a strong bond along the fracture surface, but can still fail in shear or tension if the stresses so dictate. In this manner, it is possible to represent a discontinuous fracture system, but one in which breakage of solid rock can occur. The resulting blocks within the 3DEC model are fully deformable as they are subdivided into tetrahedral finite difference zones with a linear elastic constitutive model. The 3DEC model uses a fully dynamic solution algorithm to solve the laws of motions for the blocks, subject to contact restraints with surrounding blocks. The gridpoints along the fracture surfaces act as contact points across which forces are transmitted, subject to shear and tensile yield conditions.

Other enhancements added to 3DEC for rockfall modeling include: (a) implementation of the "free field" boundary to provide a "quiet" or "non-reflecting" boundary for dynamic analysis with superposition of the P and S wave motions, and (b) partial density scaling for dynamic analysis. These enhancements enable an efficient solution for the dynamic simulation of the seismic wave propagation in three-dimensional media.

5.1. Dynamic Analysis with Seismic Loads

Input properties for the distinct block 3DEC model involve both the fracture and block (intact) properties. Table 3 lists the base case properties used in 3DEC. A linear elastic model is used for the block material, whereas Coulomb slip criterion is used to represent joint mechanical behavior. This approach is used to obtain a conservative (i.e., increased) estimate of the block volume. Breaking and spalling of the rock inside the blocks are expected considering the large amplitude of seismic waves for postclosure ground motions. Although the shallow-dipping vapor-phase parting consists of higher cohesive material, a single set of joint mechanical properties are used for the joint sets for conservatism (i.e., more rockfall will be produced). Coulomb slip criterion is also used for the intact bridges between adjacent fractures, where the intact cohesion and friction is assigned for the bridge strength.

The initial state of stress was included at the model consolidation stage. The vertical component of *in situ* stress (the major principal stress) is approximated as 7 MPa considering an overburden depth of 300 m. The horizontal components of *in situ* stress (the minor and intermediate principal stresses) are simplified to be 3.5 MPa based on an average horizontal-to-vertical stress ratio of 0.5. The *in situ* stress for each emplacement drift will vary depending on the cover depth on top of the drift. The approximated values assigned for the *in situ* stress are adequate and the results are insensitive judging the magnitude of the induced seismic and thermal stress.

Table 3. Base-Case Material Properties for 3DEC Analysis

Joint strength properties	Joint cohesion (MPa)	0.1
	Joint friction (°)	41
	Joint dilation (°)	0
	Joint normal stiffness, K_n (MPa/m)	5×10^4
	Joint shear stiffness, K_s (MPa/m)	5×10^4
Intact rock deformation properties	Young's modulus (GPa)	33.0
	Poisson's ratio	0.21
	Bulk modulus (GPa)	19.2
	Shear modulus (GPa)	13.6
Intact bridge strength properties	Cohesion (MPa)	47.2
	Friction angle (°)	42
	Tensile strength (MPa)	11.6

NOTE: Joint dilation is set to zero for the base-case analysis. With no dilation, joints are modeled as perfectly planar and smooth, resulting in a conservative (i.e., higher) estimation of rockfall.

Site-specific ground motions were developed for Yucca Mountain through use of a formal process of expert elicitation resulting in development of a Probabilistic Seismic Hazard Assessment (PSHA)[2]. Site-specific ground motion time histories for four levels of annual probability of exceedance, 1×10^{-4}, 1×10^{-5}, 1×10^{-6}, and 1×10^{-7}, were examined.

A total of 15 sets of ground motion time histories were developed at the repository horizon for each annual postclosure hazard level. The multiple sets ensure a reasonable distribution of spectral shapes and time history duration. For each set of ground motions, two horizontal components (H1 and H2) and one vertical component (V) of acceleration, velocity, and displacement are supplied. The motions include the effects of the free surface reflections, and, thus, the 3DEC model does not need to account for them. Figure 7 shows the H1 velocity time history for four annual hazard levels. In running the 3DEC simulation, the duration of the seismic time histories was truncated to a duration bracketed the 5% and 95% points in the energy buildup as measured by Arias Intensity (an estimate of energy delivered to the structures), as shown in Figure 7. The amplitude

---

[2] The ground motion hazard determined in the PSHA expert elicitation is unbounded. Because the ground motion experts characterized aleatory variability in ground motion using unbounded lognormal distributions, as the PSHA calculations are extended to lower and lower annual probabilities of exceedence, the mean ground motions increase without bound, eventually reaching levels that are not credible. An analysis was conducted to determine a bound to peak ground velocity (PGV) at the repository level based on the shear strain increments (relative to the in situ stress state) required to fracture the Tptpll rock (Bechtel SAIC Company 2005). The bound to PGV at the repository level has been shown, based on physical strain limitations of the lithophysal rock mass, to be approximately 4 m/s. The unbound velocity time histories were used in this study for conservatism.

of the peak ground acceleration, velocity, and displacement, and the seismic-induced far-field stress for one of the ground motion sets from each hazard level are provided in Table 4.

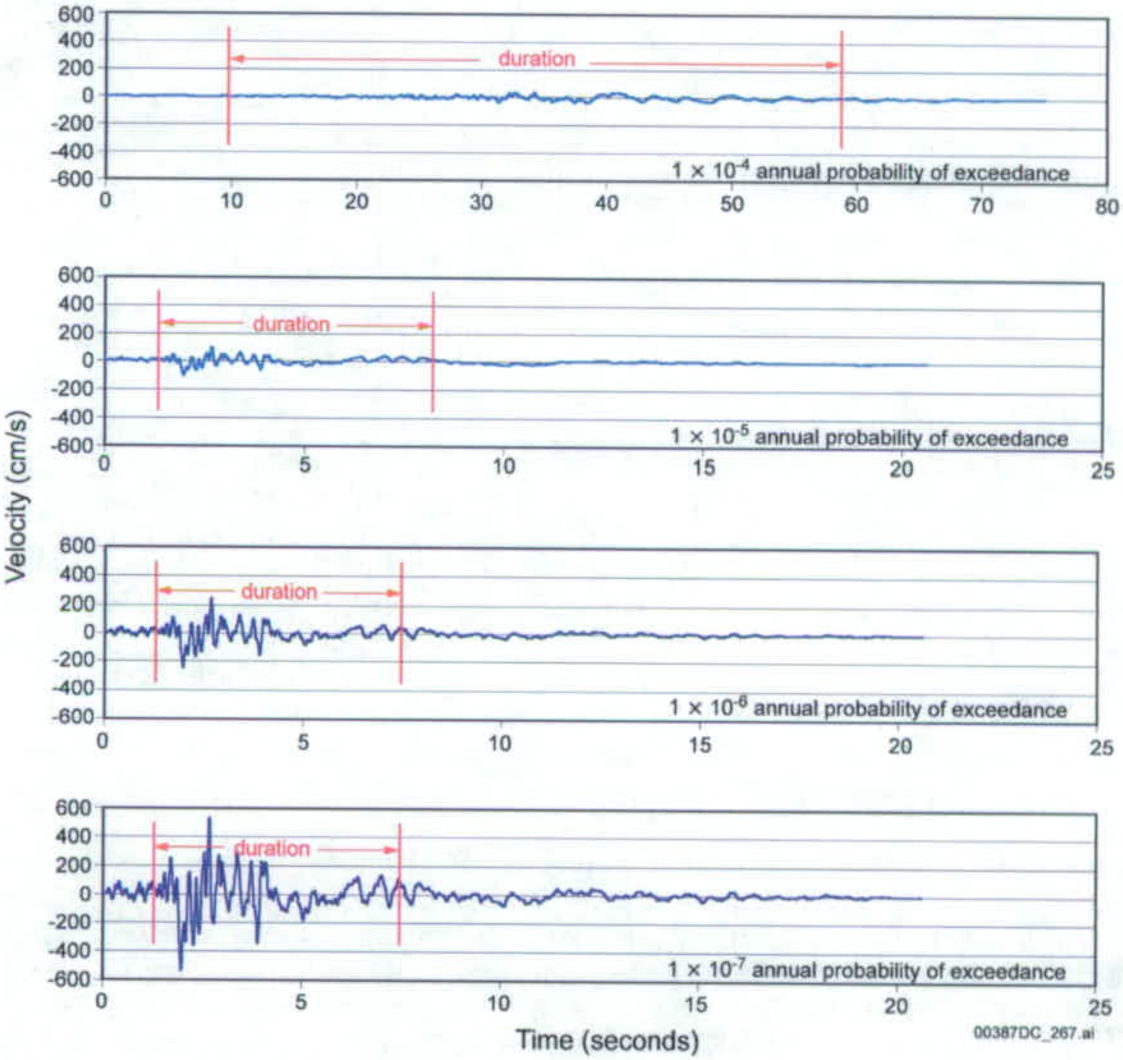

Figure 7. Examples of Ground Velocity Time Histories (H1) with Truncated Duration for Analysis

Table 4. Peak Ground Motion Parameters

Annual Hazard Level	Ground Motion Component	Peak Acceleration (g)	Peak Velocity (cm/s)	Peak Displacement (cm)	Seismic Induced Stress Corresponding to Peak Velocity (MPa)
1 × 10^{-4}	H1	0.39	38.38	44.44	2.20
	H2	0.37	43.78	45.3	2.51
	V	0.47	47.51	31.73	4.50
1 × 10^{-5} (Set 1)	H1	2.77	104.58	20.06	6.00
	H2	2.50	83.31	14.37	4.78
	V	2.63	70.88	13.00	6.71
1 × 10^{-6} (Set 1)	H1	7.42	244.14	26.76	14.00
	H2	6.74	195.41	26.78	11.21
	V	4.90	111.29	13.75	10.54
1 × 10^{-7} (Set 1)	H1	16.28	535.26	58.68	30.00
	H2	14.79	428.42	58.72	24.57
	V	13.15	298.44	36.86	28.25

Nonreflecting vertical and upper model boundaries in 3DEC allow the wave to pass through the model, and free-field boundaries on the vertical sidewalls of the model prevent damping and distortion along the vertical sidewalls of the incoming wave. No material damping[3], in addition to that supplied by sliding on fracture surfaces, is supplied to the model. Prior to use of the model for examination of drift degradation, seismic wave propagation of models without tunnels was run to ascertain that the wave passed through the model without significant distortion.

A goal of these analyses is to provide an estimate of seismically induced rockfall that is derived from an adequate sampling of the variability of fracture geometries and ground motion time histories. A simple Latin Hypercube sampling scheme was used for the pairing of ground motion and fracture modeling region (Bechtel SAIC Company 2004c). A total of 50 sets of paired fracturing realizations (i.e., drift centroid locations) and ground motion data were made for each postclosure annual exceedance frequency. For each of these analyses, a base case of block and fracture material properties were used so that the variability of the rockfall response was then a function of the fracture geometry and ground motion variability only. The base case rock and fracture properties are given in Table 3. The adequacy of 50 analyses for representation of the variability of rockfall (at each exceedance level) was verified by calculation of the cumulative mean and standard deviation of rockfall parameters for successive analyses. The mean and standard deviation of rockfall mass does not change after approximately 30 runs.

The results of the seismic analyses are presented in terms of rockfall impact and drift profile. The former provides inputs for the drip shield and waste package design and the later is for seepage consideration. Figure 8 shows typical blocks impacting the drip shield in the 3DEC dynamic simulation. The block representing the drip shield is

---

[3] 0.3% of critical damping was used in a few analyses for numerical stability purposes.

anchored at the invert, and is included in the model to record the information on the locations and relative velocities for rockfall impact. Summary histograms for the rockfall impact information with 1×10^{-6} annual probability of exceedance earthquakes are presented in Figure 9. Also included in each histogram plot is the cumulative frequency of occurrence. The block mass, impact momentum and impact energy show the trend of negative exponential distribution with most of the data concentrated on the low end of the data range. The impact velocity shows a typical bell shape for the normal distribution. The distribution centers around 3 m/s with a standard deviation of approximately 1.7 m/s. The relatively low impact velocities indicate that block fallout is mainly due to gravitational freefall. Differential acceleration or energy trapping to induce high ejection velocity is not observed.

Rockfall analyses were also completed for ground motions with 1×10^{-4}, 1×10^{-5}, and 1×10^{-7} annual exceedance probabilities. The 1×10^{-4} ground motion includes one ground motion set with 32 simulations. A total of 44 cases was conducted for 1×10^{-7} motions, as convergence of the median rock block size was evident after this number of analyses. Figure 10 shows a comparison of histograms of block mass for all four ground-motion results. Essentially, the results show that all motions result in the same general distribution of block sizes with mean block masses of less than 0.2 metric tons, and a negative exponential distribution.

Figure 11 presents correlation of rockfall volume per 3DEC simulation with peak ground velocity (PGV in H1 direction). At any given level of PGV, the variability in rockfall based on the variability in fracture pattern and ground motion frequency characteristics results in a fairly wide distribution in response. Although no strong relationship is observed between rockfall volume and PGV, a roughly linear relationship exists between the upper bound to rockfall volume and PGV on this semi-log plot. The fracture pattern is the predominant mechanism for variability in rockfall at a given level of PGV.

Figure 8. Simulation of Rockfall Impact to the Drip Shield

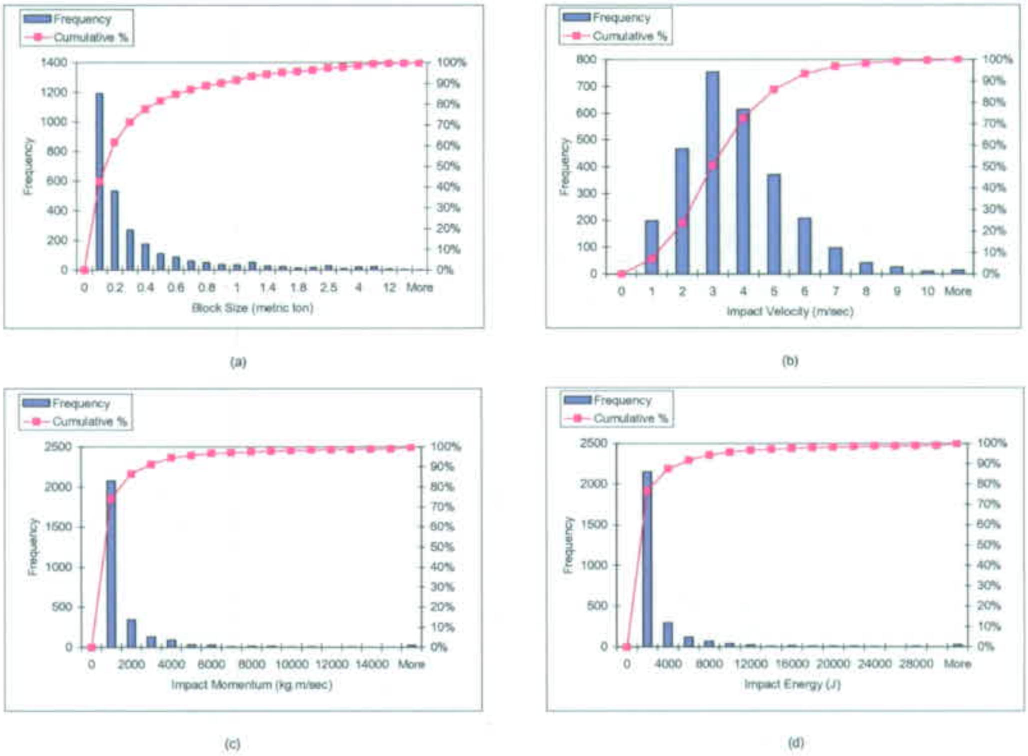

Figure 9. Summary Histograms for Seismic Analyses with 1×10^{-6} Annual Probability of Exceedance Hazard: (a) Block Size (b) Relative Impact Velocity (c) Impact Momentum, and (d) Impact Energy

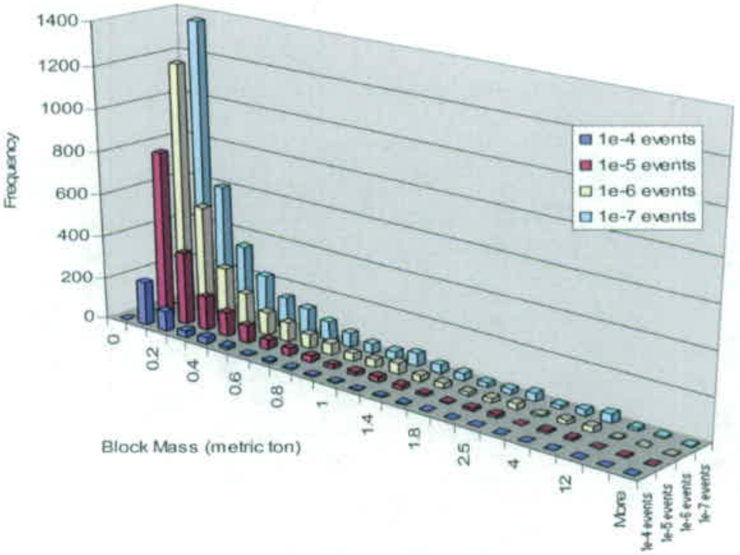

Figure 10. Comparison of Histograms of Block Mass from Preclosure and Postclosure Ground Motions

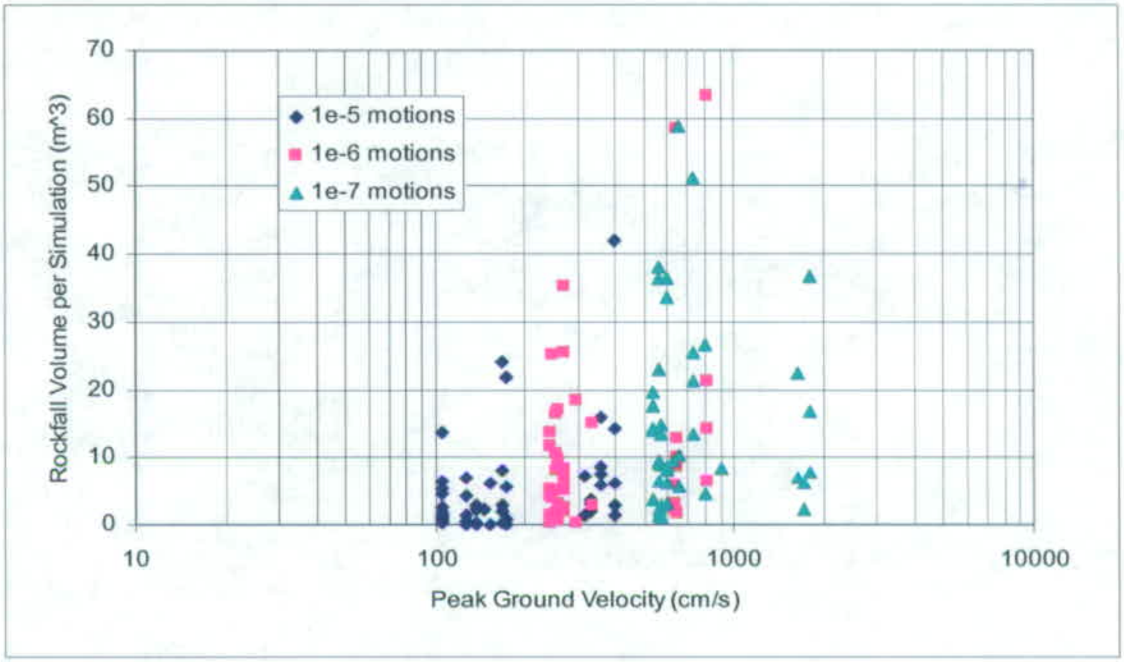

Figure 11. Rockfall Volume versus Peak Ground Velocity

Table 5 compares rockfall statistics for the different annual probabilities of ground motion exceedance. Due to the variable number of runs, the important comparison statistic is the number of blocks per kilometer, which shows an increase from 535 blocks for 1×10^{-4} ground motion to 3,079 blocks for 1×10^{-7} ground motion.

Table 5. Comparison of Rockfall Statistics

Statistic	**Ground Motion Annual Probability of Exceedance**			
	1×10^{-4}	1×10^{-5}	1×10^{-6}	1×10^{-7}
Runs Completed	32	50	50	44
Total Number of Rockfall	428	1,764	2,797	3,387
Total Volume of Rockfall (m^3)	39.4	255.4	497.7	705.2
Total Length of Drift Simulated (m)	800	1,250	1,250	1,100
Number of Blocks per km	535	1,414	2,238	3,079
Volume of Rockfall per km (m^3/km)	49.3	204.3	398.2	641.1

The three-dimensional depiction of an emplacement drift after seismic shaking provides a physical perspective for the impact of seismically induced rockfall on the drift profile. Figure 12 shows the rockfall profile for the case showing the greatest amount of rockfall for a 1×10^{-6} annual probability of exceedance ground motion. Two particular cases of the 50 analyzed show a larger amount of rockfall due to the fact that the two long, subvertical fracture sets strike at a low angle to the axis of the emplacement drift. This, coupled with the presence of closely spaced subhorizontal vapor phase partings or random sets, allows a number of roof and sidewall blocks to detach over a significant plan view area. The drift preferentially breaks out along the sidewalls since this is the location of highest induced stress along the tunnel periphery.

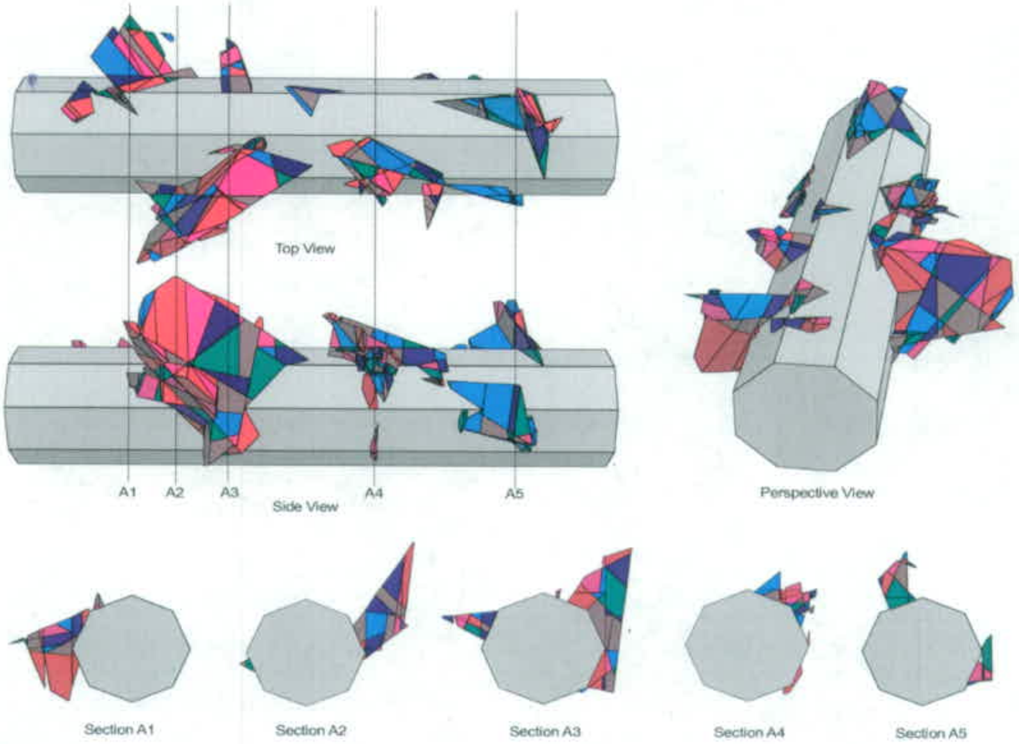

Figure 12. Drift Profile for 1 × 10^{-6} Hazard Level, Case with Greatest Amount of Rockfall

5.2. Thermal-mechanical Analysis

Thermal-mechanical modeling was performed to define drift stability under combined *in situ* and thermally induced stresses. Temperatures within the rock mass are determined from thermal analysis conducted using the NUFT program, which accounts for the details of heat transfer mechanisms within the drift, including heat removal due to ventilation in the preclosure period. The NUFT thermal calculation considers a 1.45 kW/m initial linear heat load and 50-year preclosure ventilation with 90% of heat removed by ventilation. The NUFT approach is two-dimensional and, thus, assumes a cross section through a series of infinitely long emplacement drifts. Thus, this type of approach adequately represents the developing temperature distribution around emplacement drifts located centrally within the repository. Figure 13 presents the drift crown temperature history. The peak temperature was predicted to be 138°C at approximately 75 years, and reduced to below boiling after 1,000 years.

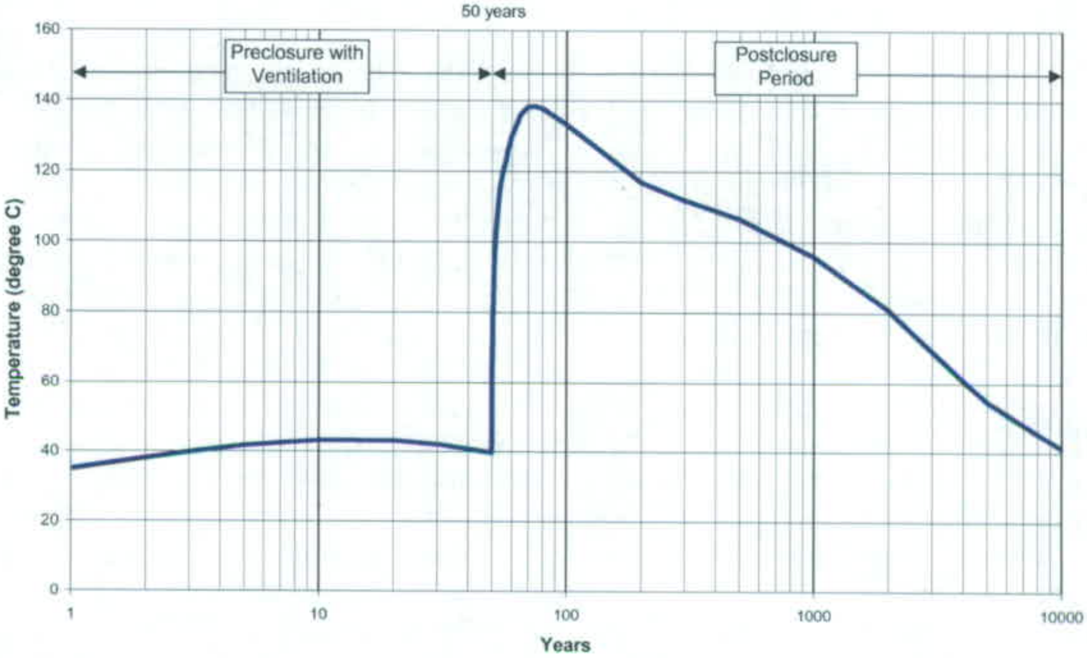

Figure 13. Predicted Drift Crown Temperature History

Rockfalls induced by thermal loading are found to be minor. Most of the damage, although little, occurs in the rock mass during the heating period. Less than 1 m^3 of rockfall is predicted within the 25-m tunnel simulated for all cases analyzed. There is little to no change on yielding and permanent deformation during the cool-down period. Sensitivity of rock thermal properties results show an insignificant effect with varying rock thermal properties by one standard deviation.

For the combination of *in-situ*, thermal and seismic loads, three example cases were chosen to cover the likely range of drift degradation. The thermal state with the highest level of rock temperature and thermally induced rock stress (i.e., 80 years after waste loading) was chosen. The initial state (before heating began) and the state after 80 years of heating coincide with extreme points on thermally induced stress paths at a number of locations around the emplacement drift. The state after 80 years was felt to be of greatest interest because already-completed analyses with no thermal loading provide the other extreme thermal condition. In summary, the impact of thermal loading in nonlithophysal rock is to stabilize the rock mass and reduce rockfall. The reason for this effect is that the rock mass expansion on heating induces tangential compression around the excavations. This compression tends to provide increased normal stresses to fractures, thus increasing their shearing resistance as well as minimizing joint opening during extensional loading during a seismic event. Thus, the most conservative thermal state, from a rockfall standpoint, is actually when the rock is at or near ambient temperature.

5.3. Sensitivity Studies of the Input Parameters and Model Conditions

5.3.1 Fracture Surface Property Variation and Fracture Strength Degradation

The base-case joint properties, listed in Table 4, were based on the rotary shear tests of the cored rock specimens. Additional direct shear tests have been completed, and results from these tests are used to provide the range of shear strength variation tested in the sensitivity studies. With limited joint test results currently available and given the fact that the use of rotary shear devices in rock mechanics is not common, some of the parameters in the base case, such as cohesion and dilation angle, were scaled down from the testing results for conservatism, to allow for an investigation of parameter sensitivity on rockfall development.

A range of joint properties, as shown in Table 6, was selected for the sensitivity study. The values for joint categories 1 to 3 were established based on the residual friction angle of 30° and three tiers of dilation angles. The dilation angles were selected within the range of reported test results. The results of these sensitivity studies show that the variation of joint mechanical properties is a secondary effect compared with the variation of fracture geometrical properties (i.e., fracture pattern). Results for the three categories are quite similar, irrespective of the variation of the mechanical properties used for each category. Joint category 4 is used to represent the degraded joint condition. The reduced joint strength parameters are estimated to be in the range of the residual, post-peak shear displacement state with joint cohesion reduced to zero and the joint friction angle reduced to 30°. Dilation angle is also conservatively presumed to be zero, considering that the asperities on fracture surfaces had been sheared off. The net result of these conservative assumptions is the potential for greater rockfall. The degraded joint strength and dilatational properties were applied in three 1×10^{-5} annual probability of exceedance seismic motion cases that represent the case with the greatest amount of rockfall, the median case, and the case producing no rockfall. The predicted number of detached rock blocks and the total rockfall volume show that only a slight increase in rockfall is predicted for the degraded state. Thus, potential time-related joint strength degradation has a minor impact on drift stability in nonlithophysal rock.

Table 6. Four Categories of Joint Properties Used in the Sensitivity Study

Joint Category	Joint Cohesion (Pa)	Joint Dilation Angle	Peak Friction Angle	Joint Shear Stiffness (Pa/m)	Joint Normal Stiffness (Pa/m)
1	1.0×10^5	1.4	31.4	5.3×10^9	7.2×10^{10}
2	1.0×10^5	4.4	34.4	1.1×10^{10}	9.4×10^{10}
3	1.0×10^5	11	41	1.7×10^{10}	1.2×10^{11}
4	0	0	30	5.3×10^9	7.2×10^{10}

5.3.2 Rock Bridge Strength

Solid rock "bridges" between fractures were automatically generated as the extension of finite trace length fractures to form the distinct blocks in the 3DEC model. During a simulation, the stress conditions acting on these solid rock bridges are monitored, and failure in shear or tension can occur. Rock bridge damage either in shear slip or tensile separation appears to have a strong relationship with peak ground velocity. In general, less than 1% of the bridge area is damaged when subjected to 1×10^{-5} annual probability of exceedance ground motions, with about 5% bridge damage for 1×10^{-6} ground motions, reaching to 20% bridge damage for 1×10^{-7} ground motions. However, for certain large ground motions, much higher damage percentage is expected. Figure 14 shows the correlation between the damage percentage and the peak ground velocity.

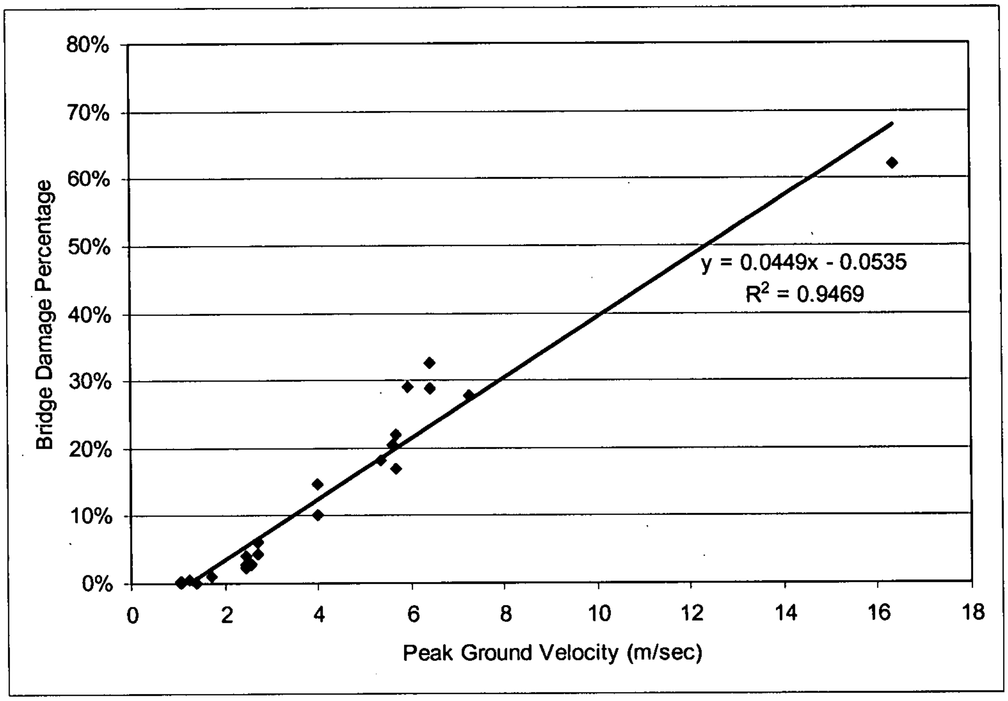

Figure 14. Correlation of Rock Bridge Damage Percentage and Peak Ground Velocity

A range of bridge strength parameters, in terms of cohesion, friction angle, and tensile strength, was selected for the sensitivity study. This range of intact rock properties was derived from the results of triaxial testing of rock cores from the Tptpmn. A total of 3 categories were included to cover the possible range of variation for bridge strength parameters and was subject to 1×10^{-5} annual probability of exceedance motions. The joint strength parameters are used for category 1 to represent the extreme case where all the bridges are sheared-off to become fractures. The mean values of the intact Tptpmn strength parameters are used for category 2. The mean-plus-one standard deviation values determined from triaxial testing are assigned as the strength parameters for category 3. This category represents the upper bound for the rock bridge strength. The results show that within the range of variation for the intact strength parameters (categories 2 and 3), rock bridge strength parameters have an insignificant impact on rockfall prediction. However, if all rock bridges are sheared-off, as represented by category 1, a significant increase of rockfall volume occurs with smaller rock block size.

5.3.3. Intact Block Failure Response Under Low-Probability Ground Motions

At the lower seismic hazard levels, the ground motions show extreme PGV levels, ranging from 2.44 m/s at the 1×10^{-6} to 5.35 m/s at the 1×10^{-7} annual exceedance probabilities. The calculations and estimates of dislodged block masses and volumes assumed that the rock blocks were, in general, elastic. The only block failure that was allowed was breakage of solid rock "bridges" that occur along the extension of fracture planes, between the end of the fracture and its possible termination against adjacent fractures. Thus, in the current model, it is possible for a block to split into several smaller blocks if the seismic stresses are sufficient to fail the rock bridge in shear or in tension.

A sensitivity study of rock bridge strength provides a conservative assessment of the case in which the tensile strength of the rock bridges is assumed to be zero. This case effectively represents the condition in which the tensile strength of the rock mass is conservatively assumed to be zero as no rock bridges exist. These analyses indicate that the rockfall volume increases between 3 to 5 times for the 1×10^{-6} and the 1×10^{-7} cases. The drift degradation profile for the base case rock bridge strength and the case in which the rock bridge tensile strength is set to zero are shown in Figure 15 for the 1×10^{-6} ground motions. As seen in this figure, the rockfall increases significantly with the assumption of zero rock bridge tensile strength, but total collapse is not evident.

6. Conclusions

This paper summarizes the geologic, laboratory, field, and numerical analysis work related to the mechanical degradation of the nonlithophysal rock mass surrounding the emplacement drifts of a proposed geologic repository at Yucca Mountain. A drift degradation model for nonlithophysal rock was developed using the three-dimensional discontinuum code 3DEC for the planned repository emplacement drift at Yucca Mountain. This model includes the development of fracture patterns generated from multiple sampling from a synthetic rock mass volume that contains a realistic fracture population based on field mapping data. Site-specific ground motion time histories, with annual probabilities of exceedance ranging from 1×10^{-4} to 1×10^{-7}, are included in the model.

Degradation in the nonlithophysal units is primarily controlled by geologic structure. Ground motion with an annual probability of exceedance of 1×10^{-4} results in minor drift damage due to rockfall even with the assumption of unsupported drift openings. Ground motions with annual probabilities of exceedance from 1×10^{-5} to 1×10^{-7} result in varying extent of drift damage due to rockfall, with localized areas of rock failure sufficient to cover the drip shield.

Thermal-mechanical analyses were conducted using both a base case set of thermal properties and a sensitivity case considering the values for thermal conductivity and specific heat one standard deviation smaller than the mean. The transient temperature field around the repository was calculated using 90% and 70% ventilation heat removal efficiencies. There was minimal rockfall predicted at any time for the thermal only scenario (i.e., no seismic loading) for the cases analyzed. When thermal stresses were considered in combination with the stresses resulting from postclosure seismic ground motion, it is clearly shown that thermal loading reduces the amount of rockfall.

Drift stability due to the effect of time-dependent rock joint degradation is assessed based on a reduction of joint cohesion and friction angle. The reduced joint strength parameters are estimated to be in the range of the residual state with joint cohesion reduced to zero and the joint friction angle reduced to 30°. Dilation angle is also reduced to zero considering that the asperities on fracture surfaces had been sheared off. The degraded joint strength and dilational properties were applied, while a slight increase in rockfall is predicted for the degradated state. Overall, joint strength degradation has a minor impact on drift stability.

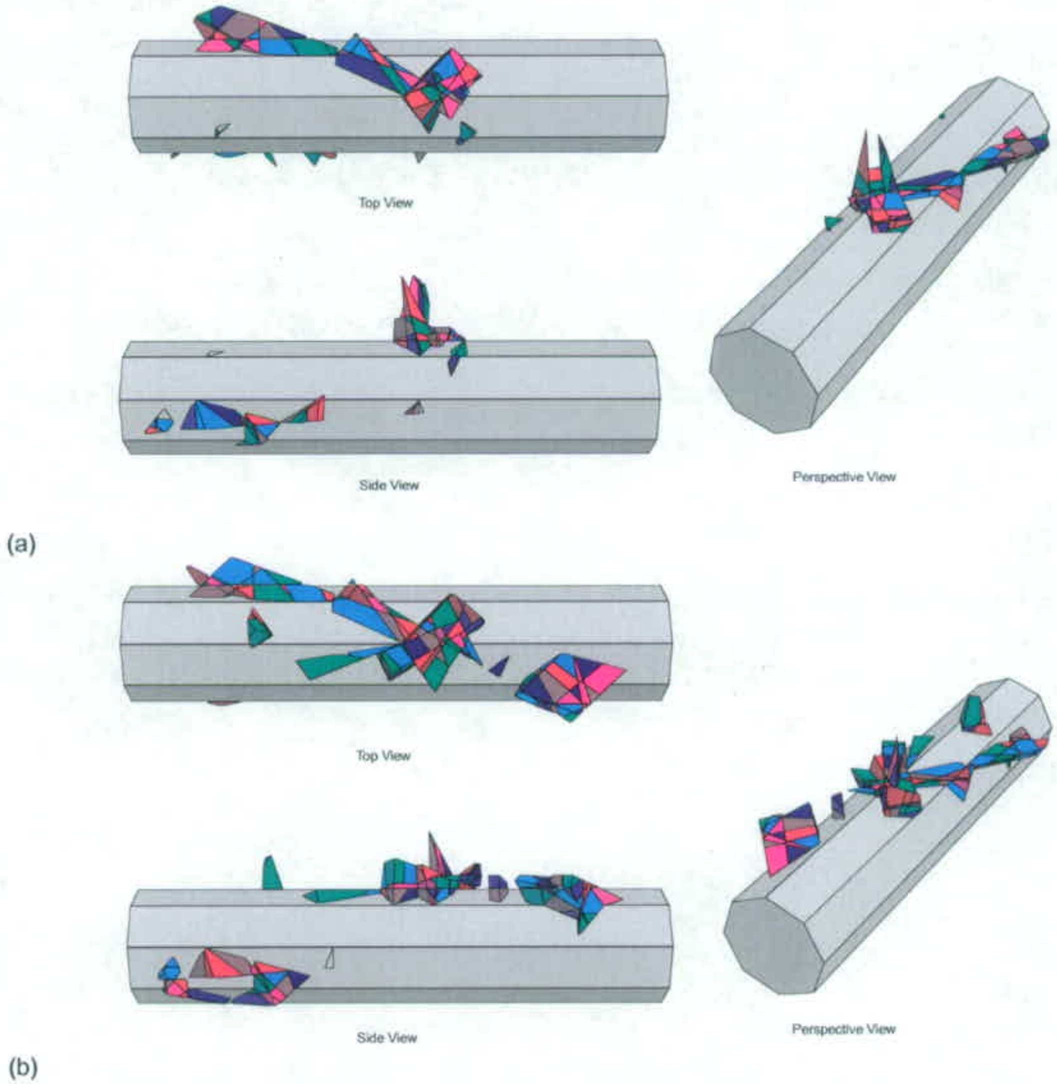

Figure 15. Three-dimensional Visualization of Rockfall for the Median Rockfall Condition: (a) Base Case and (b) Low Rock Bridge Strength Properties, 1×10^{-6} Ground Motion

7.0 References

Bechtel SAIC Company 2003. *Subsurface Geotechnical Parameters Report.* 800-K0C-WIS0-00400-000-00A. Las Vegas, Nevada: Bechtel SAIC Company.

Bechtel SAIC Company 2004a. *Yucca Mountain Site Description.* TDR-CRW-GS-000001 REV 02 ICN 01. Two volumes. Las Vegas, Nevada: Bechtel SAIC Company.

Bechtel SAIC Company 2004b. *Drift Degradation Analysis.* ANL-EBS-MD-000027, Rev. 03. Las Vegas, Nevada: Bechtel SAIC Company.

Bechtel SAIC Company 2004c. *Sampling of Stochastic Input Parameters for Rockfall Calculations and for Structural Response Calculations Under Vibratory Ground Motion.* ANL-EBS-PA-000009 REV 01. Las Vegas, Nevada: Bechtel SAIC Company.

Bechtel SAIC Company 2005. *Peak Ground Velocities for Seismic Events at Yucca Mountain, Nevada.* ANL-MGR-GS-000004 REV00. Las Vegas, Nevada: Bechtel SAIC Company.

CRWMS M&O 1998. *Geology of the Exploratory Studies Facility Topopah Spring Loop.* BAB000000-01717-0200-00002 REV 01. Las Vegas, Nevada: CRWMS M&O.

Dershowitz, W.S. 1984. *Rock Joint Systems.* Ph.D. Thesis, Massachusetts Institute of Technology.

Itasca Consulting Group 2002. *Itasca Software–Cutting Edge Tools for Computational Mechanics*. Minneapolis, Minnesota: Itasca Consulting Group.

Mongano, G.S.; Singleton, W.L.; Moyer, T.C.; Beason, S.C.; Eatman, G.L.W.; Albin, A.L.; and Lung, R.C. 1999. *Geology of the ECRB Cross Drift - Exploratory Studies Facility, Yucca Mountain Project, Yucca Mountain, Nevada.* [Deliverable SPG42GM3]. Denver, Colorado: U.S. Geological Survey.

Mechanical degradation of emplacement drifts at Yucca Mountain—A case study in rock mechanics.
Part II: Lithophysal rock

B. Damjanac[a], M. Board[a], M. Lin[b*], D. Kicker[b], J. Leem[b]

[a]*Itasca Consulting Group Inc., 111 Third Avenue South, Suite 450, Minneapolis, MN 55401, USA*
[b]*Bechtel SAIC Company, 1180 Town Center Dr, Las Vegas, NV 89144, USA*

Abstract – This paper outlines rock mechanics investigations associated with mechanical degradation of planned emplacement drifts at Yucca Mountain, which is the designated site for a U.S. high-level nuclear waste repository. The welded tuff emplacement horizon consists of two groups of rock with distinct engineering properties: nonlithophysal and lithophysal units, based on the relative proportion of lithophysal cavities. Part I of the paper concentrated on the degradation behavior of the generally hard, strong, and fractured nonlithophysal rock. Part II concentrates on the host rock in the lithohpysal units. Lithophysal rock is characterized by lithophysal cavities interconnected by fracturing. Fracture sets are not as clearly defined as in the nonlithophysal rock. The rock mass porosity in the lithophysal units has been shown to be the primary physical factor that governs elastic and strength properties. The degradation behavior of the tunnels in the lithophysal rock is controlled by the spalling of the surrounding rock mass. A discontinuum material model has been developed to represent the drift scale rock mass properties in which slip and separation of contacting rock blocks can be estimated. Two-dimensional discontinuum analyses were developed with the consideration of *in situ*, thermal, and seismic loads. Time-dependent degradation was also considered. In this study, field and laboratory data and numerical analyses are well integrated to provide a solution for the unique problem of modeling drift degradation throughout the regulatory period for repository performance.

1. Introduction

Yucca Mountain is located on federal land on and adjacent to the Nevada Test Site in Nye County, Nevada. It has undergone comprehensive site characterization activities for gathering site information beginning in May 1986. In 2002, the site was designated as the U.S. repository for high-level nuclear waste.

Degradation of underground openings as a function of time is a natural and expected occurrence for any subsurface excavation. Over time, changes occur to both the stress condition and the strength of the rock mass due to several interacting factors. Once the factors contributing to degradation are characterized, the effects of drift degradation can typically be mitigated through appropriate design and maintenance of the ground support system. However, for the emplacement drifts of the geologic repository at Yucca Mountain, it is necessary to characterize drift degradation over a 10,000-year period or more, which is well beyond the functional period of the ground support system. This paper provides a summary of the study of the stability of repository excavations in

---

[*] Corresponding author. Tel.: 1-702-295-4830; fax:+1-702-2955-98 E-mail address: ming_lin@ymp.gov

lithophysal tuff and potential mechanical degradation under the action of *in situ*, thermal, and seismic stresses during the first 10,000 years of repository performance.

2. Site Geology and Geotechnical Characteristics of the Lithophysal Rock

The entire repository is currently designed to be located in densely welded and crystallized volcanic tuff with approximately 15% of the repository in nonlithophysal tuff and 85% in lithophysal tuff. Lithophysal tuff contains hollow, bubble-like cavities composed of simple or concentric shells of finely crystalline alkali feldspar, quartz, and other minerals. The rock material in both the lithophysal and nonlithophysal tuffs consists of fine-grained intergrowths of alkali-feldspar, and SiO_2 polymorphs of quartz, and cristobalite. Although the mechanical and thermal properties of the rock material in these lithophysal and nonlithophysal tuffs is rather uniform throughout the repository horizon, the occurrence of lithophysal cavities results in very different internal structures and mechanical behaviors. Compared to lithophysal rocks, nonlithophysal rocks are slightly finer grained, more homogeneous with no lithophysae in several tens to hundreds of square meters of exposed rock, stronger, and fractured by four moderately to well-developed joint sets. In contrast, lithophysal rocks have porosity in the range of 2% and 30% in the form of lithophysal cavities, are weaker, and have more small-scale fractures. Lithophysal rocks display fractures of similar orientation to the nonlithophysal, but with much more poorly developed fracture sets.

Because a large portion of the repository is located in the lower lithophysal zone, a detailed study of the lithostratigraphic features in the lower lithophysal zone exposed in the Enhanced Characterization of the Repository Block (ECRB) Cross-Drift (see Figure 1 in Part I of the paper) has been completed. The data document the distributions of size, shape, and abundance of lithophysal cavities, rims, spots, and lithic clasts.

In addition to the variation along the tunnel in the abundance of features such as lithophysae, there are variations in the sizes, shapes, and distances between features. These types of variations are observed most easily with panel map data (Figure 1), which have been converted into porosity variations as functions of distance along the exploratory cross-drift through the entire lower lithophysal zone (Tptpll) subunit (e.g., Figure 2). Lithophysal porosity varies in a bedded or stratiform fashion with layering orientation coincident with the dip of the Tptpll. For example, the areas of highest lithophysal porosity (i.e., greater than about 20%) lie in a thin band in the upper portion of the Tptpll unit, just below the contact with the middle nonlithophysal zone (Tptpmn). Here, the largest lithophysae are also found. The lowest levels of lithophysal porosity are found near the bottom of the Tptpll where it grades into the lower nonlithophysal subunit (Tptpln). This information provides direct input to mechanical degradation studies in the following ways.

- Panel maps, porosity, and the size and shape variations of lithophysae provide the basis for numerical estimation of the impact of lithophysae on rock mass properties.

- Rock mass properties in the lithophysal rock are primarily a function of porosity, and variation in porosity assessed by direct panel mapping allows the variation in rock mass properties to be estimated.

Lithophysal porosity has been shown to be the primary physical factor that governs the elastic and strength properties of the densely welded and crystallized tuff (Price 1983; Price and Bauer 1985). A series of large core (267-mm- to 290-mm-diameter) samplings of the upper and lower lithophysal units (Tptpul and Tptpll) were taken in the Exploratory Studies Facility (ESF) to obtain more representative samples of lithophysal rocks. The objective was to obtain samples that had a number (approximately 3 to 5) of lithophysae across a sample diameter. Drilling of such large core in this material is quite difficult due to the tendency of the core to break in shear when a large or poorly placed lithophysae is encountered. Figure 3 shows a series of these samples as prepared for laboratory compression testing. Approximately 20 samples were tested at varying environmental conditions, including air dried, saturated under vacuum, and at 200°C. Figure 4 plots the unconfined compressive strength and Young's modulus as functions of the approximate levels of lithophysal porosity[1]. In these results, the unconfined compressive strength and Young's Modulus are relatively insensitive to lithophysal porosity above approximately 20%, with rapid increase in both for lithophysal porosities below about 15%. As was shown previously via field measurement in the cross-drift (Figure 2), lithophysal porosity through the Tptpll averages approximately 15%, with a range from about 10% to 25%. The laboratory-scale unconfined compressive strength of the Tptpll can vary from as high as about 25 MPa to 30 MPa to as low as about 10 MPa, while the Young's modulus can vary from 5 GPa to 20 GPa.

---

[1] Lithophysal porosity is approximate, as it was estimated from core surface measurements.

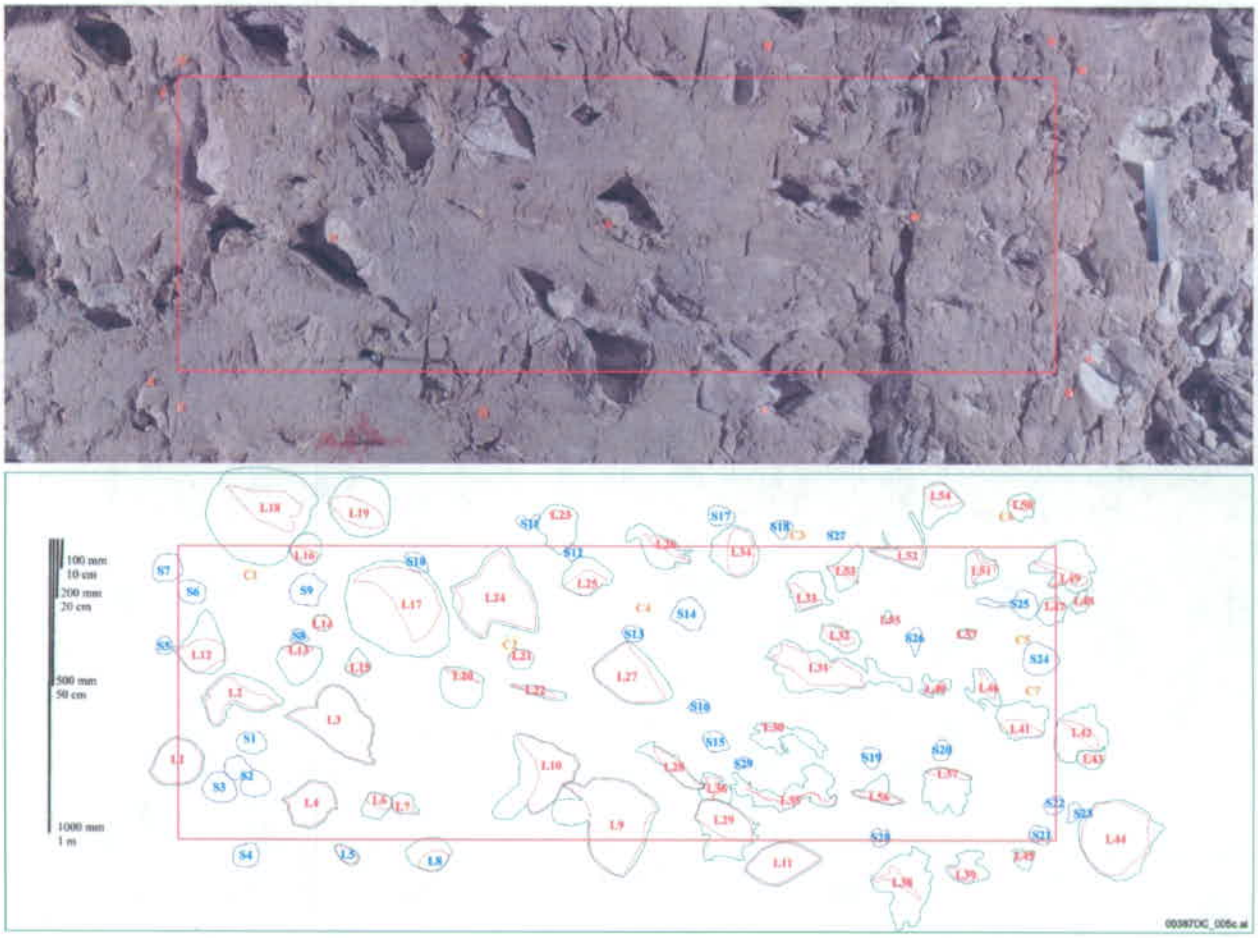

Figure 1. Lithophysae of Tptpll in Panel Map 1493 Located in ECRB Cross-Drift on the Right Rib from Station 14+93 to 14+96

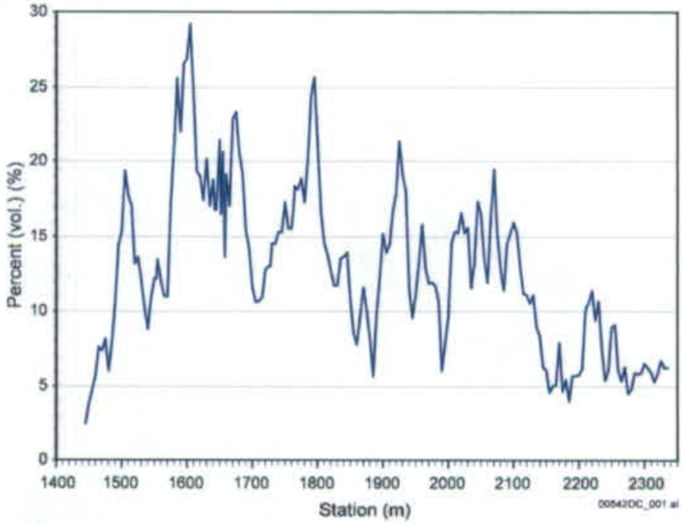

Figure 2. Mapped Lithophysal Porosity in the Lower Lithophysal Zone (Tptpll) Exposed Along the Exploratory Cross-Drift

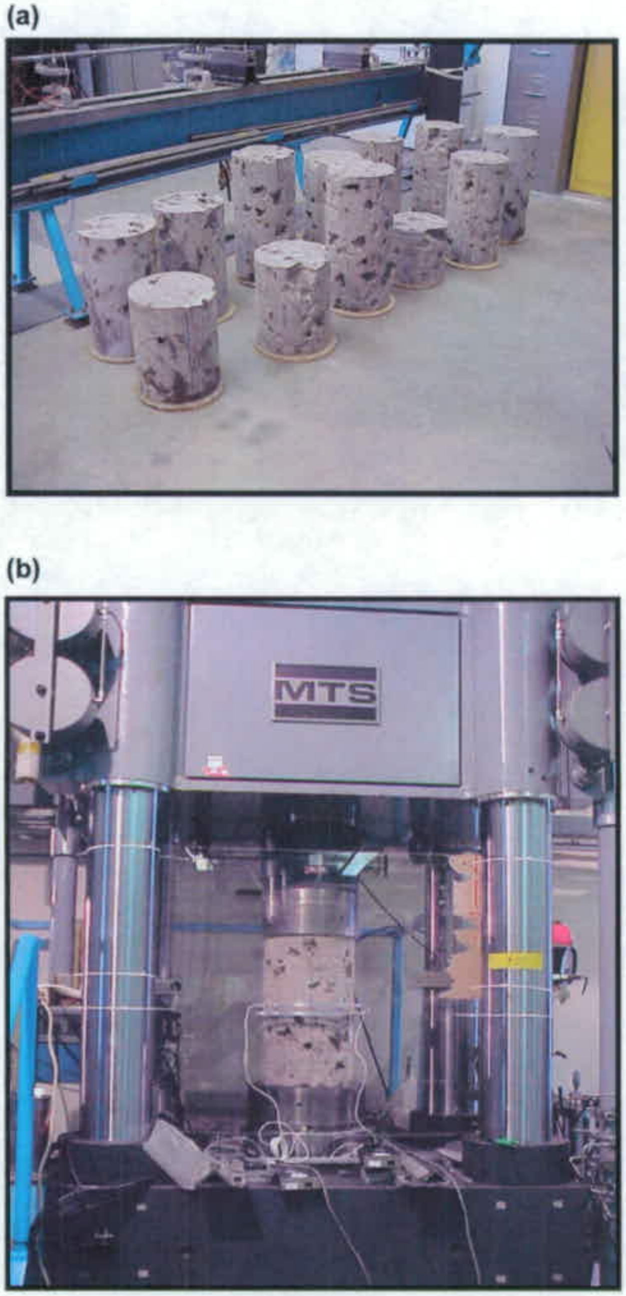

Figure 3. Photographs of Large Lithophysal Core Samples from the Tptpll and Tptpul (a) and a Sample under Uniaxial/Unconfined Compression Loading Conditions (b)

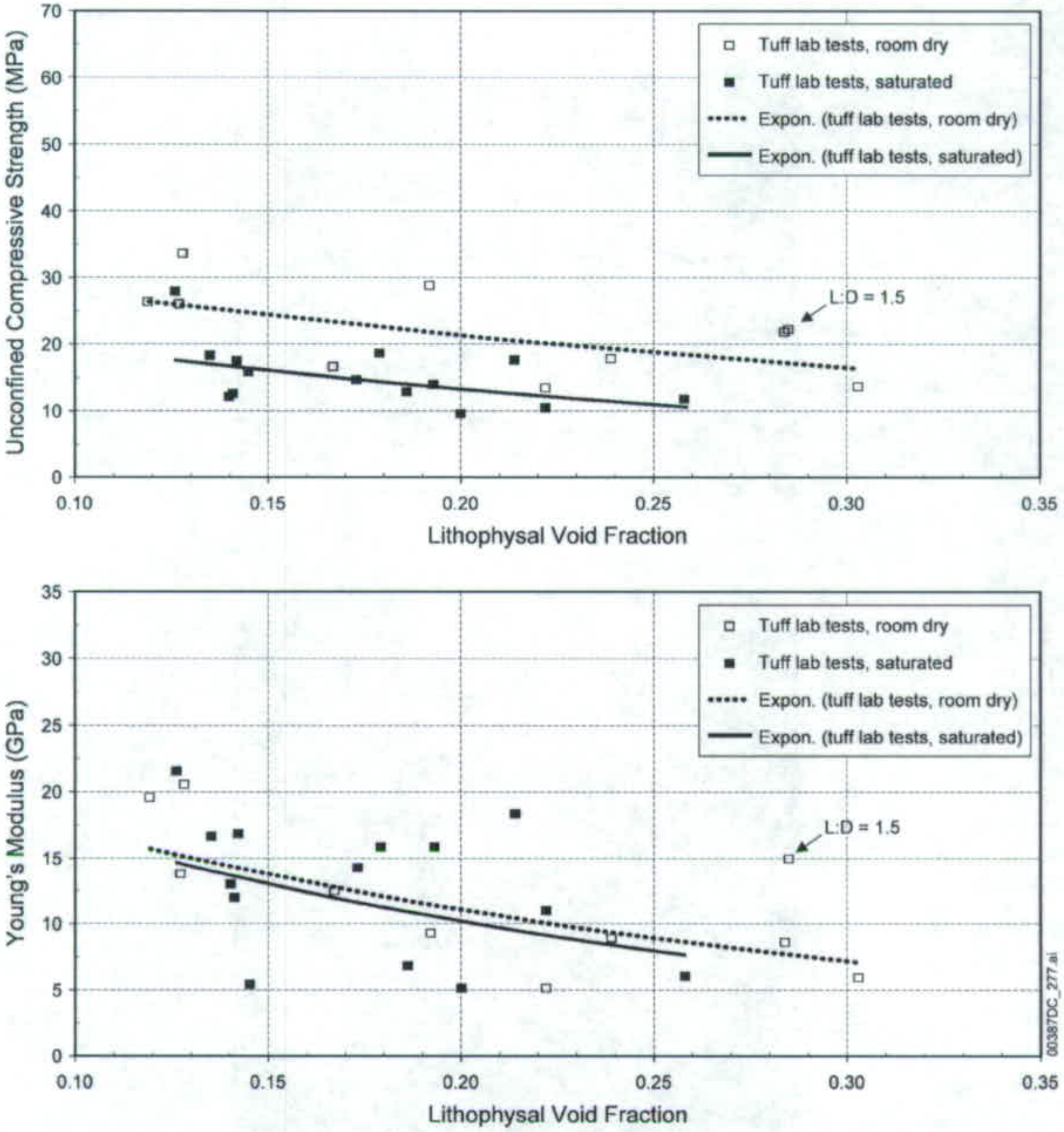

Figure 4. Unconfined Compressive Strength and Young's Modulus as Functions of Estimated Lithophysal Porosity from Large Core (290-mm diameter) Compression Tests from Lithophysal Rocks

3. General Approach

Analysis of rockfall in the lithophysal units presents a significantly different problem than that given in the first part of this paper with regard to nonlithophysal rocks. In general, the nonlithophysal rocks are composed of strong, intact blocks of welded tuff that are separated by fracture planes. The fracture surfaces provide the primary weaknesses in the system and control the failure mode and resulting rock-block dimensions. For this reason, it is necessary that the fracture planes be explicitly represented within the model to allow estimation of block dimensions, masses, and velocities. Lithophysal rock is characterized by lithophysal voids interconnected by intense fracturing. Fracture sets are not as clearly defined as in the nonlithophysal rock. In addition to fracturing on different scales, the lithophysal rock mass is characterized by the presence of almost uniformly distributed holes (lithophysae) of varying size (from less than 1-cm to greater than 1-m in diameter). Lithophysae and fractures tend to create blocks with dimensions on the order of about 10 cm or less. The lithophysae account for up to about 30% of the rock mass volume. The size of the internal lithophysae structure and fracture spacing is much smaller than the drift size (i.e., 5.5-m diameter). It is assumed that the lithophysal rock mass will break into relatively small block sizes controlled by the spacing of natural fractures when stressed beyond its strength limits. Therefore, as opposed to the 3DEC modeling of the nonlithophysal rock, the modeling of the lithophysal rock does not attempt to calculate the block sizes resulting from yield but considers them to be on the order of 0.1 m to 0.3 m (or smaller) in dimension. The models developed here are discontinuum models in which the rock mass is discretized into random block sizes with dimensions on the order of 0.1 m to 0.2 m. Use of a two-dimensional UDEC (Itasca Consulting Group 2002) modeling approach is justified for lithophysal rocks based on the lack of anisotropy in the rock mass and the fact that the block sizes created upon failure are small with respect to the size of the emplacement drift.

The approach to modeling mechanical degradation and rockfall from combined *in situ*, thermal, and seismic loading in lithophysal rock is illustrated in Figure 5. The standard approach in geotechnical engineering for solving problems of stability of underground excavations is through the use of models based on equivalent continuum mechanics. Such an approach is quite effective if the main interest is estimating stress redistribution around an opening or solving for tunnel wall displacements. However, the estimation of rockfall requires that the modeling technique and mechanical material model be capable of representing fracture and separation of the intact rock mass into individual blocks of material. Thus, the modeling technique must be based on use of a discontinuum numerical method (i.e., a method in which the rock is represented as blocks separated by fracture surfaces in which slip and separation of contacting rock blocks can be estimated).

The development of a mechanical material model and estimate of property ranges for the lithophysal rock is based on use of the laboratory and *in situ* test data, geologic mapping, and supplemented by numerical model extrapolation using the PFC and UDEC discontinuum programs (Itasca Consulting Group 2002). Detailed description of the lithophysal material model is provided in the Section 4.

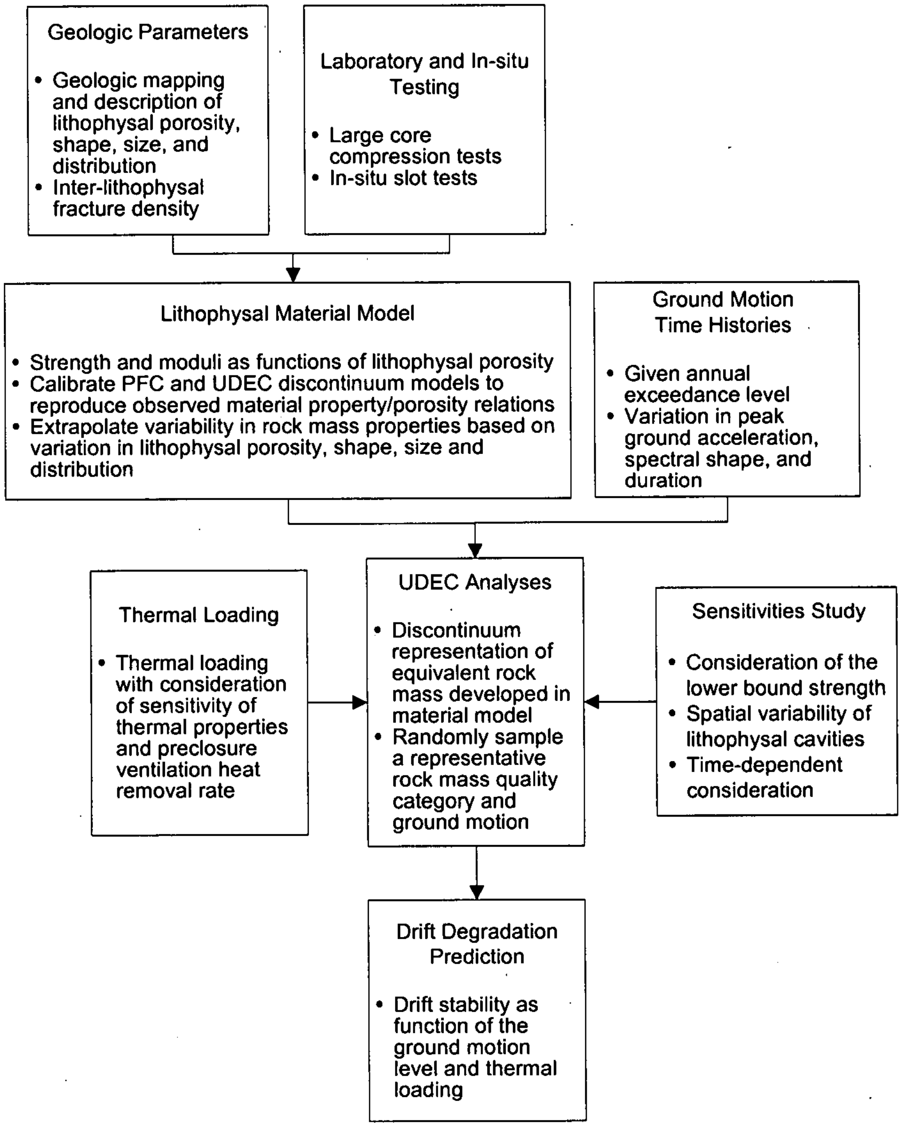

Figure 5. Approach of Drift Degradation and Rockfall Analyses for Lithophysal Rock

4. Development of Rock Mass Material Model for Lithophysal Rock

Typically, development of a mechanical material model for a rock mass is based on extensive laboratory testing of the rock core and determination of strength and moduli reduction factors via *in situ* mapping of rock quality, followed by validation against field measurement. Such an approach for lithophysal rock presents a number of challenges. It is difficult to conduct an extensive mechanical properties testing program on lithophysal rock due to the requirement to obtain and test large cores or to create large *in situ* samples by sawing or drilling. Additionally, direct determination of the true triaxial stress behavior of lithophysal samples is problematic, as pressure vessels to provide confinement to very large core samples typically are not available. It is also not possible to conduct testing on a wide range of lithophysae shapes and size distributions. Finally, empirical methods for rock-mass property estimation based on geotechnical classification systems are not applicable to lithophysal rock due to lack of experience in excavation and laboratory testing of this particular type of rock mass.

The database available for model development includes: (1) uniaxial and triaxial compression and indirect tensile strength testing of nonlithophysal rock; and (2) uniaxial compressive strength testing of a limited number of large-scale cores and *in situ* blocks of lithophysal tuff. To supplement the sampling and testing for lithophysal rock, an alternative strategy is also used here. Two discontinuum numerical modeling programs, PFC and UDEC (Itasca Consulting Group 2002), first are calibrated against the existing laboratory compressive strength data, demonstrating that a detailed understanding of the basic physical mechanisms of the rock mass behavior can be obtained without resorting to empiricism or complex constitutive modeling. These programs were chosen because of their ability to simulate the physics of deformation and fracture of a bonded granular matrix that contains void space of varying shape, size, and porosity. Using two different approaches provides a check to, and greater confidence in, the modeling. The UDEC program is used because it also allows grains that are nonspherical in shape and thus overcomes some simplifications used in the PFC approach; specifically, it allows greater flexibility in modeling failure mechanisms under triaxial compression.

The models then are used to extend the laboratory data by conducting numerical experiments on simulated samples of lithophysal tuffs at various physical conditions of porosity, lithophysae shape and distribution, as well as various levels of confinement and applied stress. From this modeling, it is possible to understand the size scaling and variability issues introduced by lithophysae shape and distribution and their impact on rock mass properties and failure criteria. The material model developed from the combined laboratory testing and the PFC/UDEC extrapolation is embedded in a drift-scale UDEC model for examination of emplacement drift stability.

4.1. Generalization of Lithophysal Rock Mass Properties into Rock Quality Categories

In the lithophysal units, lithophysal porosity is the primary physical feature impacting rock quality conditions (and therefore rock mass strength and stiffness). As seen in Figure 6, the laboratory data shows a range in unconfined compressive strength from approximately 10 MPa to 30 MPa with a corresponding range in Young's modulus from approximately 5 GPa to 20 GPa. The estimated sample lithophysal porosity varies from approximately 10% to 30% over this range, or is approximately comparable to the range of *in situ* values defined from mapping in the cross-drift (Figure 2). Thus, the core sampling used for the laboratory testing spans approximately the same range of lithophysal porosity as observed throughout the cross-drift.

For convenience of analysis, the mechanical rock properties range, as shown in Figure 6, is subdivided into five rock quality "categories" that cover the entire range of large-core laboratory testing and *in situ* testing results. Table 1 presents these strength and moduli ranges derived by subdividing the laboratory data into five categories with an unconfined compressive strength increment of 5 MPa. The associated Young's modulus for each unconfined compressive strength is derived from the linear data fit to the 290-mm core data given in Figure 6. The approximate equivalent lithophysal porosity for each of these ranges is given in Table 1.

It is considered that, by conducting numerical analyses with this entire range of data, all levels of rock quality and rock mass response from lowest to highest porosity ranges and size effects can be covered. A histogram constructed to provide the information on the percentage of each rock category in the Tptpll as a whole is shown in Figure 7. The distribution of lithophysal porosity is based on the lithophysal mapping data in the cross-drift as presented in Figure 2. It is shown that approximately 90% of the mapped rock quality is equal or better than the category 3 rock. Categories 1 and 2 are related to localized, stratiform, high-porosity zones that occur particularly near the top of the Tptpll. Although of low abundance, categories 1 and 2 are included in the range of rock properties for analysis to test the conservative bounds of rock strength. Figure 7 also shows photographs of example panel maps that illustrate lithophysal porosity levels characteristic of categories 3, 4, and 5.

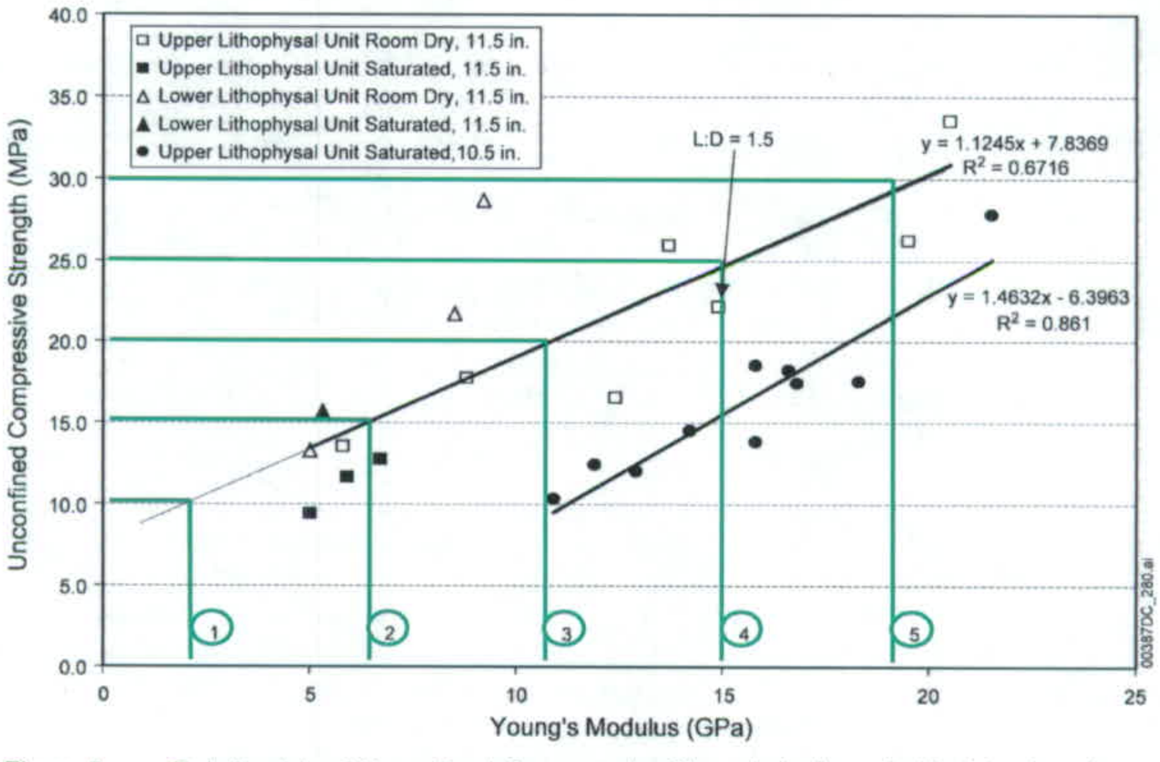

Figure 5. Relationship of Unconfined Compressive Strength to Young's Modulus from Large Core Testing of Lithophysal Rock (Figure 3) and Assignment of Five Average Quality Categories

Table 1. Suggested Range of Mechanical Properties Selected for Base-Case Analyses

Rock Quality Category	Unconfined Compressive Strength (MPa)	Estimated Young's Modulus (GPa)	Approximate Lithophysal Porosity From Laboratory Tests (%)
1	10	1.9	35 ± 8
2	15	6.4	28 ± 6
3	20	10.8	21 ± 4
4	25	15.3	13 ± 5
5	30	19.7	7 ± 7

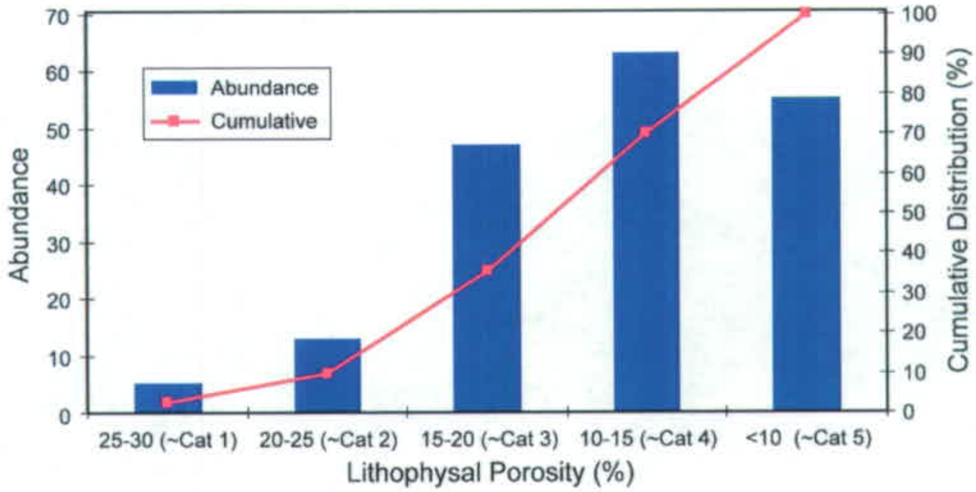

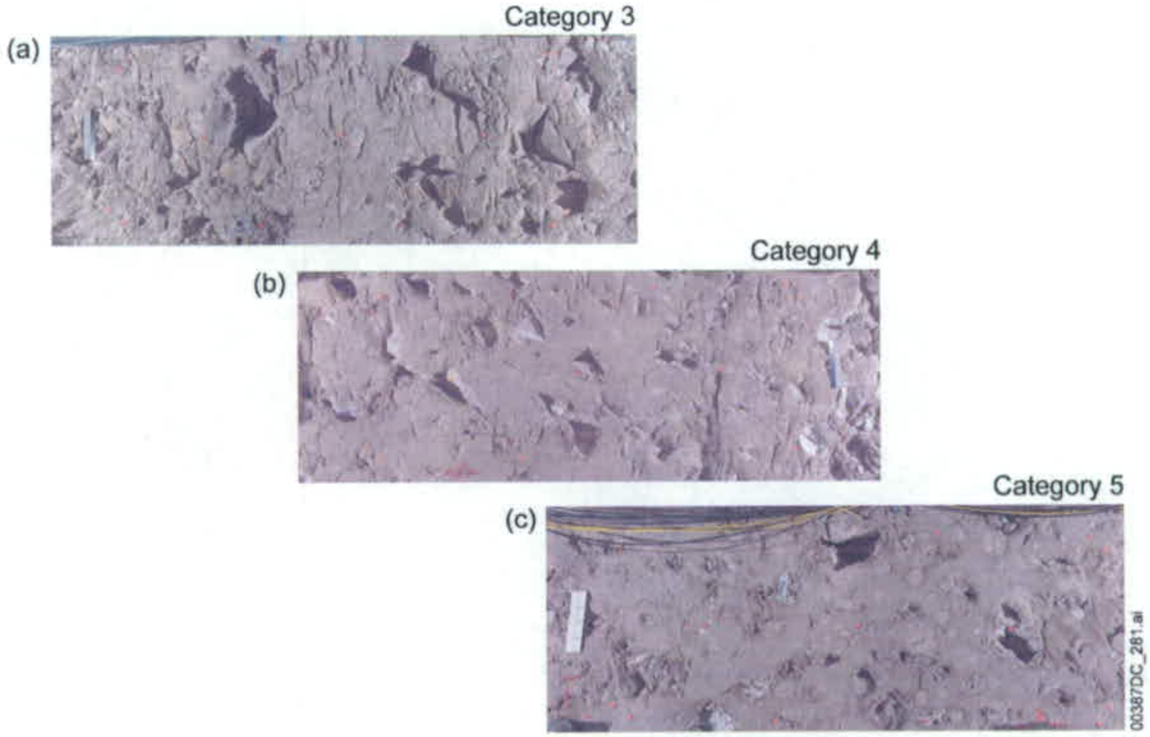

NOTES: Lithophysal porosity data are from cross-drift station 14+44 to 23+26. Examples of approximate rock strength category levels taken from 1x3-m panel maps: Category 3 (a) with lithophysal porosity of approximately 19%; Category 4 (b) with lithophysal porosity of 13.3%; and Category 5 (c) with lithophysal porosity of 8.5%.

Figure 7. Distribution of Lithophysal Porosity and Estimated Rock Properties Categories for the Tptpll in the Enhanced Characterization of the Repository Block Cross-Drift

4.2. Micro-Mechanical Models of the Lithophysal Rock Mass

The PFC approach represents rock as a number of small, rigid, spherical grains that are either bonded together at their contacts with shear and tensile strengths or that interact by a grain-to-grain friction angle after the "contact bond" has been broken. The deformability of the contacts between particles is represented by normal and shear stiffnesses at the contact point. Porosity is developed naturally in the model by control of the shape and size of void space between chains of bonded grains. The contact properties and porosity distribution are referred to as "microstructural" properties. Thus, the input conditions necessary for the model are very simple: only contact strength and stiffness. However, as shown below, extremely rich constitutive behavior may develop naturally based on porosity and the few straightforward input properties and their variability throughout the rock.

When load is applied to the grain assembly, forces are transmitted across contacts. If the shear or tensile strength of the contact is reached, failure will occur, and the adjacent particles are free to slide past one another, or to separate. In either case, a fracture is formed, and the forces must reorient in some fashion, thus redistributing loads. Realistic failure mechanisms may develop that can be compared to those observed in the laboratory. Calibration of the model against laboratory testing is necessary and is conducted via sensitivity studies in which the contact strength and stiffness values are varied and the macroscopic stress–strain response is compared to that monitored.

The UDEC approach, although similar, is different specifically in that the grains may be of any arbitrary shape and in that the contacts between grains are not point-force contacts, but contacts across a plane. Additionally, the UDEC grains may be deformable rather than rigid.

4.2.1. PFC Micro-Mechanical Model

The PFC model has been calibrated against the large-core laboratory testing data. Sample numerical compression experiments were conducted for nonlithophysal and lithophysal tuffs using the same matrix properties derived by calibration of strength and modulus for a mid-range (approximately 15%) lithophysal void porosity (Figure 8). The nonlithophysal samples show a typical shear-failure mechanism, as evidenced by the coalescence of extension cracks to form major shear fractures. The model also shows highly linear (elastic) response just to the point of rock failure, followed by a brittle post–peak failure response due to the uniformity of bond strength set in the samples. This replicates the observed laboratory behavior of nonlithophysal samples as a result of the uniformity of the fine-grained, high silica content matrix. Simple circular holes with a uniform spatial distribution were added to the model, and the correspondence between laboratory-derived strengths, modulus and porosity was examined. The model showed good comparison with the general magnitude and trend of laboratory strength and modulus data (Figure 9). One conclusion of this initial work with the simplistic void porosity model is that the primary strength-decreasing effect of the lithophysae is due to the formation of tensile splitting between neighboring lithophysae under compressive load. As porosity increases, the spacing between lithophysae decreases; thus, there is a greater propensity for tensile splitting at lower applied forces. The tensile-splitting mechanism results in an increasingly less brittle post–peak response with increasing porosity. Additionally, the same matrix strength provides a reasonable fit to both nonlithophysal and lithophysal laboratory data (i.e., the void porosity is the primary driver in the mechanical properties reduction, not mineralogical differences in lithophysal and nonlithophysal rocks).

Further numerical testing was performed in which all of the actual lithophysal panel maps generated in the underground excavations (e.g., the cross-drift) were discretized and used as compression test "specimens" for the model (Bechtel SAIC Company 2004). As seen in Figure 8, the complex shape, size, and distribution of lithophysal voids result in the same general failure mode (tensile splitting between voids) and the same general trend of strength and modulus to void porosity (Figure 9). However, the variability tends to be greater primarily due to shape and distribution of voids. This is particularly true when the sample lithophysal porosity is lower (e.g., around 10% to 15%). A few large voids with uneven distribution through the sample can result in lower strength, whereas widely spaced voids in a finite sample size can result in higher strength than the same sample with uniformly distributed voids. The result of all strength testing on both the simplest, circular void cases and the more complex, realistic shapes can be summarized as follows.

- The PFC model shows that the mechanism for strength reduction from nonlithophysal to lithophysal rock results from tensile splitting of solid rock bridges between lithophysal voids. The smaller these rock bridges, the greater the strength reduction.

- The PFC model and laboratory data show reasonable agreement with respect to strength and modulus changes with lithophysal porosity. Strength and modulus show a generally logarithmic decrease with lithophysal porosity.

- Models with circular voids that are distributed uniformly through the rock mass show less scatter and a more uniform relation of mechanical properties to lithophysal porosity.

- Models with lithophysal voids with complex, irregular size and shape distribution show the same general trends as the circular void models, but with greater scatter of the strength or modulus. This scatter is greater for lower lithophysal void porosity, as might be expected, and may account partially for the obvious size effect observed in the laboratory and *in situ* scale testing.

PFC model calibration shows that a viable tool has been developed to simulate the mechanical response of lithophysal tuff to applied stress.

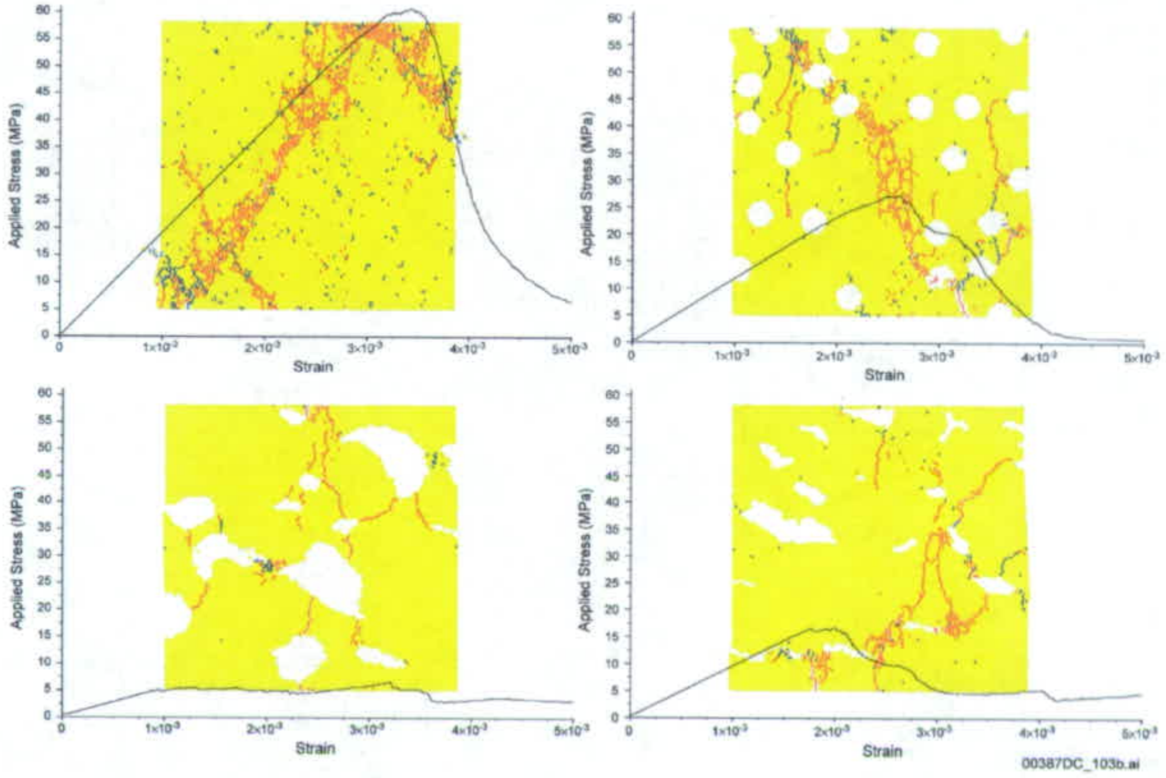

NOTES: Nonlithophysal welded tuff (upper left) is calibrated to provide matrix properties. Circular holes (upper right) provide a simple model of lithophysae, whereas lower models provide more realistic (hand-stenciled and digitized) shapes from Tptpll panel maps. Nonlithophysal rock fails in a brittle fashion through propagation of a major shear fracture (composed of small tensile fractures) through the sample. Lithophysal samples fail due to tensile splitting (Each red line is a bond breakage between small particles) between holes. Variability in lithophysal strength arises due to the abundance, shape, and distribution of holes throughout the sample.

Figure 8. PFC Calibration Experiment Samples and Respective Unconfined Stress–Strain Curves for Cases of Circular and Stenciled Lithophysae Shapes

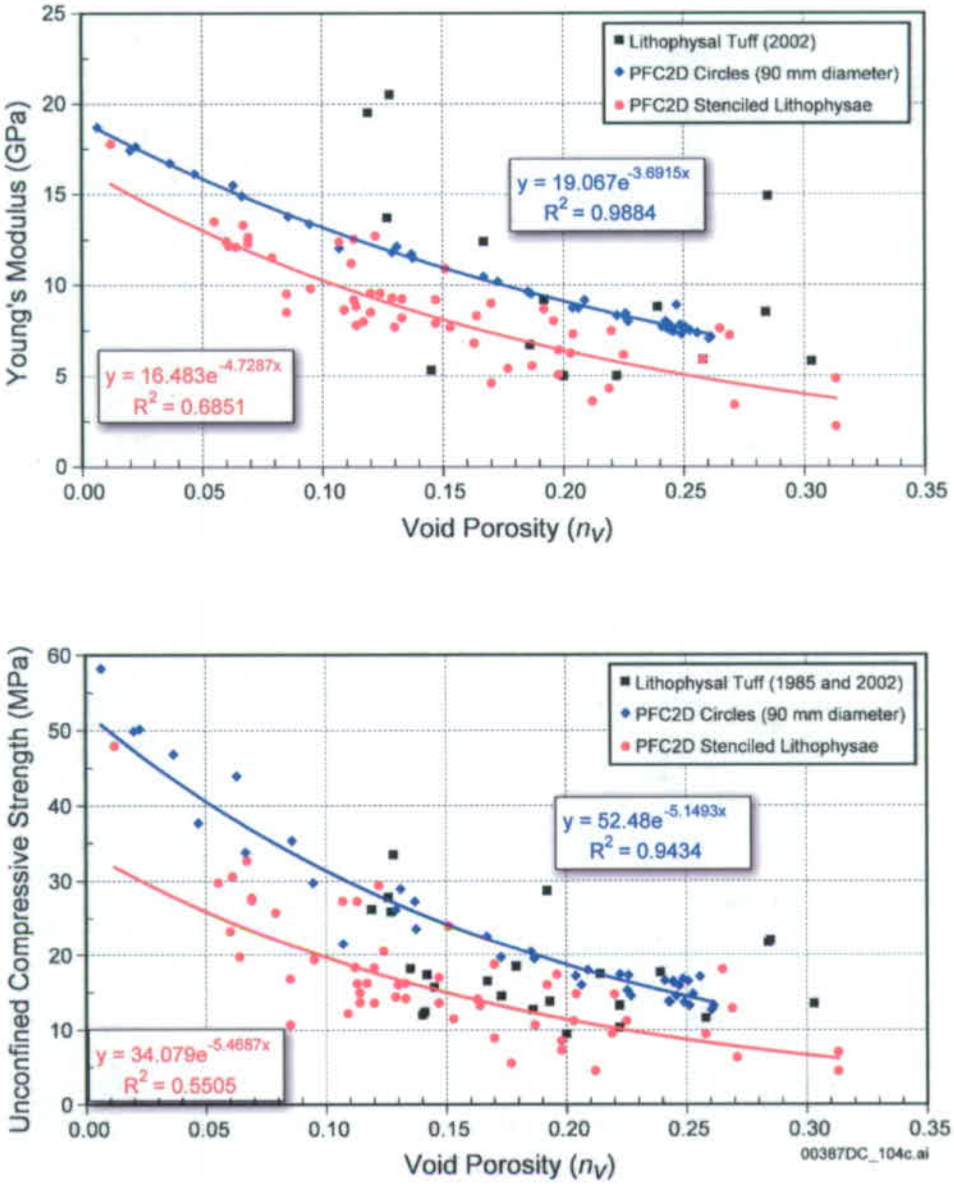

NOTES: There is greater variability in the strength of the PFC samples for a given porosity when true lithophysae shapes are introduced. This effect is particularly large at low porosities due to the greater variability of distribution and solid bridge lengths between lithophysae in a given sample volume.

Figure 9. Plots Showing Data from Large-Core Compression Testing of Tptpul and Tptpll Compared to Particle Flow Code Simulations Using Circular-Shaped Lithophysae as well as Actual "Stenciled" Shapes from the Cross-Drift Geologic Panel Maps

4.2.2. UDEC Micromechanical Model

The previous PFC calibration and analysis describe the basic comparison of the uniaxial compression behavior and modulus of lithophysal rocks. Triaxial laboratory experiments have not been conducted on representative lithophysal samples due to the size of the sample and the associated difficulties in obtaining pressure vessels and confining jacketing systems for samples with cavities. An understanding of the confining pressure response is necessary for assessing how the basic rock-mass failure parameters (rock-mass cohesion, angle of internal friction, and dilatancy) are affected by lithophysal porosity. Because of its more general particle-shape capability, UDEC, a discontinuum program similar in many respects to PFC, is used to investigate the effect of confinement on strength of lithophysal rock mass. The circular particle geometry employed by PFC simplifies the numerical algorithms, making it a good tool for conducting many parameter studies, as shown in the previous calibration studies. However, the particle geometry also restricts the ability to examine the effect of confinement and post–peak failure mechanisms in detail due to the dilational response of a circular particle model—this is not the case for the more general UDEC approach.

A series of uniaxial and triaxial compression and extensional experiments is conducted on samples with circular lithophysal voids added randomly to create samples of 10.3%, 17.8% and 23.8% porosity. Figure 10 shows a sample stress–strain response for the case of 17.8% lithophysal porosity, or the approximate average value obtained from panel maps in the cross-drift. The simulated stress–strain responses for tensile testing and compression at a number of confining pressures are shown. Adjacent to each of the stress-strain curves is a figure of the sample in the failed state. The addition of void volume results in failure due to fracturing between the voids in a fashion similar to that demonstrated previously for the PFC modeling. The general behavior is typical for brittle rock materials—increasing strength and conversion of the failure mode from axial splitting to shear failure as the confining pressure increases. The material response is elastic-brittle at low confinement and elastic-plastic at higher confining levels.

4.3. Establishing Bounding Ranges for Rock-Mass Properties

The calibrated PFC program is used as an extrapolation tool to examine the impact of lithophysae size, shape, porosity and distribution on mechanical properties of the rock mass. Parametric studies have been conducted with simple (e.g., circular) shapes of lithophysae, as well as actual complex shapes and distributions digitized from cross-drift panel maps. The results of these studies (shown in Figure 9) are used as a guide to understand the variability of mechanical properties for a given level of lithophysal porosity. Figure 11 shows the large-core laboratory mechanical-test data, plotted with the results of the PFC modeling studies that assume realistic lithophysae shapes and distributions from panel maps. As seen in this plot, approximate bounding estimates of the unconfined compressive strength and Young's modulus have been drawn for the range of saturated and unsaturated laboratory data as well as the PFC extrapolations of lithophysal shape and porosity variability. The linear fit to the 290-mm core data, which is used as a base-case measure of the mechanical properties for room dry conditions, is shown as is the mean of the two bounding curves. The plots are dashed for those points that fall outside the range of the data. The laboratory data show that the saturated environmental conditions form a lower bound to the property ranges and that the PFC extrapolations of shape variability fall within the bounding curves.

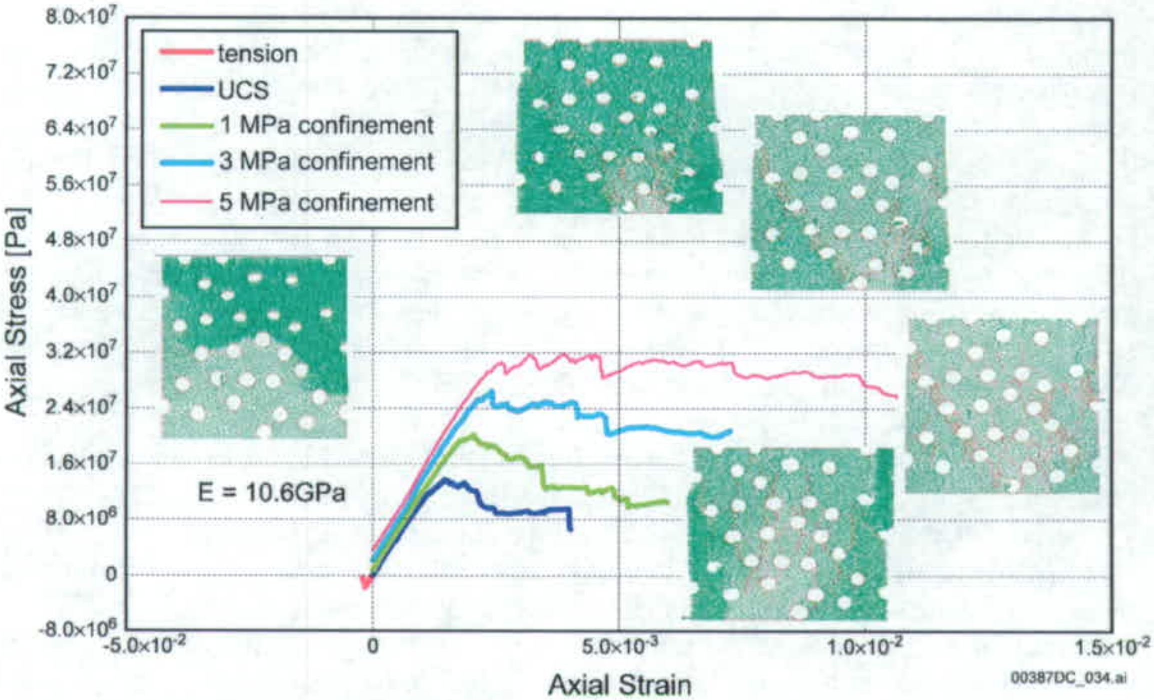

NOTES: "Samples" showed a failed state for a particular confining pressure: counterclockwise from the left are direct tension, unconfined, and 1-MPa, 3-Mpa, and 5-MPa confining stress. Circular voids are distributed randomly throughout the sample.

Figure 10. Stress-Strain Response and Failure Mechanisms for Lithophysal Porosity of 17.8%

The PFC models estimate the impact of lithophysae shape and distribution on the strength of small (meter-scale) samples of rock. When the lithophysae size is roughly proportional to the sample size (the case in some of the PFC modeling), it is possible to produce strengths that are unrealistically low. A number of drift-scale stability models of the cross-drift were run using the UDEC discontinuum program for the entire range of strengths shown in Figure 11. It was found that unconfined compression strengths with values below about 10 MPa predict that significant sidewall spalling of the cross-drift would be observed in the lithophysal rock. However, these drifts are stable and in good structural condition despite the fact that only light bolting (none in the sidewalls of most of the drift) is used. Therefore, a lower-bound strength cutoff of 10-MPa is assumed. It is noted that no laboratory testing has showed strengths below about 10 MPa, even for fully saturated samples.

The impact of variability of the mechanical properties of the lithophysal rock on drift stability is accounted for by conducting parametric stability analyses that cover the entire range of probable rock-mass properties (i.e., from the highest-porosity and poorest-quality to the lowest-porosity and highest-quality lithophysal rocks).

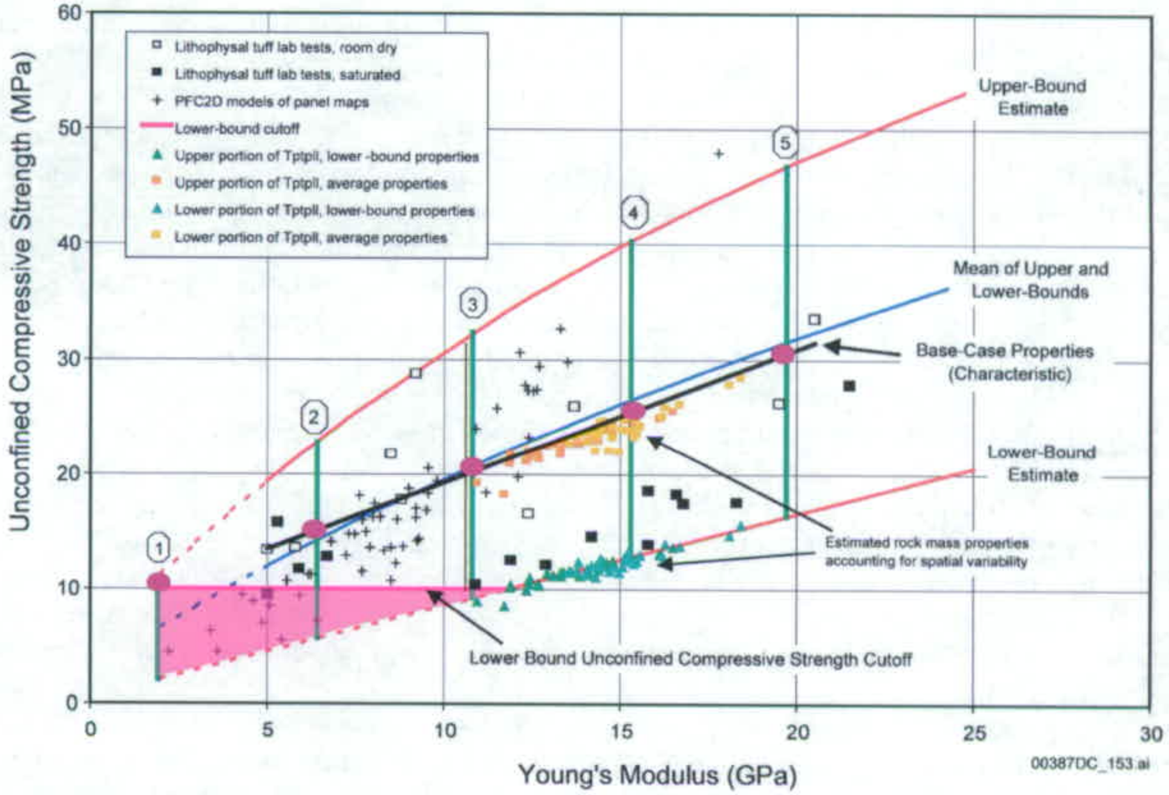

NOTES: Base-case average properties defined for each category are the mean and the upper and lower bounds of each range. Category 1 is highest-porosity, lowest-quality rock; category 5 is lowest-porosity, highest-quality rock. Results of rock-mass strength estimates from spatial variability studies are shown and assume mean and lower-bound properties.

Figure 11. Lithophysal Rock Strength and Modulus Range Divided into Five Rock Strength Categories Covering the Large-Core Laboratory Testing and PFC Extrapolation Studies

5. Dynamic and Thermal-mechanical Analyses

5.1. Drift-Scale Modeling Method for Lithophysal Rock Using the UDEC Program

Although the PFC and UDEC programs have been shown to provide reasonable agreement to large-scale laboratory compression testing of lithophysal rock, it is not practical to attempt to model a full tunnel-scale problem with explicitly represented lithophysal cavities. The model would be excessively large, with correspondingly large run times. Furthermore, it is not necessary to attempt to model individual lithophysae as long as the overall mechanical response of the material model of the rock mass is consistent with material behavior and properties determined in the previous section.

In the models used for predicting rockfall for different loading conditions, the rock mass is represented as an assembly of polygonal, elastic blocks (as shown in Figure 12) that are bonded together across their boundaries to form a coherent solid. The goal is to provide a model of a rock mass in which the overall mechanical behavior of the model is consistent with the material model developed for the lithophysal rock, yet allows internal fracturing to form and blocks to loosen and detach as the evolving stress state dictates. In other words, the fractures are "invisible" to the model until yielding begins.

Because the block boundaries can fail in tension and shear, they act as "potential fracture" locations should the stresses approach the fracture strength. It is important that the block assemblage contain blocks that are sufficiently small that the model does not dictate where and how fractures can form and propagate. The entire tunnel domain is discretized into small blocks (using Voronoi tessellations, Itasca Consulting Group 2002) that roughly are consistent with the maximum block size expected from rock-mass fracture spacings. The joints between blocks are considered to behave mechanically according to a linearly elastic–perfectly brittle plastic model. The elastic behavior of the joints is controlled by constant normal and shear stiffnesses. The possible failure modes of the rock mass are controlled by the strength of the joints. The joints can sustain a finite tensile stress, whereas a Coulomb slip condition governs the onset of slip, as a function of joint cohesion and friction angle. If a potential fracture develops, either in tension or shear, tensile strength and cohesion are set to zero, whereas the friction angle is set to the residual value. This model allows for the formation of fractures between blocks, separation and instability (under action of gravity) of portions of the rock mass around a drift.

The blocks used in the UDEC model do not represent the actual internal structure of the lithophysal rock mass. They are a tool in the numerical model used to simulate the damage and fracturing of the rock mass (i.e., the potential fractures in this model do not correspond to actual features). Therefore, it is not possible to obtain directly the joint properties in the UDEC model from results of laboratory or field testing on samples of lithophysal rock. To ensure that an assembly of Voronoi blocks behaves as a lithophysal rock mass, it must be calibrated. Calibration is performed by numerical simulation of tests (e.g., unconfined compressive strength tests) that actually are conducted in the laboratory or the field and for which the test results are available. (The synthetic samples are "cored" from the model of drift stability, as illustrated in Figure 12.) During these tests, the Coulomb strength parameters (joint cohesion and tensile strength) and the joint stiffness values are fitted to achieve the measured modulus and compressive strength for each rock mass category. As seen in Figure 13, the calibration involves generating stress-strain curves for the equivalent material. Validation of the approach and the model was accomplished by analyzing the stability conditions of the existing excavations under *in situ* stresses as well as by analyzing spalling observed during thermal overdrive testing in the nonlithophysal rock in the drift-scale heater test (Bechtel SAIC Company 2004).

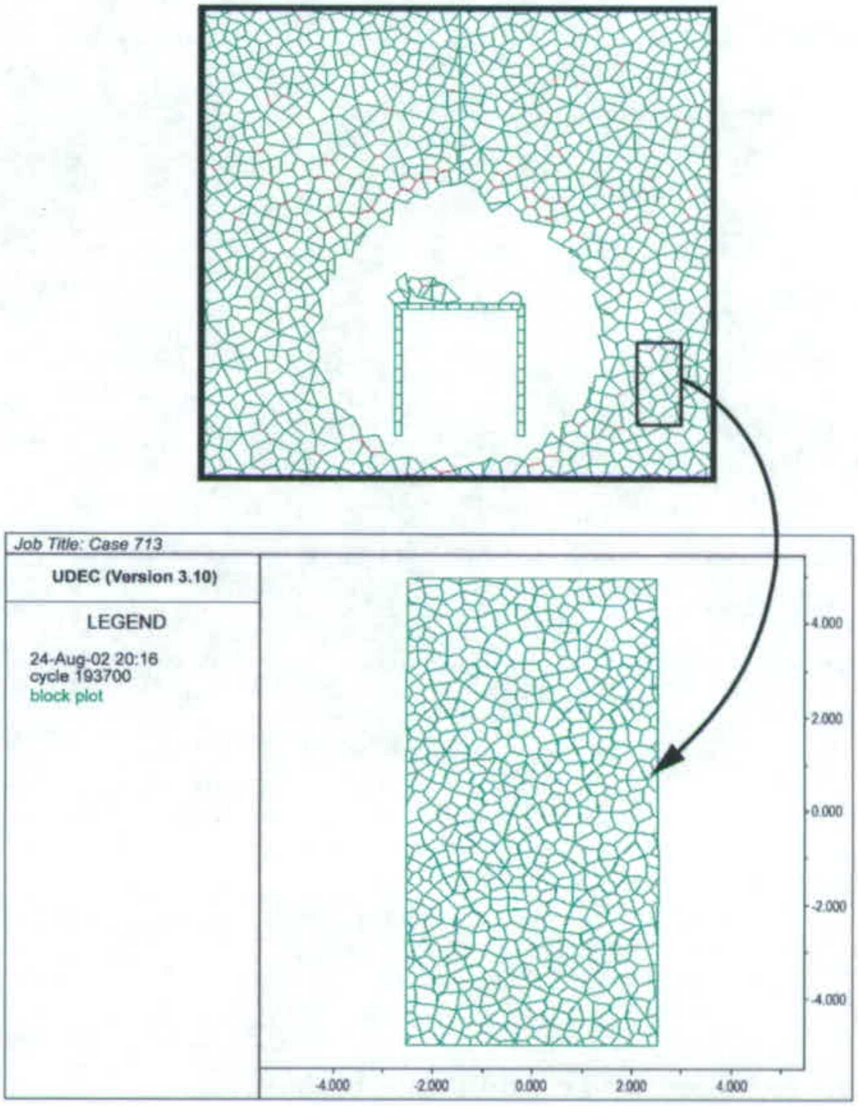

NOTES: Blocks are bonded at their contacts with a cohesion and tensile strength. When these break, the contacts become purely frictional. The specimen is "sampled" from equivalent rock mass representing the Tptpll.

Figure 12. UDEC Lithophysal Rock Specimen Composed of Many Irregular Blocks with Roughly Equidimensional Side Lengths

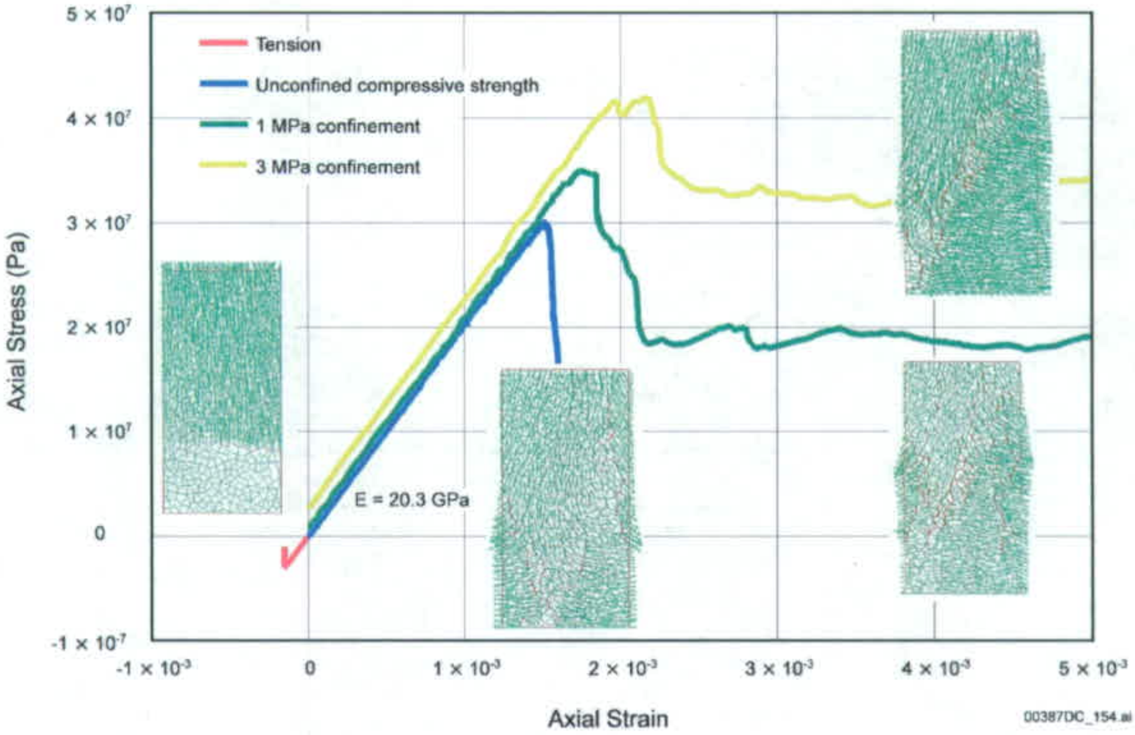

NOTES: Joint stiffness, shear and tensile strengths are calibrated to reproduce laboratory values of Young's modulus and unconfined compressive strength. Samples show fracturing and failure modes in tension and unconfined and confined compression.

Figure 13. Example of the Calibration of the UDEC Discontinuum Block Model to Laboratory Testing Results in Unconfined and Confined Compression and Tension, Strength Category 5

5.2. Seismic Consideration in Lithophysal Rock

Drift stability was analyzed for two preclosure (5×10^{-4} and 1×10^{-4} annual exceedance probabilities) and two postclosure (1×10^{-5} and 1×10^{-6} annual exceedance probabilities) ground motion data sets. Cases for lower annual probabilities of exceedance were not examined since complete drift collapse occurs for the 1×10^{-6} case. Description of the site-specific ground motions is provided in Part I, Section 5.1. It was assumed that complete collapse would occur for these lower probabilities cases as well. One ground motion, (consisting of the three component motions) was supplied for each of the preclosure cases, whereas 15 sets of ground motion data were supplied for the postclosure cases. For each of these ground motion data, the response for the range of rock mass properties categories was investigated.

An *in situ* (before excavation) stress state, defined by 7-MPa vertical and 3.5-MPa horizontal stresses, is used throughout the simulations, which is consistent with the 3DEC modeling discussed previously. The equilibrium state of the model after excavation of a drift represents the initial condition for the dynamic analysis. This equilibrium state is achieved by performing a quasistatic simulation whose geometry, static boundary, and initial conditions are illustrated in Figure 14.

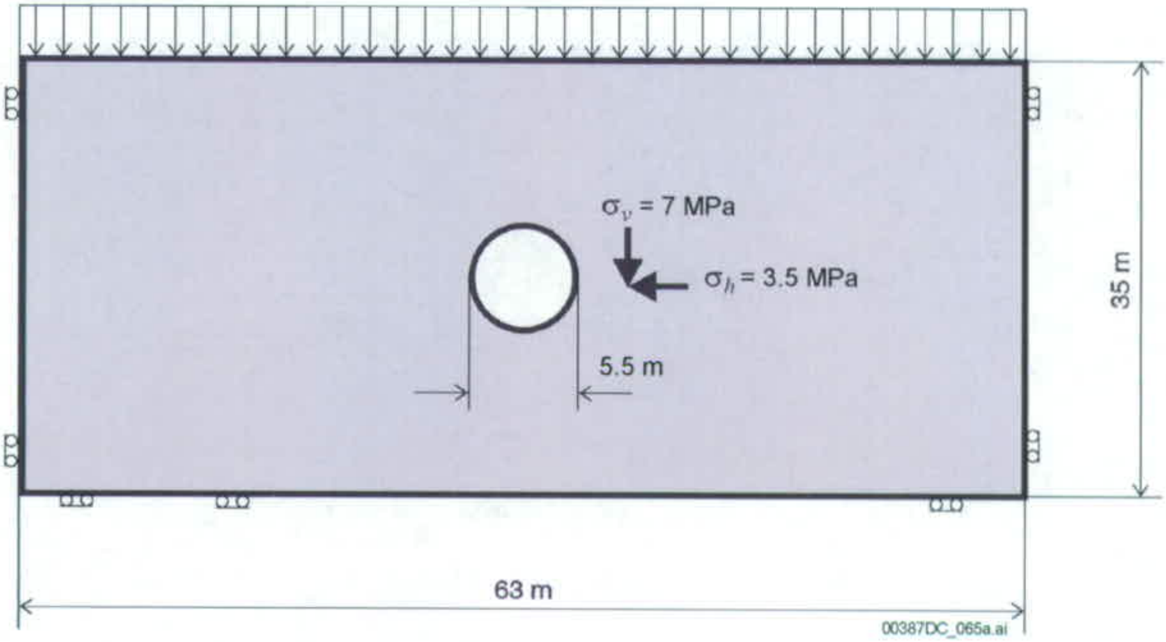

Figure 14. UDEC Model, Initial and Boundary Conditions for Initial Static Simulation

The boundary conditions used in the dynamic analysis are illustrated in Figure 15. Viscous boundaries were used on all model outside boundaries. These boundaries prevent reflection of outgoing seismic waves back into the model. Viscous boundaries were combined with free-field boundaries on the vertical outside boundaries that prevent distortion of vertically propagating plane waves along the boundaries. Dynamic loading was applied at the bottom of the model, as propagating vertically upwards.

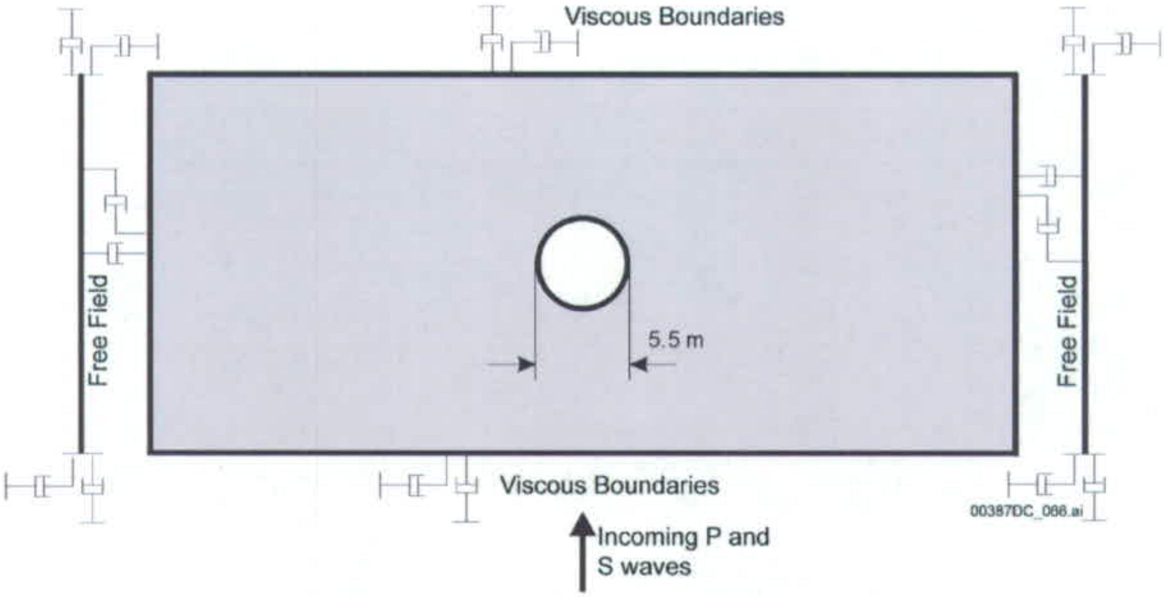

Figure 15. UDEC Model Boundary Conditions for Dynamic Simulation

5.2.1. Analysis Results for the Preclosure Ground Motions

The preclosure ground motions, defined here as annual probabilities of exceedance 1×10^{-4} or greater, were conservatively examined for unsupported tunnels. The analyses indicate that ground motion with probabilities of an annual occurrence of 5×10^{-4} and 1×10^{-4} will not induce any rockfall for rock quality categories 2 through 5. As discussed in Section 4.1, the estimated mean rock mass condition is category 3, with about 90% of the Tptpll having category 3 or greater properties. A relatively small amount of rockfall from the drift walls is expected, even for the lowest quality (less than 10% of all lithophysal rock) category 1. In reality, no rockfall would occur in preclosure since the emplacement drifts are fully supported with rockbolts and surface steel sheeting. Stress monitoring locations within the rock mass surrounding the tunnel show that dynamic stress changes induced by this ground motion are small, and the rock mass remains well within the elastic range. The observed rockfall in the category 1 case is simply the small springline zone of yielded rock from *in situ* stresses being shaken down. The conclusion is that only minor sidewall sloughing would be expected from this ground motion, and only in the poorest quality rock. Light bolting and surface support would easily contain this material.

5.2.2. Analysis Results for the Postclosure Ground Motions with 1×10^{-5} Annual Exceedance Probability

Fifteen sets of ground motion time histories were applied to unsupported base case rock mass strength categories 1, 3, and 5 to provide a crossection of response across the entire range of rock qualities. The level of damage induced by the ground motion is quantified here by the area (volume) of the rock that yields and is detached from the surrounding rock mass and falls into the tunnel. Figures 16 to 18 show representative examples of the mechanism and level of damage induced for rock strength categories 1, 3, and 5 for ground motion 12 (1.04 m/s peak ground velocity in H1), 4 (1.52 m/s peak ground velocity in V), and 7 (3.33 m/s peak ground velocity in V).

The drift damage levels are plotted for each rock mass strength category as a function of peak ground velocity in Figure 19. The peak ground velocity is the highest value among the three components of H1, H2, and V. The analyses show that the damage is related to the magnitude of peak ground velocity, with significant variability at large peak ground velocity. Approximate linear upper and lower bounds are shown for each rock strength category, with a damage band shown that covers the range of variability. The variability in the response is a function of the ground motion, not the rock properties, since constant modulus and strength are assumed for a given category. This variability at large peak ground velocity can be explained by examining the damage as a function of the total energy in the waveform. A Fast Fourier Transform was used to perform an integration of each of the 15 velocity time histories (in terms of the velocity squared). The result of this integration is a spectral power density number that is proportional to the total kinetic energy (kinetic energy = $\frac{1}{2}(mv^2)$) of the time history. The damage as a function of the velocity power spectral density for the ground motion component (either H1 or V, whichever has the maximum value of peak ground velocity) for each of the 45 analyses is plotted in Figure 20. This plot shows that the damage is linearly related to the kinetic energy associated with the velocity time history. Therefore, although the peak ground velocity is, in general, related to drift damage, the variability in that correlation is related to the total kinetic energy in the time history.

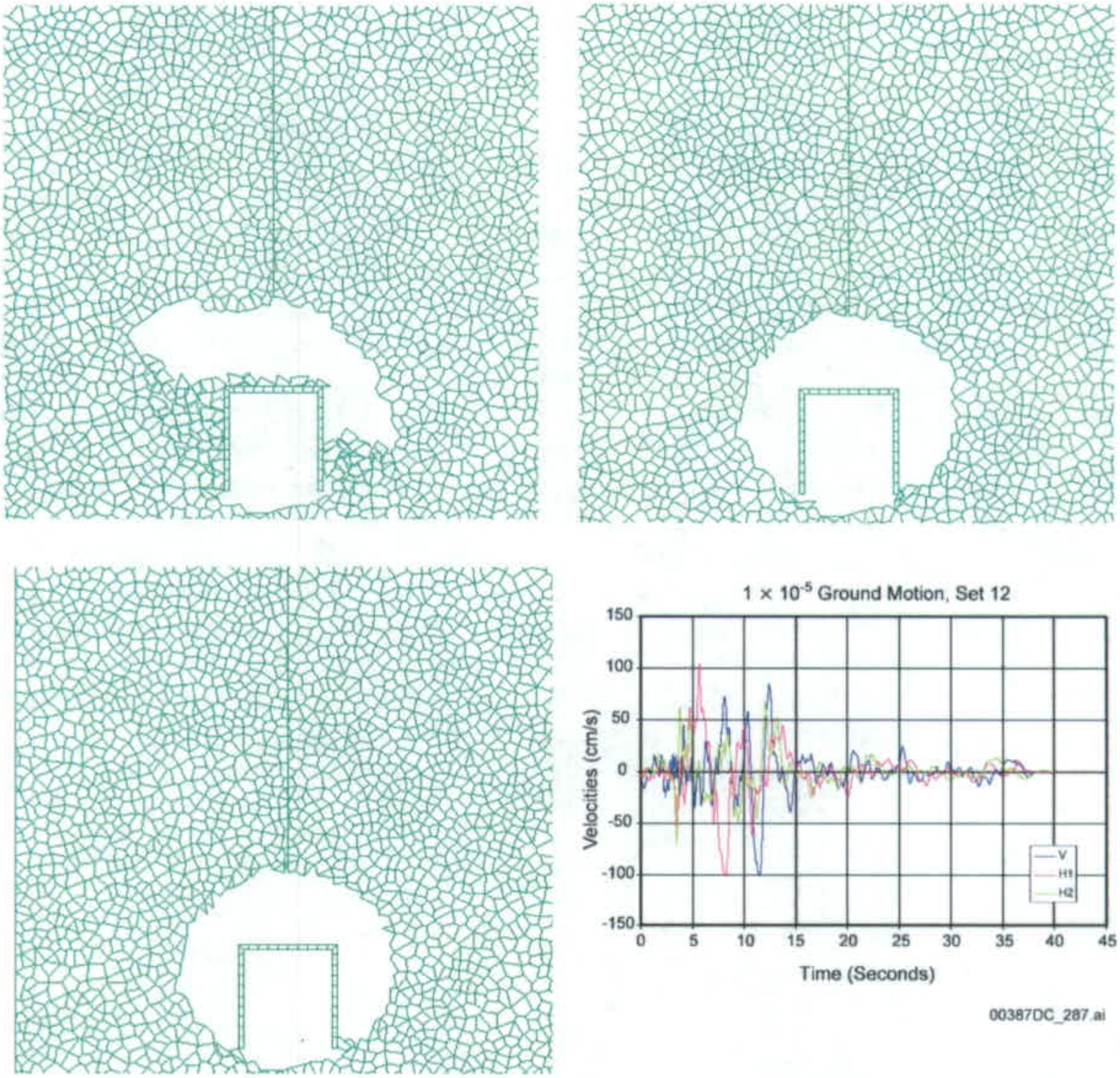

NOTES: (Clockwise from upper left) Rock Strength Category 1 (5.6 m^2/m drift length), Category 3 (0.02 m^2/m), Ground Motion History 12, PGV=104 cm/s, and Category 5 (0.1 m^2/m).

Figure 16. Example of Comparison of Damage Levels for Lower End of PGV (104 cm/s) for 1×10^{-5} Annual Exceedance Level

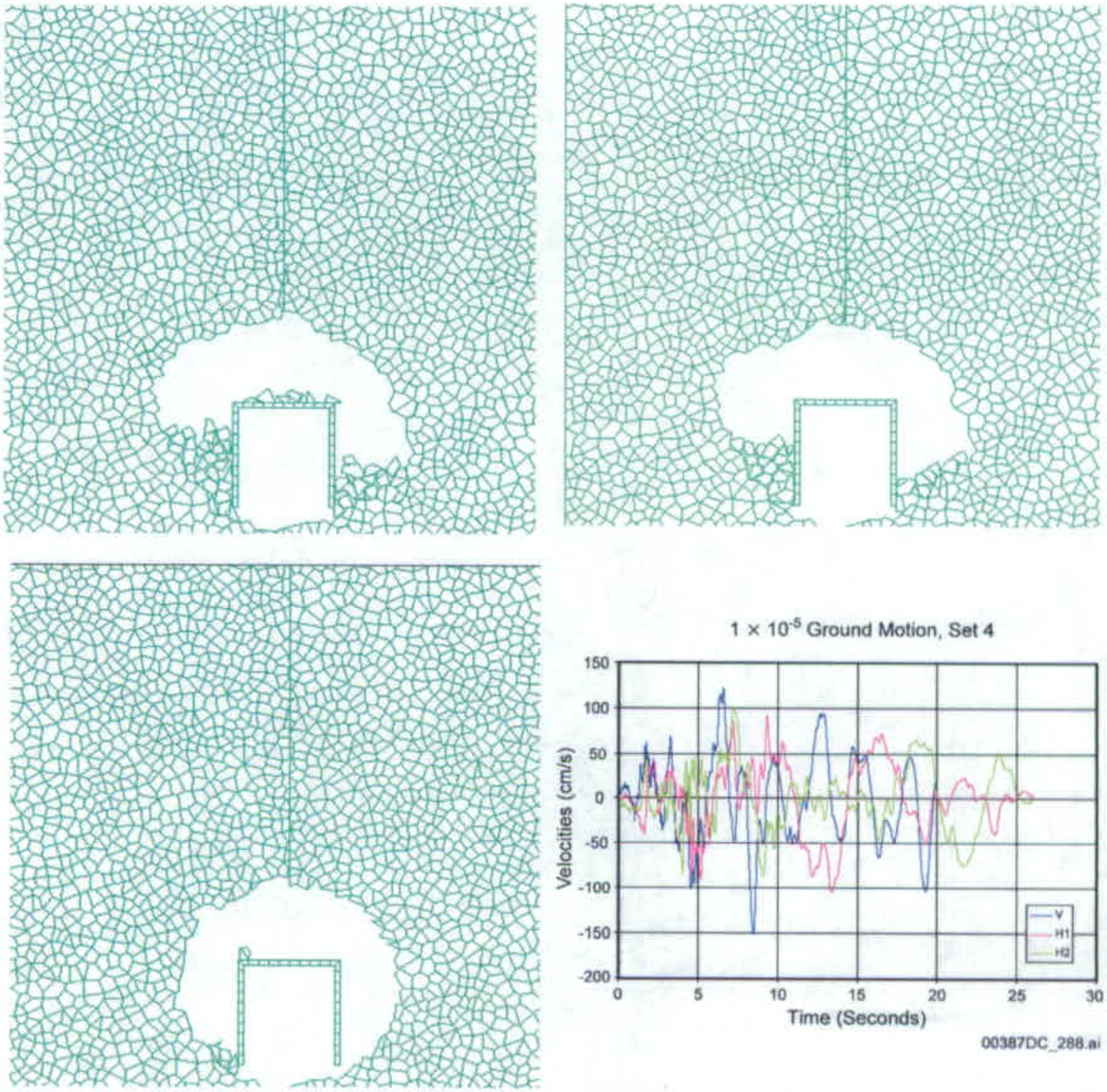

NOTES: (Clockwise from upper left) Rock Strength Category 1 (3.3 m^2/m drift length), Category 3 (2.2 m^2/m), Ground Motion History 4, PGV=152 cm/sec, and Category 5 (0.3 m^2/m).

Figure 17. Example of Comparison of Damage Levels for PGV of 152 cm/sec for 1×10^{-5} Annual Exceedance Level

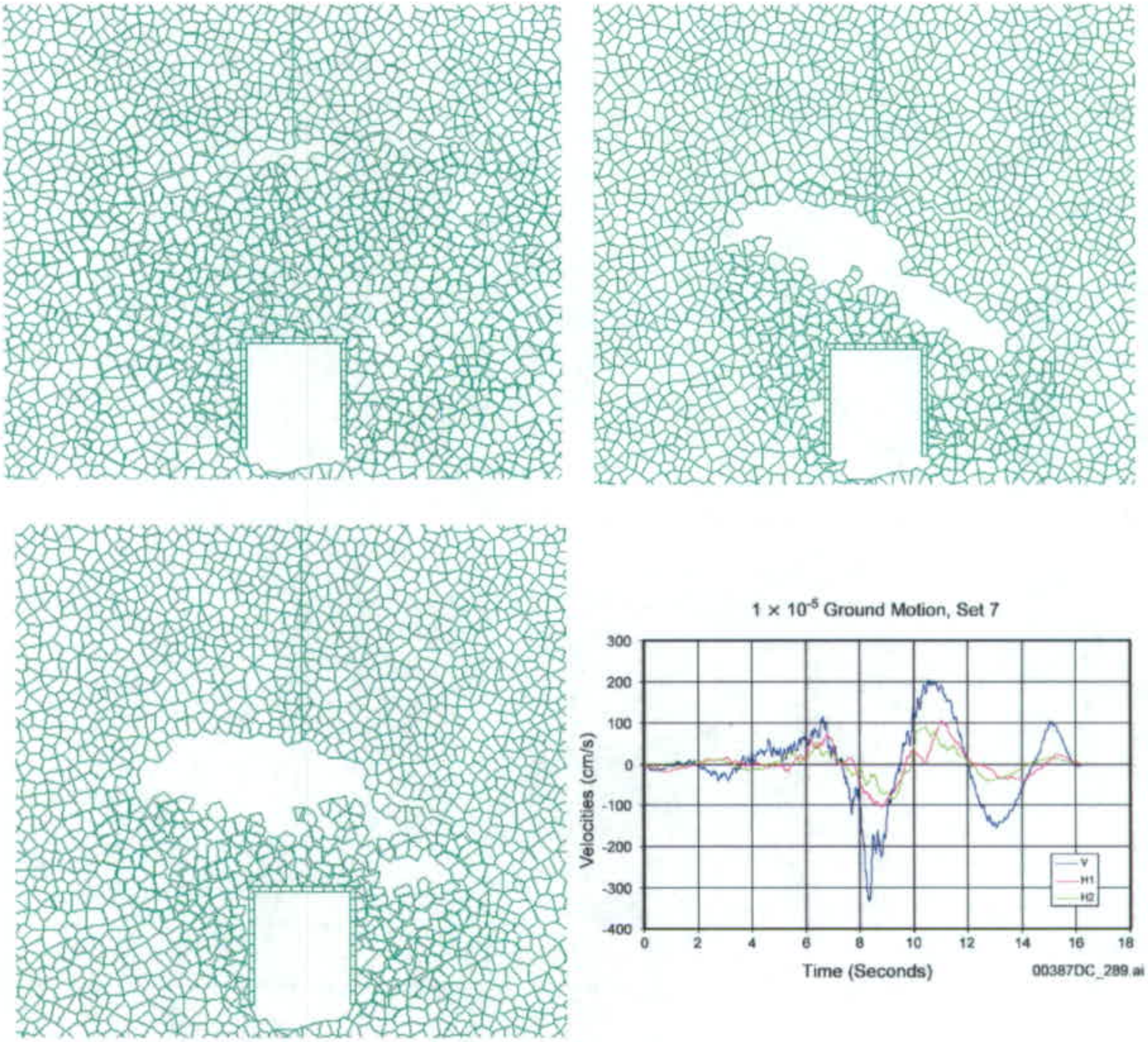

NOTES: (Clockwise from upper left) Rock Strength Category 1 (40.6 m^2/m drift length), Category 5 (19.7 m^2/m), Ground Motion History 7, PGV=333 cm/s, and Category 3 (15.4 m^2/m).

Figure 18. Example of Comparison of Damage Levels for Upper End of PGV (333 cm/s) for 1×10^{-5} Annual Exceedance Level

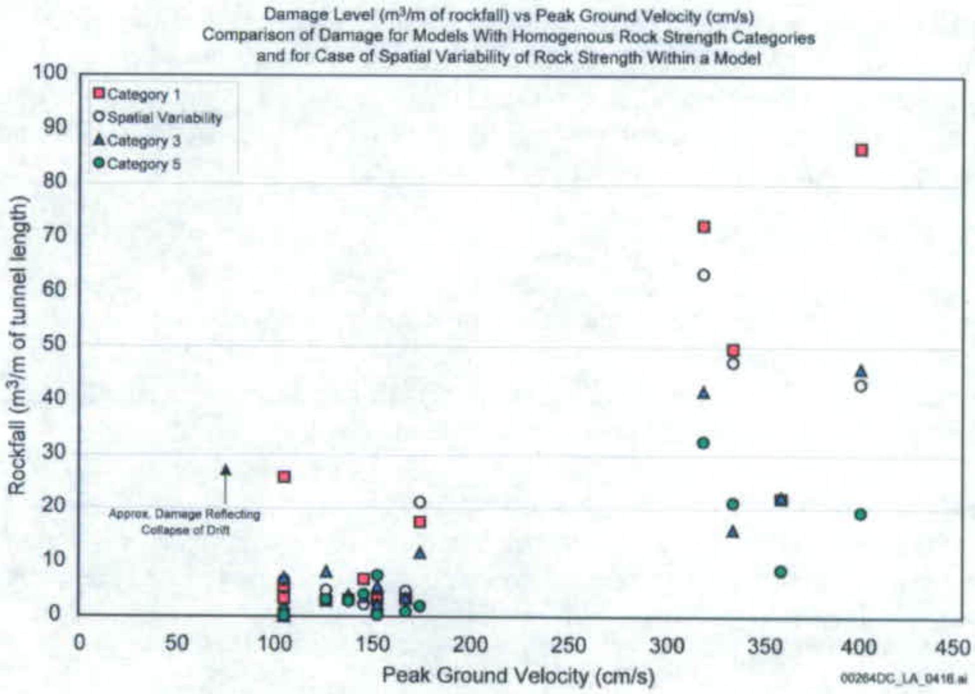

NOTES: Damage levels for the 15 ground motions are given. Results for spatially variable lithophysal porosity are also given for comparison.

Figure 19. Estimate 1×10^{-5} Annual Probability of Exceedance Damage Level, Expressed as m^2/m of Emplacement Drift Length for Rock Strength Categories 1, 3, and 5 for the 15 Ground Motion Time Histories

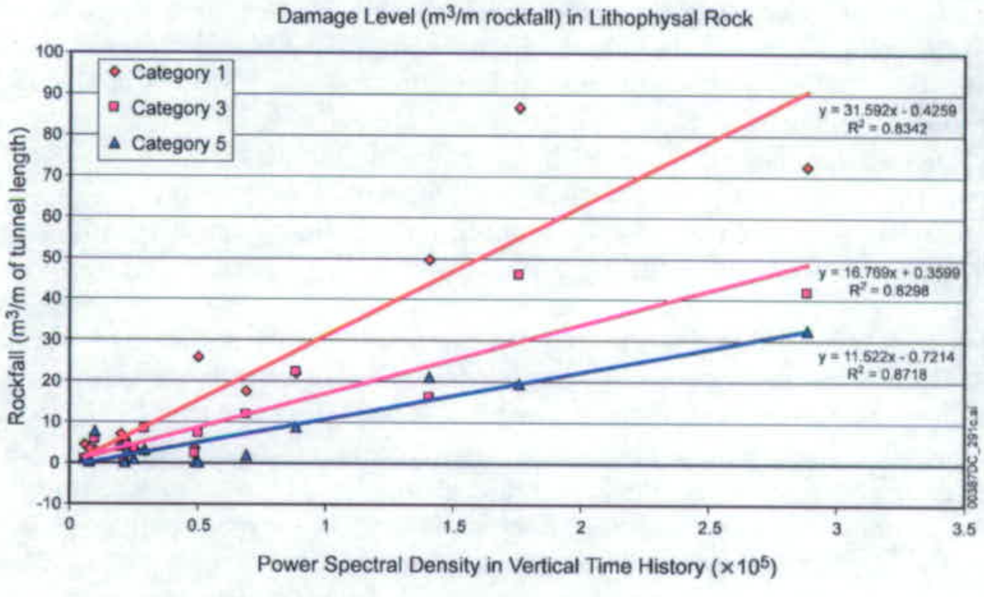

NOTE: The power spectral density is obtained by integrating the square of the velocity time history, producing a value proportional to the kinetic energy.

Figure 20. Rockfall Damage as a Function of the Energy Associated With the Vertical Velocity Time History

The drift damage mechanism consists primarily of stress-induced failure of the rock mass resulting from the stress change associated with the velocity time history. The *in situ* stress field has major vertical and minor horizontal stress components. The vertical compression or horizontal shear wave essentially results in a free field dynamic stress increase equivalent to (Itasca Consulting Group 2002):

$$\sigma_{n,s} = \rho C_{p,s} V_{n,s}$$

where: $\sigma_{n,s}$ = dynamic induced normal (*n*) or shear (*s*) stress component
ρ = rock density
$C_{p,s}$ = speed of p-wave (*p*) or s-wave (*s*) propagation in rock medium
$V_{n,s}$ = peak normal (*n*) or shear (*s*) ground velocity

These dynamic components are superimposed on the existing *in situ* stress field to cause additional stressing or relaxation of the rock mass surrounding the drift. The end result of this superposition is that the stress tensor changes, both in magnitude and orientation of the principal stresses, as the ground velocities oscillate over the duration of the strong ground motion. Superposition of *in situ* and dynamic stresses can cause tensile or shear failure of rock mass, resulting in development of an elliptic shape of the opening as the rock mass yields and rockfall occurs and falls along the sides of the drip shield. Shear failure is most likely to start at the springline, which is the location of the largest stresses under *in situ* stress conditions. The extent of shear failure and rockfall around the circumference of the tunnel, up and down from the springline, is due to both the general ratio of rock mass strength to stress, but also to the ratio of the vertical to horizontal peak ground velocity. The greater the horizontal component, the greater the rotation of the stress tensor, which results in greater inclination of the major principal stress. Generally, this shear failure mechanism occurs with the arrival of the peak ground velocities. Compressive stresses also appear responsible for some cases in which roof slabbing is observed where the rock mass strength and stiffness are larger (i.e., category 5). A second failure mechanism observed includes tensile failure of the rock mass resulting from the reversal of the ground motion and inducement of dynamic tensile straining in the rock mass (i.e., when seismically induced tensile stress exceeds *in situ* compressive stress and tensile strength, combined).

In general, it appears that the rock mass failure and, thus, rockfall occurs simultaneously with the arrival of velocity peaks in the time histories. In a similar fashion, many authors recognize peak ground velocity as the primary contributing factor to dynamic rock mass failure in mine tunnels, slopes and dams (e.g., Newmark 1965). Currently, the shear or tensile failure mechanism results in a predicted creation of blocks resulting from fracture of the rock mass along the ubiquitous fracture network of the material.

Although the damage levels appear to correlate somewhat better to the energy content of the time history, correlation to peak ground velocity provides a simpler method for interpretation of the results. An approximate relationship of damage level to peak ground velocity in terms of m^3/m of drift length and physical interpretation can be roughly approximated as follows:

- Damage level below 5 m^3/m results in minor damage to rock particles filling the invert along the sides of the drip shield–a peak ground velocity below about 1.5 m/s (Figure 16).
- Damage level from 5 m^3/m to 15 m^3/m results in rock particles covering the sides of the drip shield approximately to the height of the drip shield and may cover the top of the drip shield – this corresponds to peak ground velocity values of approximately 1.5 m/s to 2 m/s (Figure 17).
- Damage level above 15 m^3/m causes complete collapse of the tunnel, this corresponds to peak ground velocity values of approximately 2 m/s to 3 m/s (Figure 18).

5.2.3. Analysis Results for the Postclosure Ground Motions with 1×10^{-6} Annual Exceedance Probability

Ground motions with a probability of an annual occurrence of 1×10^{-6} cause complete collapse of the emplacement drifts irrespective of the rock mass category and ground motion case. The 1×10^{-6} annual probability of exceedance ground motion time histories are characterized by the peak ground velocity of the H1 component of 2.44 m/s. The analyses of the 1×10^{-5} annual probability of exceedance ground motion showed extensive damage for peak ground velocity in excess of approximately 2 m/s, and therefore, similar damage is expected for all of the 1×10^{-6} annual probability of exceedance ground motion cases. The rock mass failure mechanism, a combination of shear and tension failure, is similar to that described for the 1×10^{-5} annual probability of exceedance cases. As was discussed in the previous section, tunnel collapse occurs for peak ground velocity values in excess of approximately 2 m/s to 3 m/s.

5.3. Thermal Consideration in Lithophysal Rock

The UDEC model does not perform complete thermal-mechanical simulations. Instead, temperature fields calculated with the code NUFT are imported into UDEC (thermal calculation. Two cases of ventilation efficiency were considered: 90% and 70%. Stresses are calculated for each new temperature state based on the temperature increment (from the previous temperature state) and the coefficient of thermal expansion. For the considered cases, the same coefficient of thermal expansion as a function of temperature was used. To have gradual evolution of stresses during the simulated time, 45 temperature fields (corresponding to different times after waste emplacements) were imported from NUFT to UDEC. The entire analysis was conducted considering that rock mass strength does not degrade with time. Any observed damage and rockfall are consequences of the thermally induced stresses only. The three cases of thermal calculation were considered for the drift stability analysis in lithophysal rock mass:

- Case 1—Base case (average thermal properties and 90% ventilation efficiency)

- Case 2—Sensitivity calculation for thermal properties (thermal properties one standard deviation smaller than the average properties)
- Case 3—Sensitivity calculation for the heat removal ratio (average thermal properties and 70% ventilation efficiency).

The simulation was conducted for the five mechanical properties categories of the rock mass. It is observed that the amount of thermally induced rockfall is generally small. The temperature and stress fields for rock mass category 1 with the base case thermal properties and 90% ventilation efficiency are shown in Figure 21. The figure shows the model state after 80 years and 10,000 years of heating. There is no significant rockfall or damage induced by heating. Conditions are similar for other rock mass categories. Elastic stress paths during 10,000 years of temperature variation were constructed for points in the wall and roof for evaluation. The elastic stress paths confirm the results of the UDEC lithophysal rockfall model. The rockfall simulations using temperatures from cases 2 and 3 of the thermal calculation do not show any increase in rockfall compared to the base case.

Additional analyses were done to assess the effect of changing thermal stress in the rock mass around the repository after waste emplacement as an initial condition for seismic ground shaking. Using a similar approach as for the nonlithophysal rock, stress paths during the regulatory period of 10,000 years were recorded at a number of locations around the drift. Temperatures from the thermal calculations for the base case and the sensitivity calculation for the heat removal ratio (case 3) were considered. The critical state was qualitatively determined from those paths, based on locations of stress states along that path relative to the yield surface. The stress state after 80 years of heating was selected as critical based on locations of stress states along that path relative to the yield surface. The critical state was used as an initial condition for the seismic analysis. Because the ground motion with 1×10^{-6} probability of annual exceedance results in complete drift collapse, it was not of particular interest to investigate the effect of that level of ground motion combined with thermally induced initial stresses. Instead, ground motions with 1×10^{-4} and 1×10^{-5} probability of annual exceedance were considered.

Seismic analysis after 80 years of heating for rock mass category 1 resulted in an increased rockfall compared to rockfall from the seismic shaking of the rock mass at an *in situ* stress state. Figure 22 presents the rockfall and fractures induced around a drift with 1×10^{-4} annual probability of exceedance ground motion. Very little rockfall is induced in rock mass category 5 in the case of 70% ventilation efficiency. For the cases with 1×10^{-5} annual probability of exceedance ground motions shaking, the results also show increase of rockfall with thermal consideration.

The result of an increase in rockfall for lithophysal rock with thermal loading is in contradiction with the results of the same analysis for the nonlithophysal units. Thermal stresses in the case of nonlithophysal rock resulted in reduced rockfall. However, the mechanism of rockfall is completely different for these two cases. In the case of the nonlithophysal rock mass, rockfall is due to sliding of blocks along the preexisting joints, and an increase in the initial stress increases confinement on the joints, thereby increasing their resistance to sliding. In the case of the lithophysal rock mass, ground motion with 1×10^{-4} probability of annual exceedance causes rockfall by shaking down already damaged rock mass around the drift. Therefore, the heating induces additional damage (compared to damage caused by drift excavation), which does not necessarily result in a rockfall under static loading conditions, but is shaken down by the 1×10^{-4} annual probability of exceedance ground motion.

(a) Temperatures

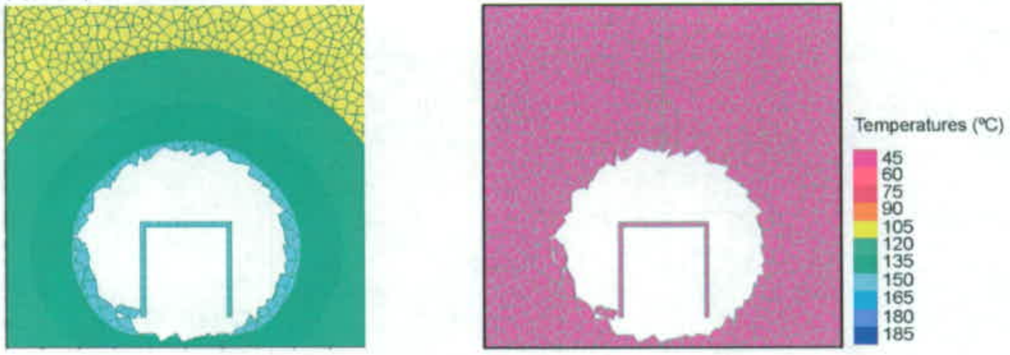

(b) Major principal stress

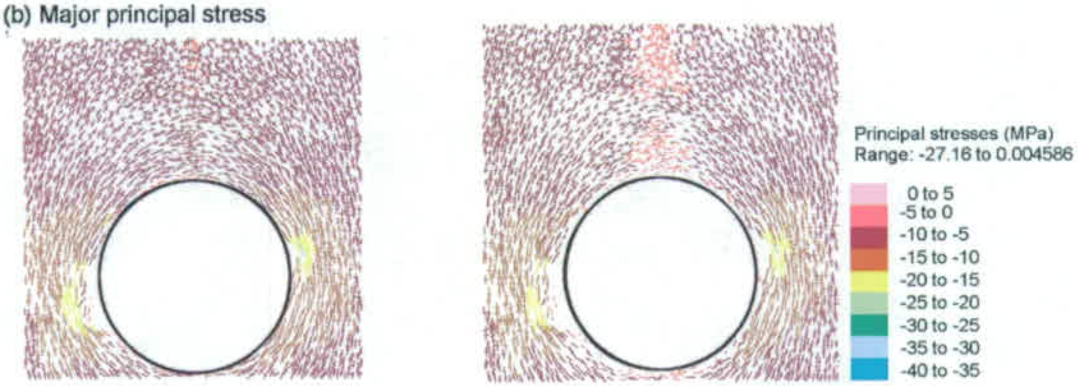

(c) Minor principal stress

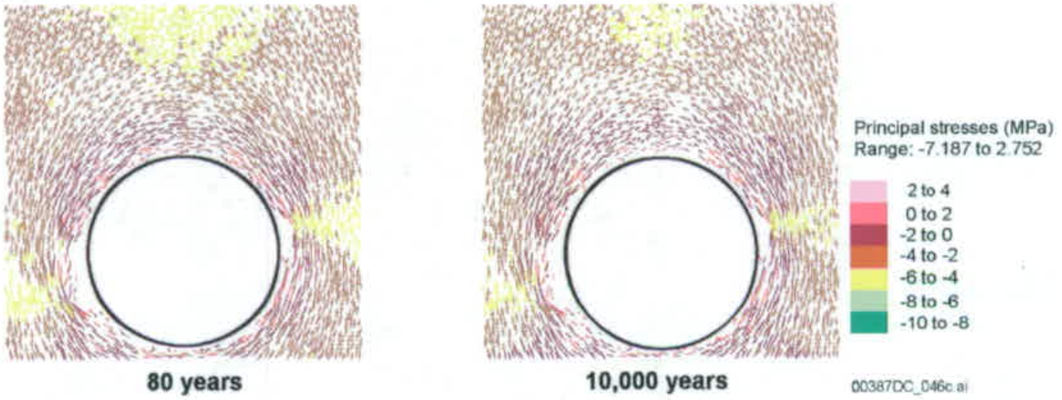

Figure 21. Thermally Induced Rockfall and Stresses After 80 Years and 10,000 Years of Heating in Rock Mass Category 1

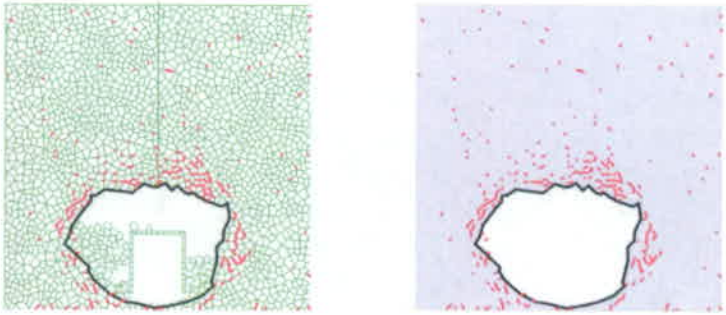

a) category 1

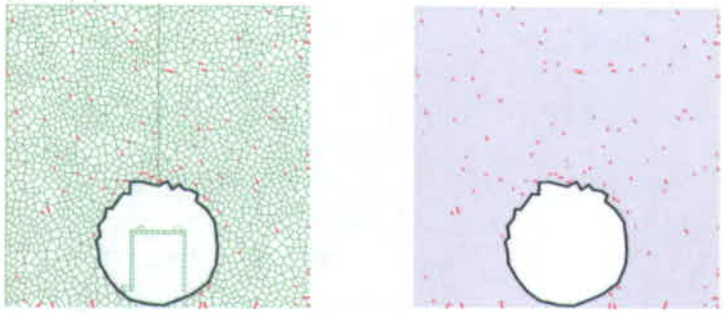

b) category 5

Figure 22. Rockfall and Fractures Induced Around a Drift by 1×10^{-4} annual probability of exceedance Ground Motion After the Peak Thermal Condition Occurring at 80 Years of Heating (30 Years after Closure) in Rock Quality Categories 1 and 5

5.4 Sensitivity of Mechanical Properties to Rockfall Prediction

5.4.1. Consideration of Lower Bound Strength

Consideration was given to the likely scatter of the strength within the same category as shown in Figure 11. Based on the assessment of rock mass properties, the lower bound strength ranges from 10 MPa to 16 MPa for the 5 categories compared with the range of 10 MPa to 30 MPa for the base case. In fact, the lower-bound strength of 10 MPa was assigned to categories 1 to 3. Because rockfall results with base case material properties indicate that minor spalling or no damage is predicted for the preclosure ground motion and drift collapse predicted for the 1×10^{-6} annual probability of exceedance ground motions, the sensitivity case only considers 1×10^{-5} annual probability of exceedance ground motions. Collapse of the drift is observed for most of the cases even with category 5 rocks. The results represent a very conservative estimate for the nominal case with the consideration that the surrounding rock is homogeneous and entirely biased to the low-strength end of the distribution within its category. Since the lower bound is estimated based on the saturated samples as shown in Figure 11, the results indicate that the saturated drift environment is likely to collapse when subject to 1×10^{-5} annual probability of exceedance ground motions. But for the nominal case with relatively dry conditions, spatial variation of rock around the drift is most realistic and should be considered.

5.4.2. Impact of Spatial Variability on Drift Stability

The impact of spatial variability of lithophysal porosity was assessed based on geologic mapping and stratiform geometry (Lin et al. 2005). A representative section of the Tptpll was extracted from the upper portion of the lithophysal porosity model. This model contains a wide range of lithophysal porosity averaging approximately 15%, but ranging from greater than 20% to less than 10%. The resulting UDEC lithophysal rockfall model showing spatially variable porosity is given in Figure 23.

Rock mass strength properties for categories 1 to 5 were assigned to regions within the model based on the lithophysal porosity levels, achieving spatial variability in strength and moduli. This model was subjected to the 15 1×10^{-5} annual probability of exceedance ground motions, and damage levels were determined. The results of the dynamic simulations, in terms of damage versus PGV, are shown in Figure 19. The damage levels are approximately within the range of that predicted for category 3 rock mass, as expected, because the mean lithophysal porosity of the model falls within the range of the category 3 levels. This analysis indicates that the use of homogenous rock properties that span the range of strength categories does span the range of expected response, including conservatively assessed damage for the low-strength categories.

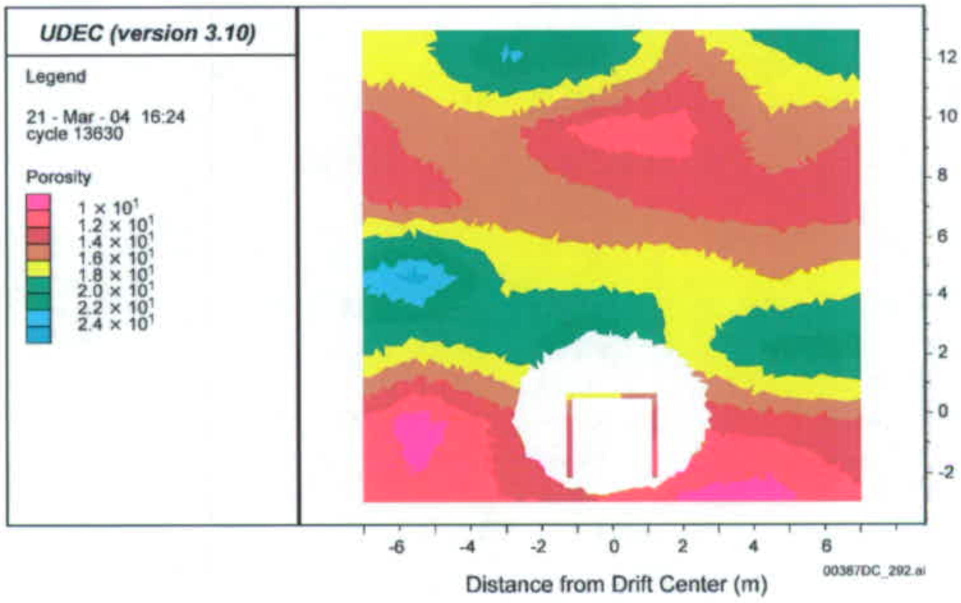

Figure 23. Contours of Lithophysal Porosity Contoured on the UDEC Spatial Variability Model

5.4.3. Time-Dependent Consideration

Underground and surface excavations, which are designed to be stable after excavation, degrade with time, and some eventually collapse completely. The primary reason for eventual yield and collapse is that a hard rock mass, exposed to humidity and temperature of the open atmosphere, may undergo strength decay with time when it is loaded to stress levels higher than about 50% to 60% of its short-term strength. A key mechanism of failure in brittle and crystalline rocks is development in the propagation of cracks parallel to the greatest principal stress direction. Extensive studies over the last 40 years have demonstrated that the critical parameters that control crack growth are stress, temperature, and the partial pressure of water at the crack tip. A crack grows due to the hydration and breaking of silicon–oxygen bonds at the tip of the crack. The rate at which the crack grows is controlled by the diffusion of water to the crack tip. This mechanism is commonly termed stress corrosion cracking. Stress corrosion is considered the primary mechanism causing strength degradation of hard rocks (Potyondy and Cundall 2001). Experimental data on single crystals of quartz, as well as in rocks, have validated the mechanism (e.g., Martin 1972; Kranz 1979). The rate of strength decay depends on, among other parameters, rock type (particularly the mineralogy and grain structure), stress state, relative humidity, and temperature.

In brittle rocks subjected to a constant stress, a crack will propagate in a time-dependent way. The diffusion of water to the crack tip controls the rate. Since the physical mechanism is hydration, there is a volume increase on the surface of the crack. Consequently, the propagation of water to the crack tip is controlled by diffusion along a crack surface where the aperture decreases and diffusivity decreases. This gives rise to a logarithmic time-dependent crack growth. The rate at which water diffuses to the crack tip decreases with time, the rate of crack growth slows down, and the observed deformation rate decreases. When the crack reaches a critical length, the rock fails. Furthermore, the lower the stress for a constant temperature, the longer the time to failure (Kranz 1980; Martin et al. 1997).

The PFC stress corrosion model by Potyondy and Cundall (2001), developed for similar time-dependent predictions for the Canadian waste disposal research program, has been used in this study to establish a rock mass damage–time relationship. The PFC stress corrosion model is first calibrated to reproduce the static fatigue response of Lac de Bonnet (LdB) granite and interpolated for nonlithophysal rock. The model is then used to investigate the impact of lithophysal porosity on the rate of time dependence, resulting in the generation of a set of curves of time-to-failure versus applied stress level for various levels of lithophysal porosity. Details for the PFC stress corrosion model and examination of impact of lithophysal voids are provided in Appendix A.

The rock mass damage-time relationship, developed from the PFC simulations, was used to generate estimates of drift degradation as a function of time for a range of rock mass strength categories. This relationship, illustrated in Figure 24, was embedded in the UDEC drift scale model to perform lithophysal rock stability calculations. It is assumed that the damage coefficients are related directly to the percentage loss of cohesion and tensile strength of these contacts; therefore, a damage coefficient of zero is no strength loss and a damage coefficient of 1 is 100% strength loss.

Throughout the 10,000 years after closure, the emplacement drifts and surrounding rock mass will be subject to a heating and cooling cycle. The time-dependent strength degradation will be a function of the *in situ* stress concentrations around the drifts as well as the transient, thermally induced stress changes. The addition of thermal stresses around the excavation will accelerate the process of strength degradation and potential drift instability. The results of numerical simulation of drift degradation as a result of these two stress states are shown in Figures 25 and 26 for categories 2 and 5 rock quality conditions. Initially, most of rockfall for category 2 rock comes from the walls, which are loaded to a near-yielding state for this rock mass category under *in situ* stress conditions alone. Strength degradation, combined with the increase in rock wall temperature, increases the tangential stress component in the walls, resulting in a small amount of rockfall from the walls within 5 years to 10 years after emplacement of the waste. The large increase in the temperature after the forced ventilation stops, and consequently in the immediate drift wall stresses, causes additional rockfall at the 80 years time frame when peak stress conditions are reached. Little additional rockfall occurs after that time as the rock mass slowly cools. Only small amounts of rock degradation are predicted for category 5 rock mass due to combined *in situ* and thermal stressing and time-dependent strength property change.

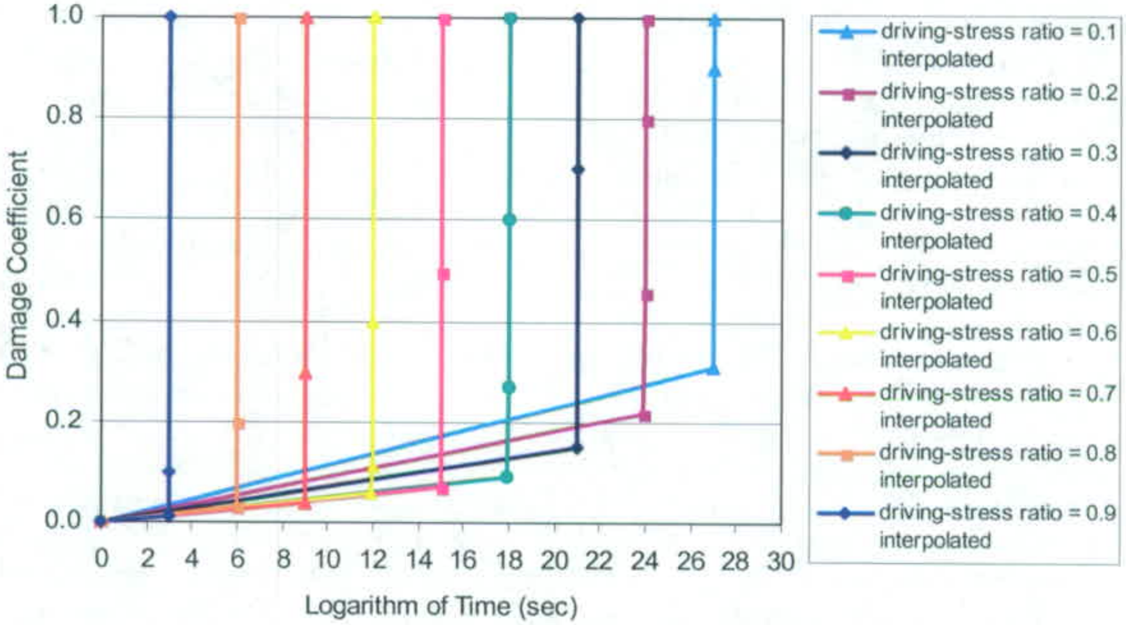

NOTE: Simplified curves are conservative in that complete damage (i.e., failure and loss of strength) is assumed to occur once time-to-failure is achieved.

Figure 24. Damage Curves Used as Input to the UDEC Tuff Best-Fit Analyses

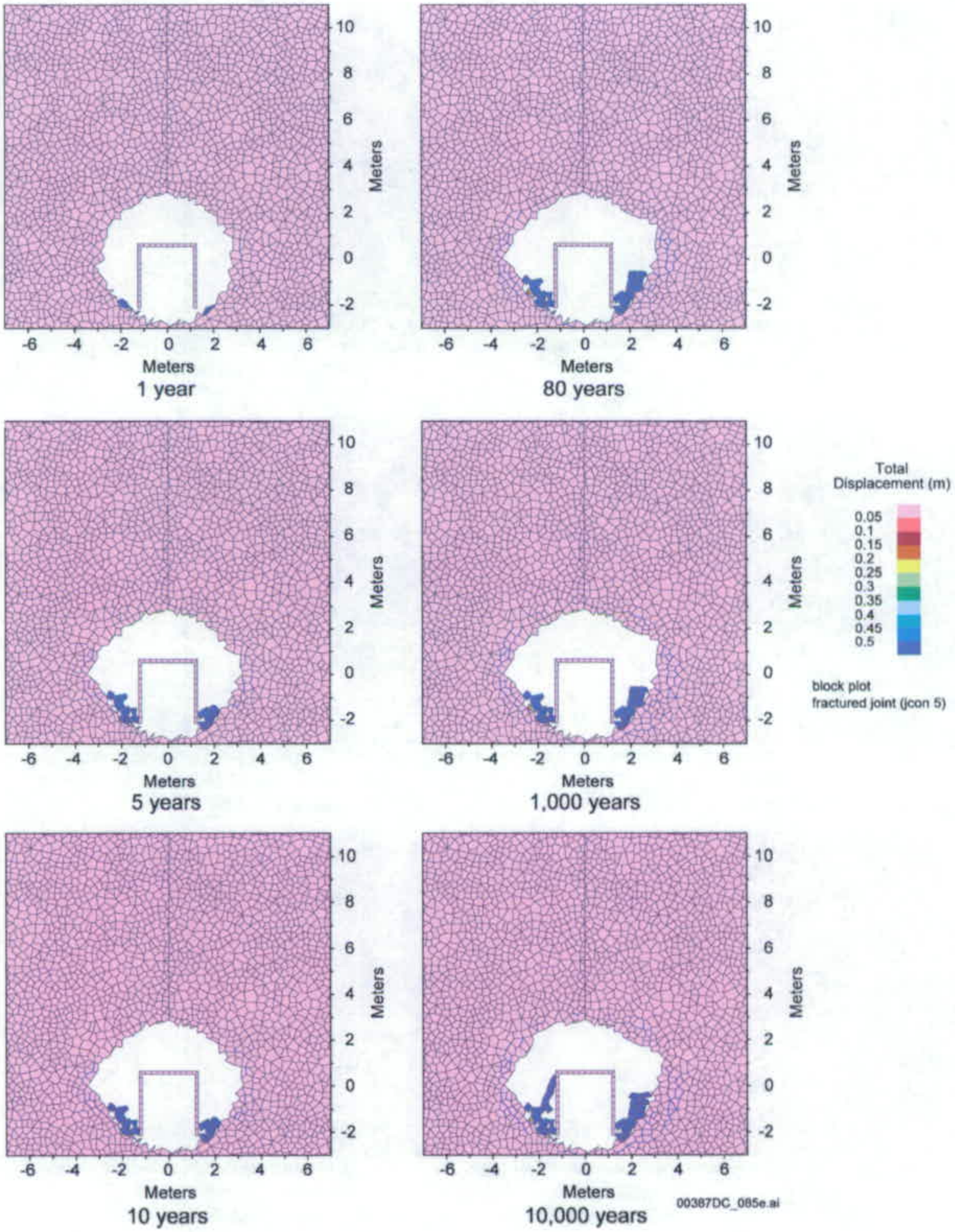

1 year

80 years

5 years

1,000 years

10 years

10,000 years

Figure 25. Predicted Evolution of Damage Due to Strength Degradation for Category 2–Tuff Best-Fit Static-Fatigue Curve, Combined *In Situ* and Thermal Stresses

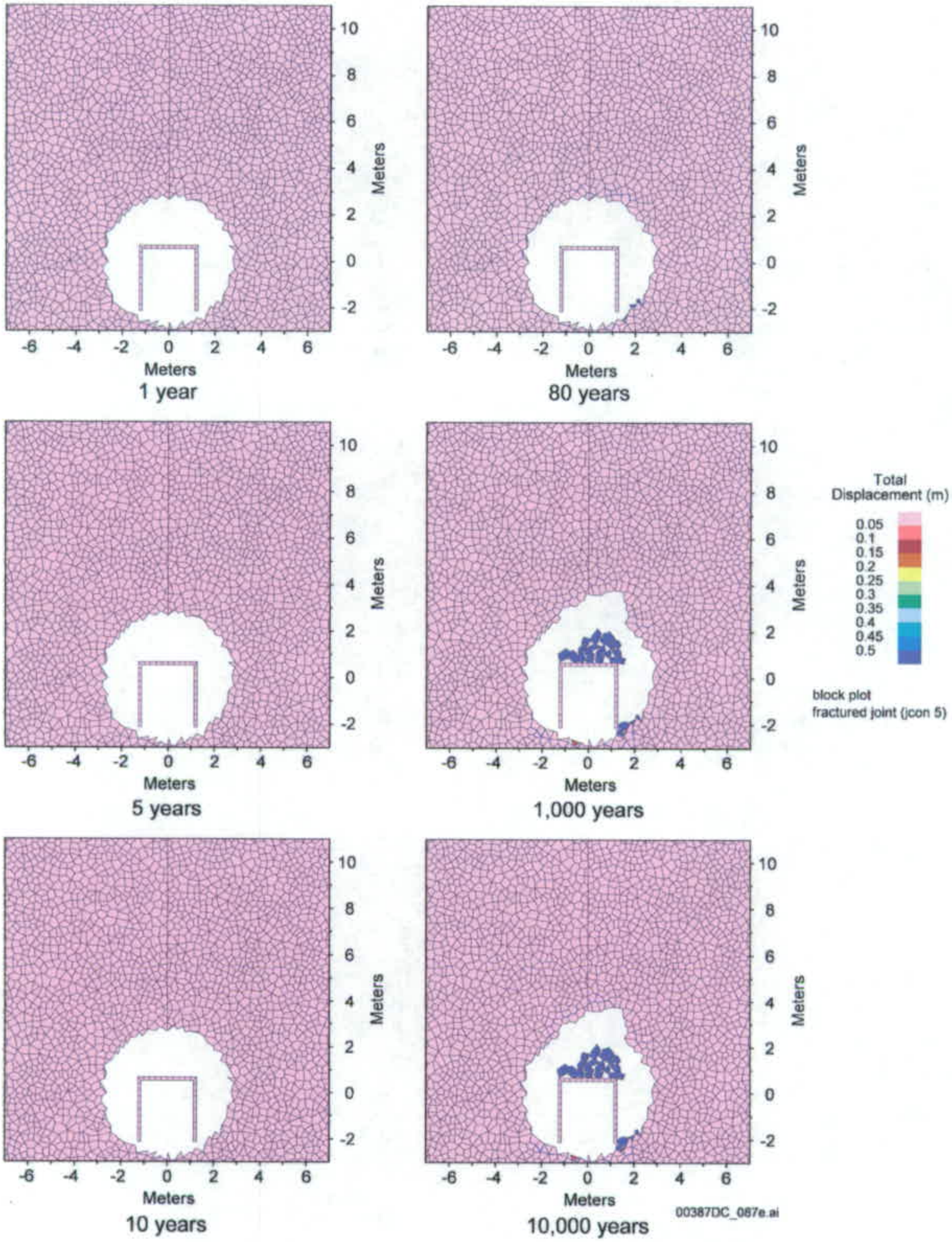
1 year

80 years

5 years

1,000 years

10 years

10,000 years

Figure 26. Predicted Evolution of Damage Due to Strength Degradation for Category 5–Tuff Best-Fit Static-Fatigue Curve, Combined *In Situ* and Thermal Stresses

The effect of a seismic event characterized by the 1×10^{-4} probability of annual exceedance, combined with *in situ* and thermal stressing, was investigated for time-dependent degradation modes for categories 2 and 5 rock masses. The 1×10^{-4} probability of annual exceedance seismic loading was chosen for this analysis as it may be considered that multiple events of this annual exceedance frequency could occur during the postclosure period. This work supplements previous seismic analyses in which thermal load was considered, but time-dependent strength loss was not.

The time frame when the combined *in situ* and thermally induced stress states reach their peak is at approximately 30 years after cessation of forced ventilation, or about 80 years after waste emplacement. However, when the time-dependent strength degradation is considered, the state when the maximum stresses are generated around the drift is not necessarily the critical state. The largest stresses occur relatively early during the regulatory period, and subsequently, the stresses decay gradually, returning to the state that existed prior to heating. At the same time the strength of the rock mass monotonically decreases as a function of time. In order to investigate the extreme effects of the combination of *in situ* and thermal stress and seismic ground motion on drift stability, dynamic analyses were carried out for the model states at 80 years and 10,000 years after waste emplacement.

The model geometry before and after the dynamic simulation is shown in Figures 27 and 28 for seismic ground motion 80 years after emplacement, and in Figures 29 and 30 for seismic ground motion 10,000 years after emplacement. In all the cases, additional rockfall is predicted due to the ground motion, which essentially shakes down the already-damaged rock mass resulting from the *in situ* and thermal stressing. This increase in the rockfall due to the 1×10^{-4} probability of annual exceedance seismic loading is greater than that predicted for *in situ* and thermal stressing alone, particularly for the category 2 case. There is also greater rockfall in the case of an earthquake 10,000 years, as opposed to 80 years, after waste emplacement.

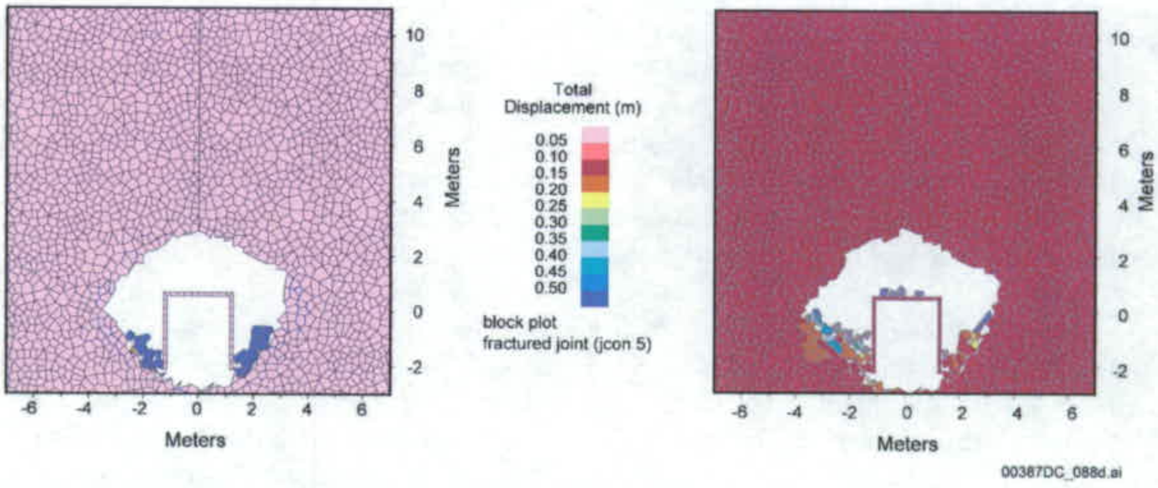

NOTE: Displacement magnitudes are in meters.

Figure 27. Effect of 1×10^{-4} Annual Probability of Exceedance Ground Motion after 80 Years of Heating in Category 2 before Seismic Shaking (Left) and after Seismic Shaking (Right): Blocks Colored by Contours of Displacement Magnitude

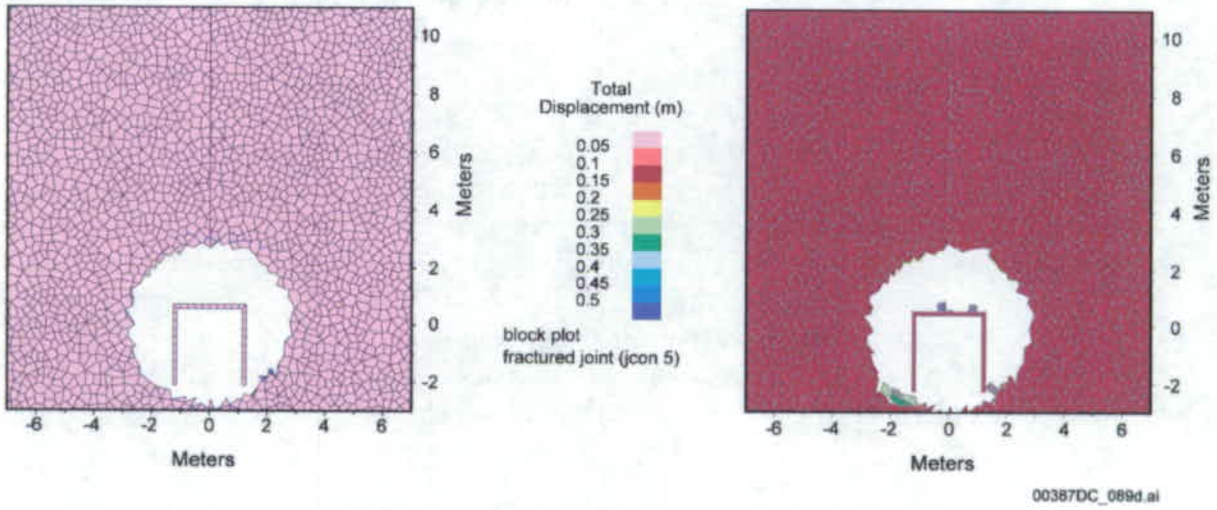

Figure 28. Effect of 1×10^{-4} Annual Probability of Exceedance Ground Motion after 80 Years of Heating in Category 5 before Seismic Shaking (Left) and after Seismic Shaking (Right): Blocks Colored by Contours of Displacement Magnitude

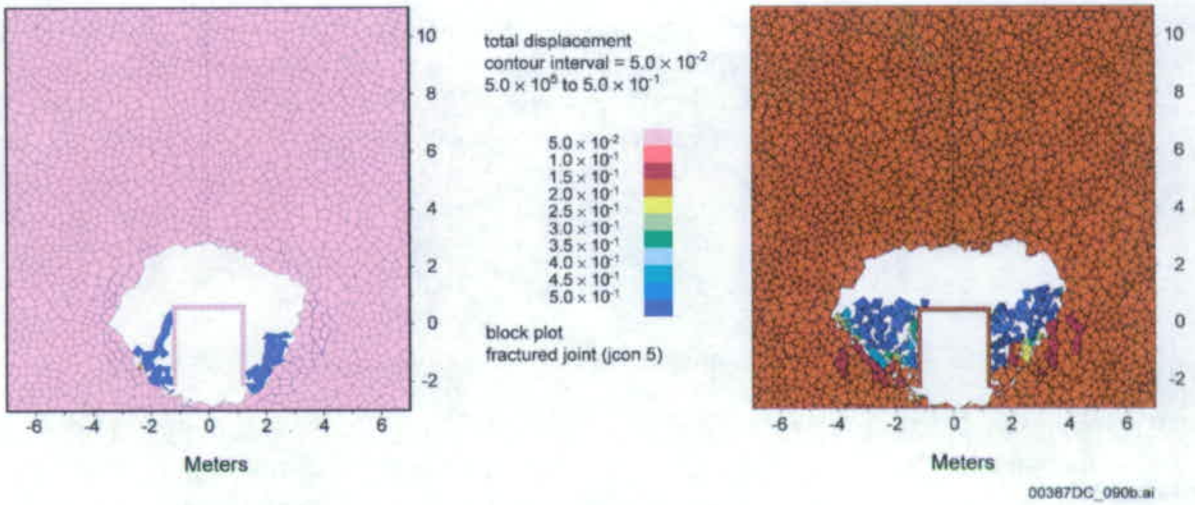

Figure 29. Effect of 1×10^{-4} Annual Probability of Exceedance Ground Motion after 10,000 Years of Heating in Category 2 before Seismic Shaking (Left) and after Seismic Shaking (Right) Contours of Displacement Magnitude

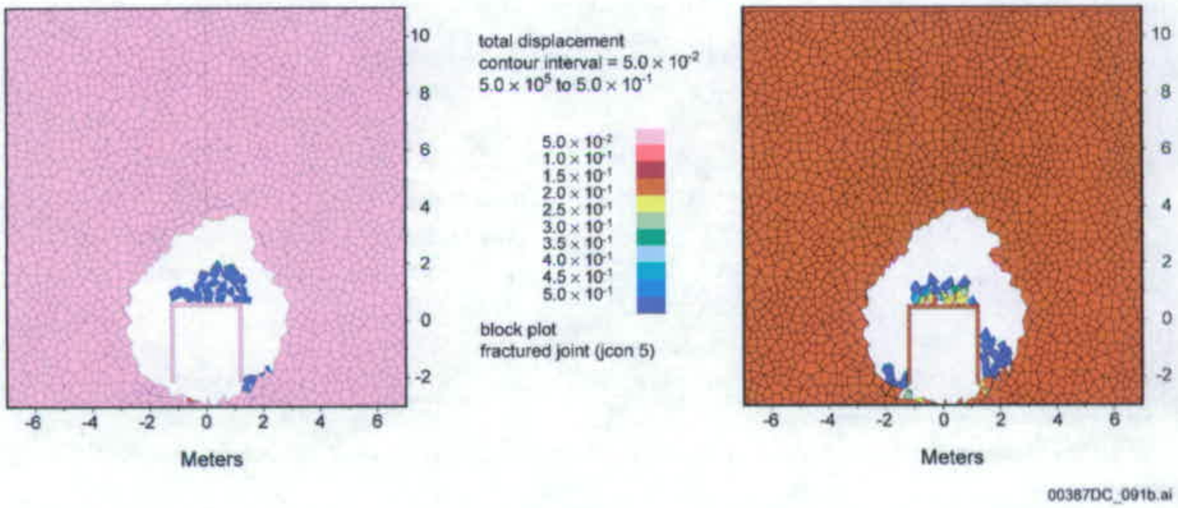

Figure 30. Effect of 1×10^{-4} Annual Probability of Exceedance Ground Motion after 10,000 Years of Heating in Category 5, before Seismic Shaking (Left) and after Seismic Shaking (Right). Blocks Colored by Contours of Displacement Magnitude

6. Conclusions

A lithophysal rockfall model was developed using the two-dimensional discontinuum code, UDEC, with the following features:

- Appropriate thermal and mechanical properties of the lithophysal rock have been determined through a combination of large diameter laboratory testing, field-scale testing, and calibrated numerical models. The model is used to examine the variability of mechanical properties with lithophysal porosity, shape, size, and distribution. The rock mechanical property range from testing has been subdivided into five quality "categories" that are functions of rock mass porosity. Categories 1 and 2 represent the lower end of the observed rock quality within the lithophysal rock, whereas Categories 3 and 4 represent an approximate average condition. Category 5 represents the higher quality, lower porosity portions of the lithophysal rock. These categories provide a basis for parametric calculations. A material model that accounts for the lithophysal rock mass behavior is developed. The majority of analyses were conducted for these bounding ranges of properties; however, a lithophysal porosity spatial variability model was developed to examine directly the impact of *in situ* variability on seismic and time-dependent drift stability.

- Appropriate boundary conditions are provided for thermal and seismic loading.
- The rock mass is represented as an assembly of polygonal, elastic blocks in which the bond strength of the blocks is calibrated such that the overall mechanical behavior of the mass is consistent with the material model developed for the lithophysal rock.
- The discontinuum lithophysal rockfall model allows for the formation of stress-induced fractures between blocks (i.e., the formation of internal fracturing) separation and instability (under the action of gravity or seismic shaking) of the rock mass around the drift.
- The effect of long-term degradation of rock mass strength is considered, assuming a stress corrosion mechanism that is dependent on time and applied stress level. An estimate of the degradation of emplacement drifts was developed by incorporating a time-related rock mass shear and tensile strength reduction factor into the drift degradation numerical model.
- Site-specific ground motion time histories are included in the model.

The results for the lithophysal rock are summarized as follows:

- Degradation is primarily controlled by stress conditions.
- Rock block size produced by degradation is controlled by the intense fracturing due to natural cooling of the lithophysal rock matrix as well as the spacing of lithophysae, and is unrelated to the more widely spaced, longer cooling fractures. The spacing of fractures in the lithophysal rock averages approximately 0.05 m, with a resulting small block side length when the rock is overstressed.
- 1×10^{-4} annual probability of exceedance ground motion results in minor drift damage due to rock failure.
- The 1×10^{-5} annual probability of exceedance ground motions result in a range of responses from no damage to collapse based on the highly variable amplitude of the individual time histories. A reasonable relationship between damage level and peak ground velocity or kinetic energy in the motion has been established.

General collapse of the drifts occurs for peak ground velocity greater than about 2 m/s. The 1×10^{-6} annual probability of exceedance ground motions result in predicted collapse of the drift, with fragmented rock particle sizes on the order of centimeters to decimeters.

- Thermal and time-dependent effects alone are expected to result in relatively small amounts of rockfall. Only in the poorest quality of rock are significant time-dependent breakouts expected. Time-dependent degradation is not expected to result in total collapse of the emplacement drifts.

Acknowledgements

This work was performed and funded under Department of Energy contract DE-AC28-01RW12101 for the Civilian Radioactive Waste Management System (CRWMS). Bechtel SAIC Company, LLC is the prime contractor for CRWMS.

Appendix A

The calibration of PFC stress corrosion model using the static fatigue data of granite and tuff are provided in this Appendix. Also included is the investigation of the impact of lithophysal porosity on the rate of time-dependence mechanical properties.

A.1. Static-Fatigue Behavior of Granite and Tuff

Martin et al. (1997) present static-fatigue results for a total of 16 specimens of welded (lithophysae poor) tuff from borehole NRG-7/7A at Yucca Mountain and from outcrop boulders. The specimens were 2:1 aspect-ratio right-circular cylinders with a diameter of 50.8 mm. Load application was rapid, with full load being reached in less than 10 seconds.

The seven borehole specimens were tested, drained, and vented to the atmosphere at a temperature of 225°C and a confining pressure of 10 MPa at differential stresses ranging from 40 MPa to 130 MPa. None of these specimens had failed after loading for times ranging from 2.5×10^6 seconds to 5.9×10^6 seconds. These results are not used since the applied stress at failure could not be determined. The nine outcrop specimens were tested at a porewater pressure of 4.5 MPa, a temperature of 150°C, and a confining pressure of 5 MPa at differential stresses ranging from 115 MPa to 150 MPa. The high pore pressure (i.e., 4.5 MPa) ensured that porewater remained in the liquid state even though the temperature is above the boiling point. Table A-1 summarizes the test results. The applied stress in the axial direction and the effective confining pressure are denoted by σ_1 and P_c, respectively. The axial load at failure during a short-term test is denoted by σ_f. The stress difference maintained during a static-fatigue test conducted at a confining pressure of P_c is $\sigma = \sigma_1 - P_c$. The stress difference at failure during a short-term test is $\sigma_c = \sigma_f - P_c$.

To facilitate comparison between different data sets, static-fatigue curves were generated by plotting the logarithm of time-to-failure, t_f, versus the driving-stress ratio given by $\sigma / \sigma_c = (\sigma_1 - P_c) / (\sigma_f - P_c)$. Six of these specimens failed at times less than 2×10^6 seconds, while the remaining three specimens (BB-9392-H, -G, and -J) did not fail during the testing period. The times-to-failure for these six tests can be plotted versus applied load (Figure A-1); however, the peak strength must be estimated in order to plot them versus driving-stress ratio for comparison with data from the Lac du Bonnet granite (Schmidtke and Lajtai 1985; Lau et al. 2000). For these purposes, the peak strength of the tuff samples at an effective confinement of 0.5 MPa is estimated to be 151 MPa, to give a failure time of one second for a driving-stress ratio of unity.[2]

Approximate linear relationships in semi-log space have been fit to the unconfined and confined granite and tuff data. The granite data shows a flatter slope, or faster time to failure than the tuff for similar ratios of the applied stress to unconfined compressive strength in this plot. This would be expected as the tuff is a fine-grained volcanic rock that shows very little hysteresis on unloading until brittle failure occurs. The granite, on the other hand, is composed of coarser mineral grain structure of several different minerals and exhibits permanent deformation at lower strain levels.

---

[2] The unconfined compressive strength values by Martin et al. (1997) for six saturated, 50.8-mm-diameter outcrop specimens tested at a strain rate of 10^{-5}/s ranged from approximately 105 MPa to 200 MPa, with a mean of approximately 128 MPa for the five weakest specimens.

Table A-1. Static-Fatigue Data for Outcrop Specimens

Specimen	Confining Pressure, P_c (MPa)	Stress Difference Maintained During Test, σ (MPa)	Time-to-Failure, t_f (sec)	Logarithm of Time-to-Failure, $\log(t_f)$ (sec)	Peak Strength, σ_f (MPa)	Driving-Stress Ratio, σ/σ_c
BB-9392-K	5	149.0	1.2	0.08	151	0.99
BB-9392-N	5	141.0	4	0.60	151	0.94
BB-9392-E	5	134.6	250	2.40	151	0.89
BB-9392-C	5	134.2	636	2.80	151	0.89
BB-9392-F	5	132.8	5848	3.77	151	0.88
BB-9392-B	5	127.8	1960000	6.29	151	0.85
BB-9392-H	5	131.4	1180000	6.07	151	0.87
BB-9392-G	5	131.3	732000	5.86	151	0.87
BB-9392-J	5	115.0	2000000	6.30	151	0.76

NOTE: Specimens were saturated and tested at a pore water pressure of 4.5 Pa and temperature of 150°C. Specimens were loaded directly to creep stress (σ_1) in less than 10 seconds. Specimen diameter is 50.8 mm. Specimens BB-9392-H, BB-9392-G, and BB-9392-J did not fail during the test. Confining pressure is the effective value from the applied confining stress (5 MPa) and pore pressure (4.5 MPa). See Martin et al. 1997 [DIRS 165960].

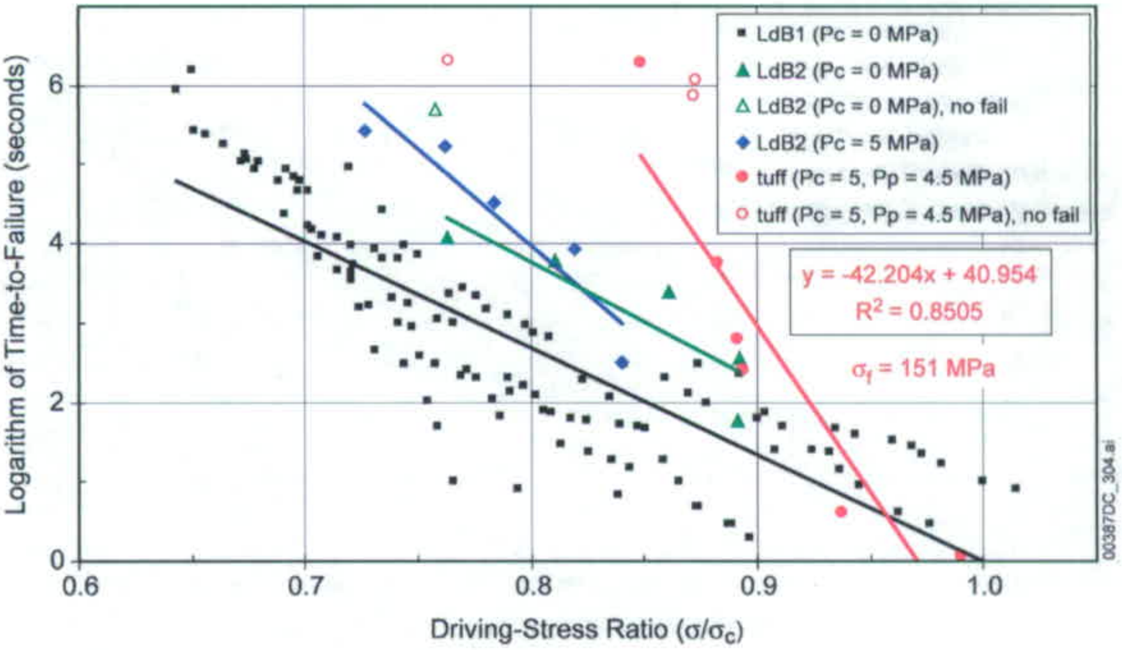

NOTES: Tests of Lac du Bonnet granite conducted at 25°C. Tuff tests conducted at 150°C.

Figure A-1. Static-Fatigue Data for Welded Tuff and Lac du Bonnet Granite

A.2. PFC Corrosion Model Calibration and Examination of Impact of Lithophysal Voids

The static fatigue data for welded tuff shown in Figure A-1 is for nonlithophysal samples. For the consideration of lithophysal rock, it is necessary to determine the impact of lithophysal voids on the static fatigue response (essentially, the slope of the best-fit lines in this figure).

Since the matrix material of the nonlithophysal and lithophysal tuff is mineralogically and mechanically similar, an approach to estimate the impact of lithophysae on the time-dependency can be developed based on the existing static fatigue data. The PFC program is first calibrated to reproduce the static fatigue response of the nonlithophysal rock. Using the same matrix properties, lithophysal porosity is added and time-dependency extrapolated. This is a reasonable approach because the primary effect of lithophysae is to adjust the internal stress condition of the sample, which, in turn, impacts the time-to-failure. PFC automatically determines the internal stress redistribution and concentration in the sample and, thus, accounts for this primary effect.

The PFC model for lithophysal tuff was described previously in Section 4.2.1. This PFC model (consisting of circular voids within a well-connected base material) has the same matrix material for which the stress-corrosion behavior is measured. The long-term behavior of the PFC material is characterized by performing a series of static-fatigue tests on the PFC lithophysal-tuff model. Recall that the PFC model consists of rigid, circular particles interconnected at their contact points. The macroscopic material behavior of the PFC model is governed by the strength and stiffness properties of the contact points. The PFC stress corrosion model uses the same construction and bonding characteristics as the model presented earlier, with the difference being that the bond strengths include time-related parameters consistent with a stress corrosion cracking mechanism. These time-dependent bond parameters (β_1, β_2, and $\bar{\sigma}_a$) are determined via calibration of the PFC model to static fatigue time-to-failure test data. These parameters do not affect the short-term behavior. The properties of the PFC material are obtained by numerically testing 1:1 aspect-ratio specimens (Figure A-2) of one-meter diameter with void porosities of 0, 0.1, and 0.2 under static-fatigue conditions at confinements of 0.1 MPa and 5 MPa.

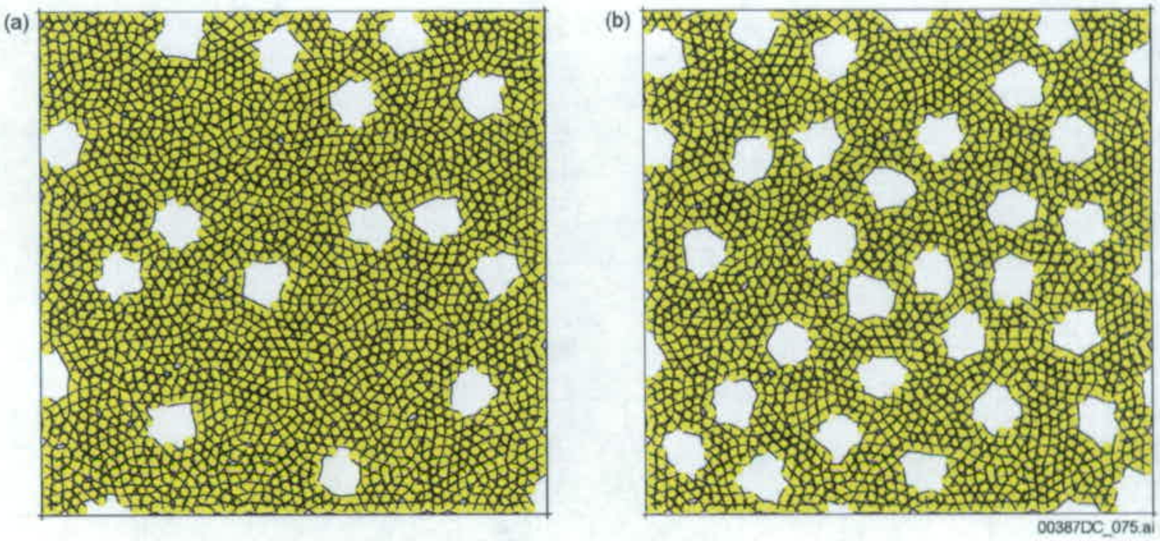

NOTE: Examples have void porosities of 0.107 (a) and 0.204 (b).

Figure A-2. PFC Specimens of Tuff Material for Static Fatigue Testing

Figure A-3 shows a typical "creep" curve and damage plot from a PFC nonlithophysal rock test in which the sample uniaxial load is held constant at 80% of the unconfined compressive strength. Damage occurs in the form of formation of cracks as a function of time. As seen, the sample undergoes time-dependent deformation until approximately 5,000 seconds (t_f), when creep rupture occurs and the sample fails. Numerical tests such as these are used first to calibrate the PFC model against the laboratory data for nonlithophysal tuff, but then to extrapolate the time-to-failure data to lithophysal rock with varying levels of lithophysal porosity.

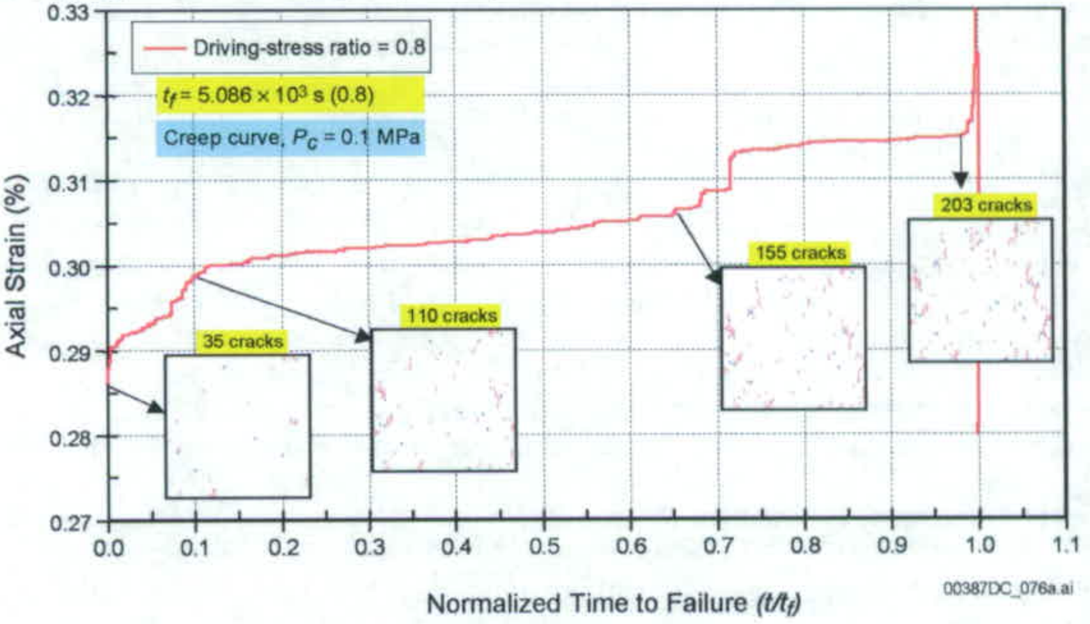

Figure A-3. Creep Curve and Damage in PFC Material for Static-Fatigue Test (0.1 MPa Confinement) at Driving-Stress Ratio of 0.8

Figure A-4 shows a plot of the time to failure for different levels of sample porosity as a function of the ratio of applied stress to unconfined compression strength for lithophysal tuff samples. As one might expect, as the lithophysal porosity increases, the time –to failure of the rock mass decreases, presumably due to the presence of increased level of tensile stresses in the material.

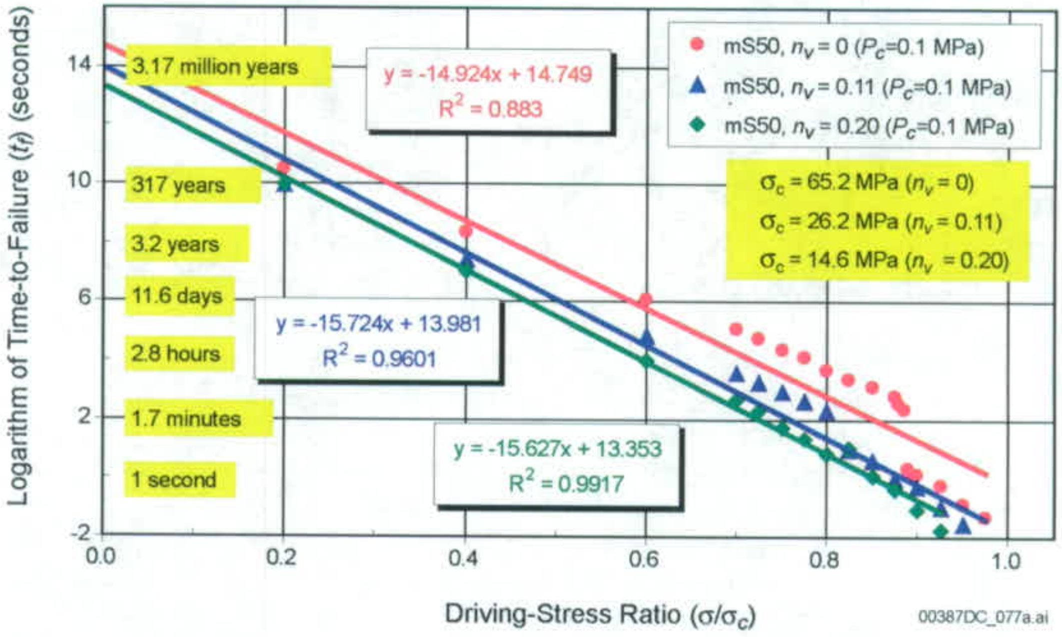

NOTES: The time-dependency has approximately the same slope for all void porosities. Straight-line fit.

Figure A-4. Effect of Void Porosity on Static-Fatigue Curves (0.1 MPa Confinement) for Lithophysal Tuff Material (0% to 20% Void Porosity)

A.3. Inclusion of Time-Dependency Into an Engineering Approximation of Drift Degradation

To utilize the time-to-failure data for lithophysal tuff, it must be generalized into an engineering-based model that can predict the evolving stress state around excavations resulting from time-dependent strength degradation as well as from *in situ*, thermal, and seismic loading. The same UDEC approach that has been used for the previous calculations is used for this purpose. Because the UDEC model is used in a quasi-static mode in this regard, it is most convenient to frame the time-to-failure data in the form of a simple damage coefficient that represents the time-evolution of strength degradation.

A.4. Damage Coefficient Derivation

The axial load at failure (peak strength) during a short-term test performed at an elapsed time, t, since the start of a static-fatigue test is denoted by $\sigma^*_f = \sigma^*_f(t)$. The values of σ^*_f are bounded by:

$$\sigma^*_f(0) \le \sigma_f$$

$$\sigma^*_f(t_f) \geq (\sigma/\sigma_c)\,(\sigma_f - P_c) + P_c \qquad \text{(Eq. A-1)}$$

where (σ/σ_c) is the ratio of the driving stress to the unconfined compressive strength of the material, and P_c is the confining pressure of the test. The values of σ^*_f for times $0 < t < t_f$ are found by stopping the static-fatigue test at the desired time and measuring the peak strength.

The strength degradation is quantified by means of a damage coefficient:

$$D = 1 - \sigma^*_c / \sigma_c \qquad \text{(Eq. A-2)}$$

where $\sigma^*_c = \sigma^*_f - P_c$ is the principal stress difference at failure. Substituting values from Equation 5-1 into this expression provides the following bounds for the damage coefficient:

$$\begin{aligned} D(0) &= 0 \\ D(t_f) &= 1 - (\sigma/\sigma_c) \end{aligned} \qquad \text{(Eq. A-3)}$$

The time evolution of the damage coefficient for the nonlithophysal tuff material tested at a confinement of 0.1 MPa is shown in Figure A-5. These results were produced by performing 10 numerical compression tests conducted on damaged "samples" derived from four static-fatigue tests at driving stress ratios of 0.8, 0.6, 0.4, and 0.2. In other words, the PFC stress corrosion model spontaneously produces stress corrosion fracturing as the simulated static fatigue test is run. To determine the impact of this damage on the strength of the sample, the static fatigue simulations are stopped at various elapsed times and the damaged "sample" compressed to determine its peak strength. The loss of cohesive and tensile strength, expressed as a ratio of the original strength, is termed the damage coefficient. Most damage occurs during the final stages of a static-fatigue test; tests performed at lower driving-stress ratios produce an earlier (in terms of normalized times to failure) onset of damage. Damage evolution for lithophysal tuff follows a similar form, with the time factor determined from the time-to-failure behavior illustrated in Figure A-4.

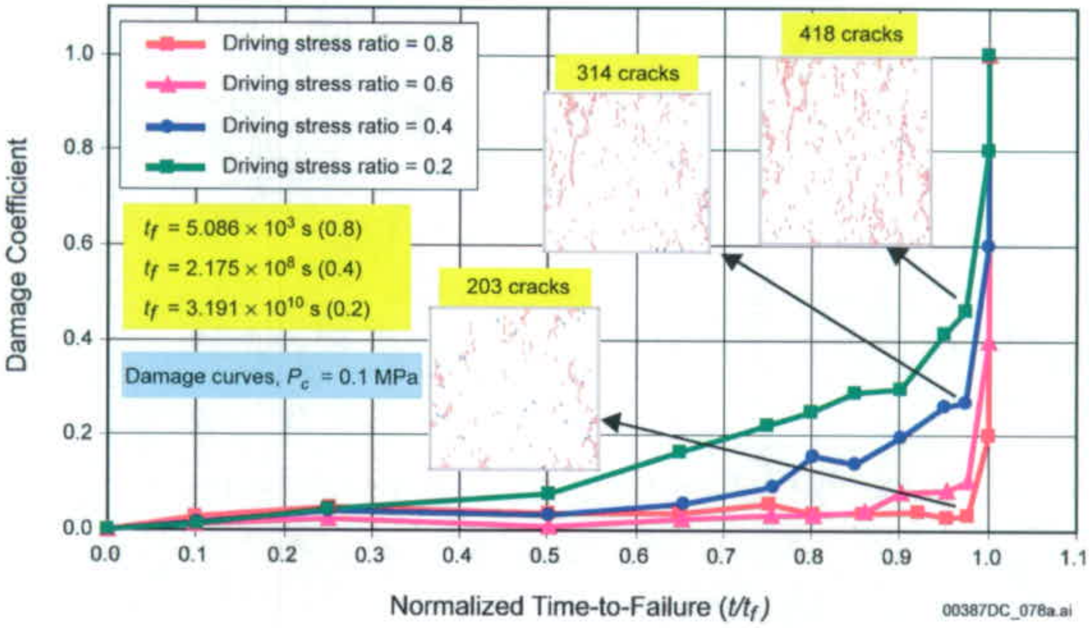

Figure A-5. Time Evolution of Damage Due to Strength Degradation Coefficient for Nonlithophysal Tuff Material during Static-Fatigue Tests (0.1 MPa Confinement) at Driving-Stress Ratios Ranging from 0.2 to 0.8

A.5. Static-Fatigue Curves and the Evolution of Damage Due to Strength Degradation

The static-fatigue behavior of Lac du Bonnet granite and welded lithophysal tuff forms the basis of the UDEC model for stress corrosion around a drift. The static-fatigue curves provide the time-to-failure (t_f) of the material at a particular driving-stress ratio (σ/σ_c).

The static-fatigue data for Lac du Bonnet granite at 0 MPa and 5 MPa confinement and tuff at 5 MPa confinement and 4.5 MPa pore pressure are shown in Figure A-1. Each data set was fit with a straight line, and the line was extrapolated to encompass driving-stress ratios ranging from 0 to 1. This is a conservative assumption, because the curves most likely approach infinity at a driving-stress ratio less than about 0.5. Three lines for the tuff data are shown in Figure A-6. The blue line in the figure is the least-square linear fit through the tuff data, while the magenta line (best-fit-through-origin curve) is the best fit for the tuff data for unconfined compressive strength (i.e., failure at 1 s at the unit driving ratio of 1.0). Since the tuff data are very limited and are for confined conditions (effective confining stress of 0.5 MPa) only, the data input to UDEC uses a simplified best-fit curve (red line) termed the "tuff best-fit curve." The tuff best-fit curve will be updated as the ongoing test data become available.

Using the time-to-failure versus stress-to-strength ratio (Figure A-6) and the damage coefficient evolution plot, a simplified, general damage evolution curve in terms of time can be developed and used directly in the UDEC program for drift stability modeling. Figure 24 presents these relations for the tuff best-fit curve. This family of curves can be used to directly relate reduction in cohesive and tensile strength of the rock mass as a function of stress state and elapsed time since excavation.

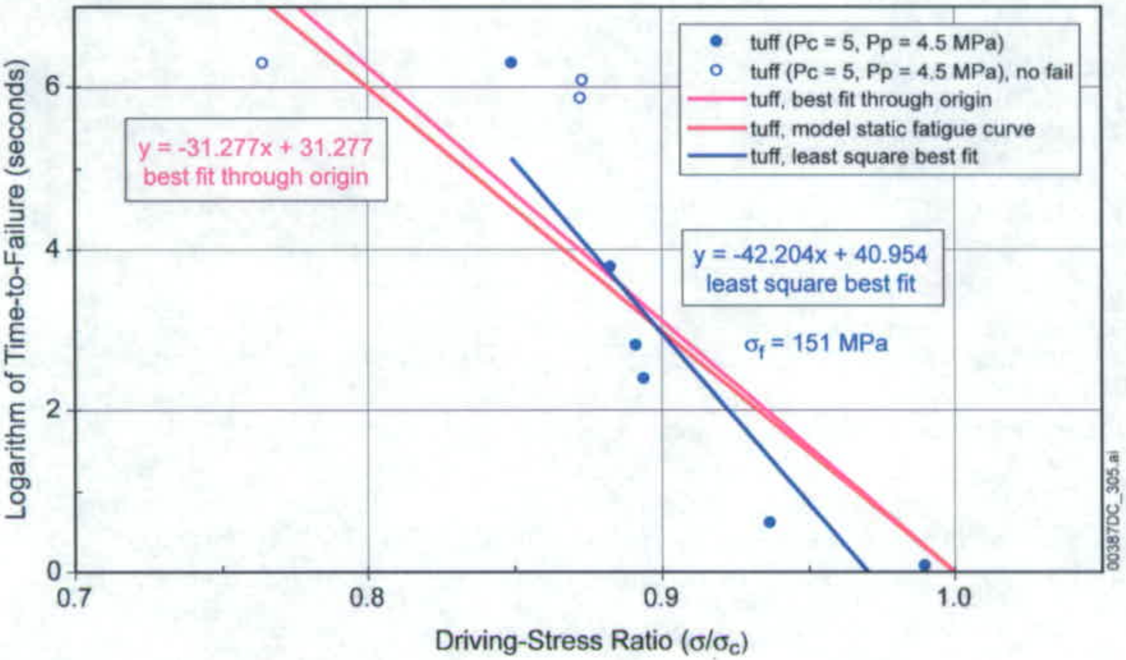

NOTE: Tuff tests were conducted at 150°C.

Figure A-6. Static-Fatigue Curves Used as Input to the UDEC Analyses

References

Bechtel SAIC Company 2004. *Drift Degradation Analysis.* ANL-EBS-MD-000027, Rev. 03. Las Vegas, Nevada: Bechtel SAIC Company.

Itasca Consulting Group 2002. *Itasca Software–Cutting Edge Tools for Computational Mechanics*. Minneapolis, Minnesota: Itasca Consulting Group.

Kranz, R.L. 1979. "Crack Growth and Development during Creep in Westerly Granite." *International Journal of Rock Mechanics and Mining Sciences, 16,* 23–36. New York, New York: Elsevier.

Kranz, R.L. 1980. "The Effects of Confining Pressure and Stress Difference on Static Fatigue of Granite." *Journal of Geophysical Research, 85,* 1854–1866. Washington, D.C.: American Geophysical Union.

Lau, J.S.O.; Gorski, B.; Conlon, B.; and Anderson, T. 2000. *Long-Term Loading Tests on Saturated Granite and Granodiorite.* Report No. 06819-REP-01300-10061-R00. Toronto, Ontario, Canada: Ontario Power Generation, Nuclear Waste Management Division.

Lin, M.; Board, M.P.; Kicker, D.C.; Leem, J.; Damjanac, B. and Buesch, D.C. 2005. "Assessment of Drift Stability with Consideration of Spatial Variation of Lithophysal Cavities at Yucca Mountain." *Rock Mechanics for Energy, Mineral and Infrastrucutre Development in the Northern Region, Proceedings of the 40th U.S. Symposium, Anchorage, Alaska, USA, 25-29* June, 2005. Chen, G.; Huang, S.; Zhou, W.; and Tinucci, J.; eds. ARMA/USRMS 05-802. University of Alaska, Fairbanks.

Martin, R. J. 1972. "Time-Dependent Crack Growth in Quartz and Its Application to the Creep of Rocks." *Journal of Geophysical Research, 77,* 1406–1419. Washington, D.C.: American Geophysical Union.

Martin, R.J.; Noel, J.S.; Boyd, P.J.; and Price, R.H. 1997. "Creep and Static Fatigue of Welded Tuff from Yucca Mountain, Nevada." *International Journal of Rock Mechanics and Mining Sciences, 34,* (3/4), 382. New York, New York: Elsevier.

Newmark N.M. 1965. "Effects of Earthquakes on Dams and Embankments." *Geotechnique*, *15*, (2), 139-160. London, England: Thomas Telford.

Potyondy, D. and Cundall, P. 2001. *The PFC Model for Rock: Predicting Rock-Mass Damage at the Underground Research Laboratory.* Report No. 06819-REP-01200-10061-R00. Toronto, Ontario, Canada: Ontario Power Generation, Nuclear Waste Management Division.

Price, R.H. 1983. *Analysis of the Rock Mechanics Properties of Volcanic Tuff Units from Yucca Mountain, Nevada Test Site.* SAND82-1315. Albuquerque, New Mexico: Sandia National Laboratories.

Price, R.H. and Bauer, S.J. 1985. "Analysis of the Elastic and Strength Properties of Yucca Mountain Tuff, Nevada." *Research & Engineering Applications in Rock Masses, Proceedings of the 26th U.S. Symposium on Rock Mechanics, Rapid City, South Dakota, June 26-28, 1985.* Ashworth, E., ed. Pages 89-96. Boston, Massachusetts: A.A. Balkema.

Schmidtke, R.H. and Lajtai, E.Z. 1985. "The Long-Term Strength of Lac du Bonnet Granite." *International Journal of Rock Mechanics and Mining Science & Geomechanics Abstracts, 22,* (6), 461-465. New York, New York: Pergamon.